Modeling of the Thermomechanical Response of Shape Memory Alloys

by
Mengqian Zhang

A dissertation submitted to the Department of Mechanical Engineering,

University of Houston

in partial fulfillment of the requirements for the degree of

Doctor of Philosophy
in Mechanical Engineering

Chair of Committee: Dr. Theocharis Baxevanis

Committee Member: Dr. Pradeep Sharma

Committee Member: Dr. Yi-Chao Chen

Committee Member: Dr. Kalyana Babu Nakshatrala

Committee Member: Dr. Shailendra Joshi

University of Houston
December 2021

ACKNOWLEDGMENTS

I would like to thank all the people who have contributed to the successful completion of the current dissertation and inspired me during my doctoral studies.

First of all, I would like to express my thanks and gratitude to my Ph.D. advisor Prof. Theocharis Baxevanis who spent four and half years supervising and helping me with my academic research. His dedication and interests on research have overwhelmed me to open my mind for research. His suggestions on scientific approaches have helped me to a great extent to accomplish this task. I also want to thank him for putting a lot of effort in training me to write scientific papers and how to give presentations properly. I would like to acknowledge my committee, Dr. Pradeep Sharma, Dr. Yi-Chao Chen, Dr. Shailendra Joshi, Dr. Kalyana Babu Nakshatrala and Dr. Theocharis Baxevanis for reviewing my dissertation and giving valuable suggestions and comments. I would further like to express my thanks to Drs. Pradeep Sharma, Yi-Chao Chen, and Shailendra Joshi for their courses that I attended. Special thanks would go to my fellow labmates through all these years in Active Materials Research Group, Ph.D. candidates Md Afzal Hossain, Jasdeep Makkar, Md Mehedi Hasan for their encouragement and collaborations. I also have been lucky to have friends here who share their knowledge and experience with me. The list includes, but not limited to, Yifei Wang, Mengshi Jin, Yitong Hao, Siwei Chen, Qiang Fu, Kosar Mozaffari, and Xin Yan.

I cannot find words to express my gratitude to my parents Ming Zhang and He Yi for the unconditional and invaluable support they have been providing me all these years. I want to dedicate my dissertation to them. A special thought also goes to my husband Hao Liu for his patience and faith during my graduate study. It is my luck to have him and my beloved pet (dundun) in my life and their companions help me get through the hardest time.

Finally, I would like to acknowledge the funding agencies for providing financial support for my research during my doctoral studies and all the accommodations during international conferences and workshops. I also greatly appreciate the financial support from NSF for the International Institute of Materials for Energy Conversion (IIMEC) Summer School that I participated in during July 2018 at Thessaloniki, Greece.

Mengqian Zhang

November 8, 2021

ABSTRACT

Shape memory alloys (SMAs) are metallic materials that have the ability to ”remember” their previous form when subjected to appropriate thermomechanical stimuli. This ”smart” property, which is attributed to a reversible, diffusionless, solid-to-solid phase transformation from austenite to martensite, renders SMAs desirable for applications in the medical, aerospace, and automotive industries. Recent research also demonstrated that SMAs exhibit tailorable bulk thermal expansion (TE), projected to achieve coefficient of TE (CTE) over a wide range of positive and negative values, via martensite variant texturing by taking advantage of the significant intrinsic TE anisotropy of the martensite lattice. There is, therefore, a remarkable potential of SMAs in applications in which TE is a critical design factor, such as high precision instruments in optical applications and satellite antennas. To ultimately realize the true potential of SMAs in engineering applications as ”smart” or low-CTE materials, constitutive models capable of effectively describing their response to thermomechanical stimuli are needed to enable efficient design of SMA-based devices. In this thesis, a constitutive model is proposed that i) can efficiently describe reversible phase transformation from austenite to self-accommodated and/or oriented martensite, (re)orientation of martensite variants, minor loops, latent heat effect and tension-compression asymmetry, and ii) tailor the bulk TE tensor based on an effective description of martensite variants texture. The strengths of the proposed model lie in i) its ability to account for all the aforementioned aspects aspects of the deformation response of SMAs and highlight their collective importance in complex non-proportional thermomechanical loading, and ii) its innovation to accurately tailor the TE evolution during deformation processing. The model is validated against experimental results under tension/compression/torsion box loading and on the CTE evolution due to orientation of self-accommodated martensite, and verified by numerical simulations of 3D SMA-based structures.

TABLE OF CONTENTS

LIST OF TABLES

LIST OF FIGURES

1 INTRODUCTION

1.1 Shape Memory Alloys and their Applications

Advances in technology drive the development of ”smart systems” with adaptive and intelligent features, which is, however, highly restricted by material limitations. A new category of materials, called ”smart materials”, has emerged, which includes Piezoelectrics, Electrostrictives, Piezomagnetics and Magnetostrictives and Shape Memory Alloys (SMAs). SMAs are metallic materials which can sustain large deformation and recover to their initial size under appropriate thermomechanical stimuli. SMAs have drawn significant attention and interest in recent years in a broad range of engineering applications in the aerospace, automotive, and biomedical industries.

Recent experiments [73] also demonstrated that SMA exhibit tailorable bulk thermal expansion (TE), projected to achieve coefficient of TE (CTE) values between a wide of range of positive and negative values, via martensite variant texturing by taking advantage of the significant intrinsic TE anisotropy of the martensite lattice; one or more lattice directions of martensite lattice exhibit negative thermal expansion upon heating. Thus new innovative applications of SMAs are booming in domains where TE is a critical design factor and dimensional stability and/or thermal fatigue resistance over a wide range of temperatures are required, such as high precision instruments in optical applications and satellite antennas.

1.1.1 Applications in the automotive and aerospace industries

The mechanical simplicity and compactness of SMA actuators reduce the scale, weight and cost of automotive components significantly and provide substantial performance benefits. In aerospace researchers, SMAs are applied in active and

adaptive structures toward morphing capability and system-level optimisation under various flight conditions. We take the application of morphing chevron of 'smart wings' as an example. Boeing has developed an active serrated aerodynamic device with wire SMAs actuators, which is also known as a variable geometry chevron (VGC) (see in Figure 1.1). This device has proven to be very effective in reducing noise during take-off by maximizing the chevron deflection, and also increasing the cruise efficiency by minimizing the chevron deflection during the remainder of the flight.

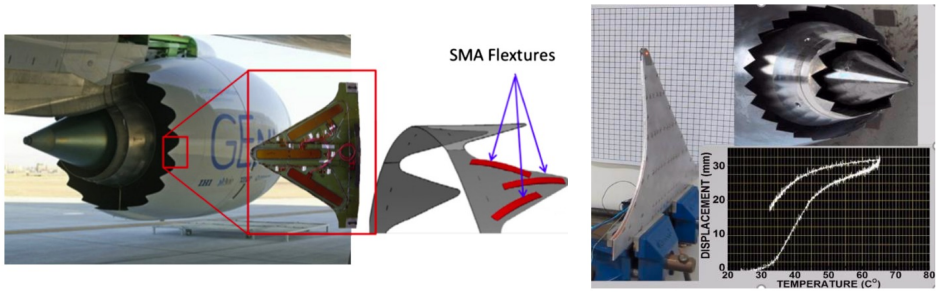

Figure 1.1: SMA wire actuators of Chevron (VGC) [67, 79]

The author in [47] concludes current research or development trends of SMAs in automotive and aerospace industries, they are:

- Self-healing and sensing structures/components
- Morphing capability for aerodynamic and aesthetic features
- High temperature actuators
- Noise, vibration and harshness
- Dampers/isolators
- Rotary actuators

Figure 1.2: Application of SMAs actuators in robots [47]

1.1.2 Applications in robotics

SMAs have been used in a diverse range of commercial robotic systems, especially as micro-actuators or artificial muscles. Several flying robots have been developed with SMAs, such as the BATMAV [30, 13] and Bat Robot [23] . The SMA actuators are equipped to control the stability of movements flight (see Figure 1.2). Additionally, a new SMA actuator design for a prosthetic hand was introduced [66], where two SMA actuators are used to actuate the robotic finger instead of using the conventional push–pull type and the biased spring type (Figure. 1.2).

1.1.3 Applications in biomedicine

SMAs have lots of excellent properties for the biomedical instruments, for example, their functional properties like shape memory effects, high corrosion resistance. Moreover, the bio-compatibility with human tissues and bones, gives SMAs with substantial advantages and great opportunities for further commercial success in the biomedical fields, even though, it is significantly more expensive compared with other candidate materials like stainless steel.

The widest application of SMAs in the biomedical field is the self-expanding stent, which is being used extensively to treat occlusions in endovascular arterial lumens, such as narrowing of the blood vessels. The stent was firstly crimped and mounted on a tube catheter outside the body, as shown in Figure 1.3. And

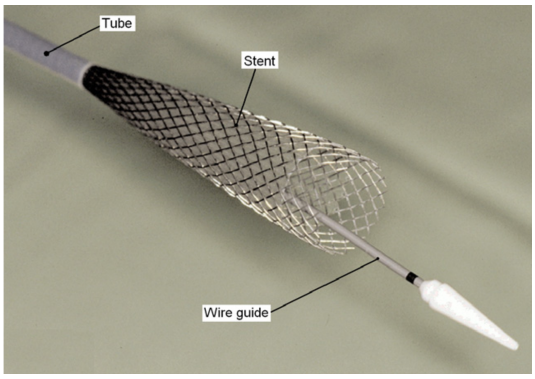

Figure 1.3: Self-expanding stent [8]

then the stent is inserted into the blood vessel to the position with arterial diseases by the delivery system. When releasing the delivery tube, the NiTi SMAs stent self-expands and exerts a radial force on the blood vessel to keep it open.

1.2 Phase Diagram of SMAs

SMAs are metallic materials which can sustain large deformation and recover to their initial shape under reasonable thermomechanical load. The capability of the material is because of the exhibit of a reversible, diffusionless, solid-to-solid phase transformation from austenite to martensite. Large inelastic strain induced during forward phase transformation from austenite to martensite can be recovered during reverse phase transformation. This dissertation focuses on modeling the material response under thermomechanical loading.

Austenite, the parent phase of SMAs, is usually characterized by a cubic crystallographic structure, and is stable at high temperature and low stress. *Martensite*, which is characterized by lower-symmetry crystallographic structure (for example, monoclinic of NiTi SMAs), generally exits in two states, *self-accommodated* (twinned) martensite and *oriented* (de-twinned) martensite. As shown in Figure 1.4, in the absence of applied stresses, the temperature-induced variants of

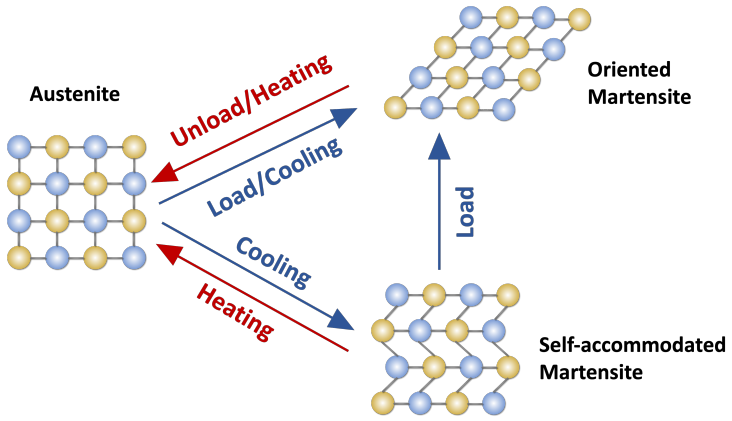

Figure 1.4: Schematic of phase transformation of SMAs

the martensite phase usually arrange themselves in a self-accommodating manner, compensating each other. According to the terminology introduced in [95], the self-accommodated martensite transforms to and from austenite without any macroscopic deformation. The formation of oriented martensite is ascribed to mechanical loading. Mechanical loading forces the martensite variants to orient towards the direction of the applied loading yielding a macroscopic shape change and the oriented martensite is formed. The oriented martensite is stable at low temperature and high stress.

To describe the phase transition of SMAs, phase diagrams of SMAs are developed in terms of stress and temperature, as shown in Figure 1.5. The phase diagram consists of equilibrium lines or phase boundaries that refer to lines that declare conditions under which multiple phases can coexist at equilibrium. Phase transformations occur along the lines of equilibrium.

In the phase diagram Figure 1.5, the three phases, austenite, self-accommodated, and oriented marteniste, are denoted as A, M^{sa}, and M^{o}, respectively. M_f, M_s, A_s, and A_f are the martensite-finish, martensite-start, austenite-start, austenite-finish transformation transition temperatures at zero load level, and σ_s and σ_f stand

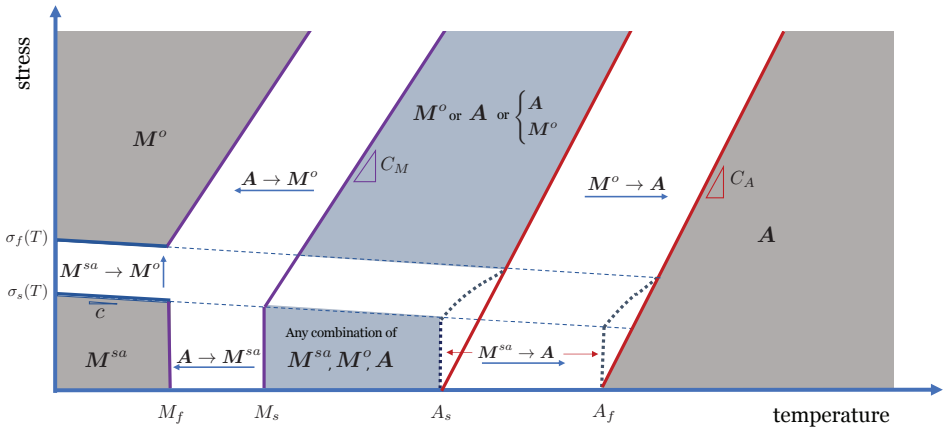

Figure 1.5: Stress–temperature phase diagram

for the critical values of stress required for initiation and completion of orientation at a given temperature, respectively. The white strips indicate transition from one phase to another and are labeled accordingly. When multiple strips overlap, multiple transitions are possible. The different width of the forward and reverse phase transformation strips indicate asymmetry between forward and reverse phase transformation. The different slopes of those strips indicate load and temperature dependence of the hysteresis loop width. Note also the temperature dependence of the orientation strip. The relevance of this phase diagram to experimental results can be traced in [84] and [4].

In this dissertation, three types of constraints (boundary lines) are defined to model and describe the material response under thermomechanical loading.

- *Phase transformation*, phase transitions between austenite and martensite (self-accommodated and oriented), both temperature-induced and stress-induced are included. Phase transition from autenite to martensite is defined as forward phase transformation, and vise versa is referred to as reverse phase transformation.

- *Orientation*, it indicates the process that mechanical loading forces the self-accommodated martensite variants to orient towards the direction of the applied load, and the process is constrained by σ_s and σ_f.

- *Reorientation*, it refers to the direction changes of the oriented martensite attributed to the changes of loading path. According to this definition, the magnitude of inelastic strain keeps constant during the direction changing. This process actives when local non-proportional evolution is induced by the loading complexity or the geometric nonlinearity.

The famous material behavior of SMAs, such as *shape memory effects (SME) and psuedoelasticity*, and some secondary features, like *tension-compression asymmetry, minor-loop, thermomechanical coupled response, anisotropic of thermal expansion*, will be discussed in the following sections.

1.3 Primary Features of the Deformation Response of SMAs

1.3.1 Shape Memory Effect

Shape memory effect (SME) is one of major material behaviors of SMAs, which is associated with temperature-induced phase transformation. It represents a process when the material is deformed while in the self-accommodated martensitic phase due to mechanical loading and then unloaded while at a temperature below A_s. The material maintains the deformation until it is subsequently heated above A_f, the SMA will regain its original shape by transforming back into the parent austenitic phase.

The detailed loading paths of SME are listed below.

1. Starting from the parent phase austenite (point A in Figure 1.6 (a)), and cooling the material to the temperature below M_s under stress-free condition, which leads to the formation of self-accommodated martensite (point B). No apparent

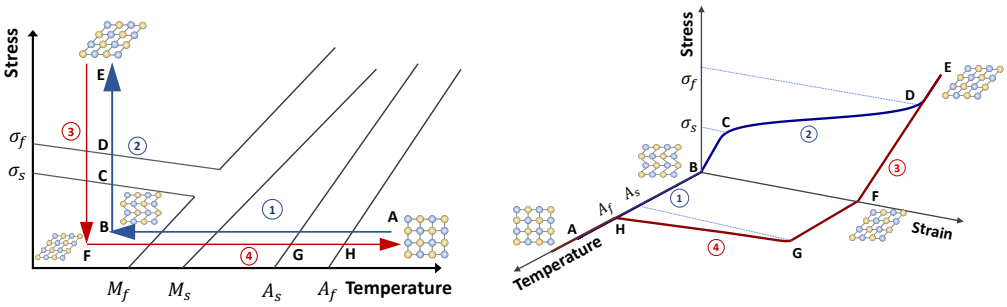

(a) Loading path of SME

(b) Stress-strain-temperature response for typical SME

Figure 1.6: Shape memory effect of SMAs

deformation is generated in this step.

2. Applying stress loading on the self-accommodated martensite (Point B) until the applied stress exceeds the start stress level (σ_s, Point C), the orientation process initiates, and results in the growth of certain favorably oriented martensitic variants. The orientation process is completed at a stress level, σ_f (Point D), that is characterized by the end of plateau in curve C $\rightarrow$ E.

3. The material is then elastically unloaded from E to F and the oriented martensite state is retained.

4. The deformation then recovered due to heating from Point F to H. Upon heating, the reverse transformation initiates when the temperature reaches A_s, (at Point G) and completes at temperature A_f (Point H), where the material fully transforms back to austenite.

The unique property, shape memory effect, provides SMAs a remarkable advantages to be desirable materials for actuators. A simple actuating loading path, which referred to a temperature-induced phase transformation under isobaric condition, is illustrated in Figure 1.7. The material initially subjected to a constant mechanical loading which results to developing a stress level higher than σ_f

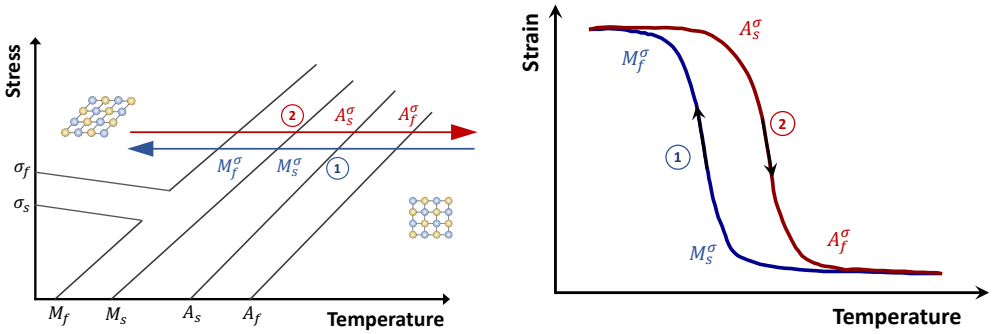

(a) Loading path

(b) A typical strain-temperature response under isobaric condition

Figure 1.7: Temperature-induced phase transformation under isobaric loading

(lower than σ_{M_s}, to make sure that the phase transformation is completely induced by temperature and psuedoelasticity doesn't affect).

The actuation starts at relative high temperature, above A_s^σ, and the material is at austenite. Cooling the material as the Path 1 shown in Figure 1.7(a), the forward phase transformation initiates when the temperature reaches M_s^σ and completes when it cools to M_f^σ. Large deformation yields during this process. The deformation recovers to the initial shape by heating the material as Path 1 shown in Figure 1.7(a). The reverse phase transformation initiates and completes at temperature A_s^σ and A_f^σ.

Although the materials have good capabilities, the real application of actuator is still restricted by the technical issues, such as keeping constant stress level on the material and speeding up the cooling process.

1.3.2 Psuedoelasticity

Another major material characteristic of SMAs is pseudoelasticity, also called as superelasticity. The pseudoelastic behavior is associated with stress-induced transformation, which leads to strain generation during loading and subsequent

strain recovery according to unloading at a constant temperatures above A_f. A pseudoelastic loading path usually starts at a sufficiently high temperature where austenite is stable, then applies load to a state at which oriented martensite is stable, and finally reverses to the austenitic phase by unloading. Generally, the loading cycle is performed under constant temperature which is above A_f .

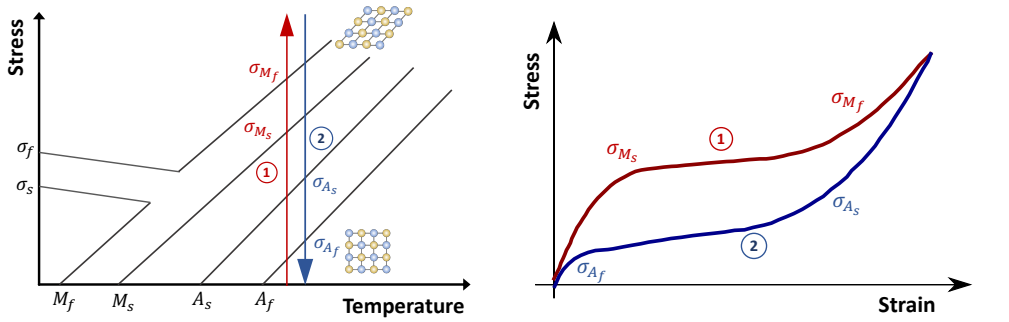

(a) A pseudoelastic loading path

(b) A typical SMA pseudoelastic stress-strain response

Figure 1.8: Psuedoelatic of SMAs

The corresponding stress-strain response in Figure 1.8(b) indicates that the forward phase transformation initiates at stress level (σ_{M_s}) and complete at (σ_{M_f}). The onset of reverse phase transformation is at stress level (σ_{A_s}) and the end is at (σ_{A_f}). According to in Figure 1.8(a), the stress level (σ_{M_s}, σ_{M_f}, σ_{A_s}, σ_{A_f}) are influenced by the temperature and the temperature-stress slope.

1.4 Secondary Features of the Deformation Response of SMAs

1.4.1 Tension-compression asymmetry

The tension-compression asymmetric transformation behavior, which is firstly reported by [109] in 1971, typically expressed a reduced transformation stress and greater transformation strain under tensile testing when compared with compression. In recent decades, experimental and theoretical analytical research has been

performed in macro, micro as well as nano scale of NiTi SMAs. Figure 1.9(b) presents a study of tension-compression of SMAs in nano-scale [103][18], and Figure1.10 indicates macro scale experiment which comparing the average nominal axial stress-strain response under uniaxial tension and compression on tubular specimens. The characteristic is mainly attributed to the crystalline texturing of martensite variants.

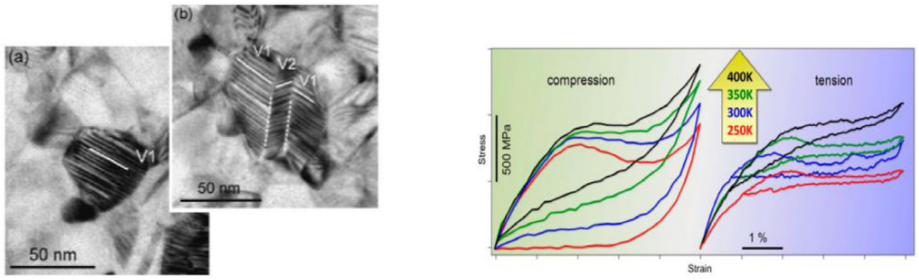

Figure 1.9: Asymmetric research in nano scale from [103] and [18]

In paper [96], the author concluded the tension-compression asymmetric responses of polycrystal NiTi SMAs, they are:

1) Consistent with the Lüders-type deformation, and a transformation stress plateau exists under uniaxial tension. However, for a compressive load, a steady increase in stress can be observed during the transformation,

2) The critical transformation stress for the forward and reverse martensitic transformation and its hysteresis width under uniaxial compression are greater than under uniaxial tension. However, the length of transformation strain is longer under uniaxial tension,

3) Inhomogeneous deformation occurring under uniaxial tension generates a localized propagating transformation front. The deformation under compression is approximately homogeneous without transformation front,

4) The temperature dependence slope of the critical transformation stress is greater under compression than tension.

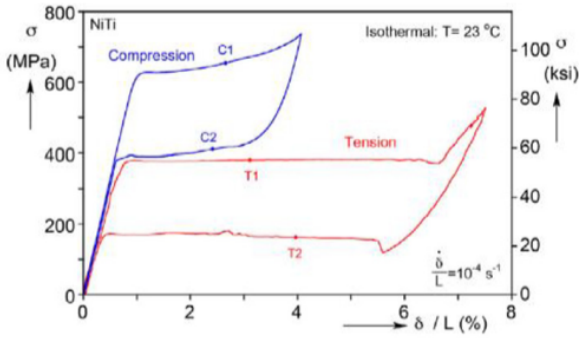

Figure 1.10: Asymmetric research in macro scale from [50]

1.4.2 Minor loops

When SMAs are subjected to cyclic loading, either thermal or mechanical, an important characteristic of SMAs should be considered, which is referred to as minor loops. Minor loops are formed when the phase transformation direction is reversed before the completion of the respective transformation, as illustrated in Figure 1.11. The experiment was performed by Muller and Xu [77], and it considers that states inside the major hysteresis loop are metastable. Partial yielding and recovery occurs whenever the state approaches the line of unstable phase equilibrium from below or from above respectively. Scalet [91] porposed a model based on the assumption that the same energy level state is achieved after a series of loadings, the material also obtains the respective microstructure and, consequently, the same phase.

High attention should be paid on the behavior when designing the SMA actuators, especially for those shape adaptive structural applications which require precise movement to various target shapes and variable amplitude trajectories. And this characteristic is important since it largely affects the amount of generated transformation strains, the actuation frequency , and the fatigue life of the component [53, 90, 14, 91].

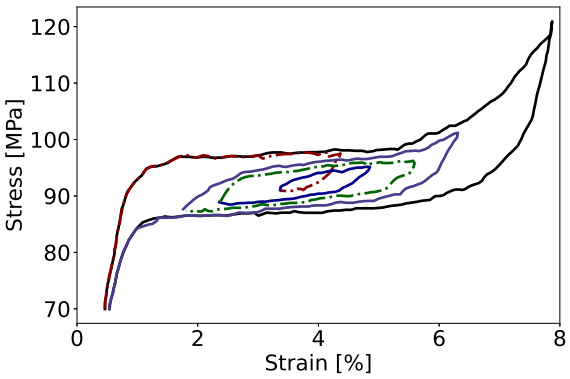

Figure 1.11: Major and a closed minor hysteresis cycle under constant mechanical load [77]

1.4.3 Latent heat effects

As thermomechanical coupling is termed the phenomenon where the thermal response of a structure affects its structural response and vice versa. This phenomenon is prominent in SMA behavior [94, 20, 63, 9, 59, 106] since a mechanical load can provoke the occurrence of marentistic transformation leading to latent heat release/absorbtion and consequently to variation in materials temperature and in the same manner a change in the temperature can lead to structural changes (i.e. shape recovery). This phenomenon is very important since it introduces rate dependent effects in material response despite the rate independent nature of the diffusionless martensitic transformations.

Figure 1.12 demonstrates the experimental DSC data reported by [59], wherein the relative heat flow is plotted as a function of temperature. Heat absorption from martensite to austenite phase transformation results in a ridge along the heating part of the curve, while heat generation from austenite to martensite phase transformation results in a valley along the cooling part. The peak and bottom points on the heating and cooling parts, corresponding to temperatures $\theta_{MA} = 339\ K$ and $\theta_{AM} = 303\ K$ denote average temperatures for forward and reverse phase transformation respectively and the area under the curve in each case, representing phase

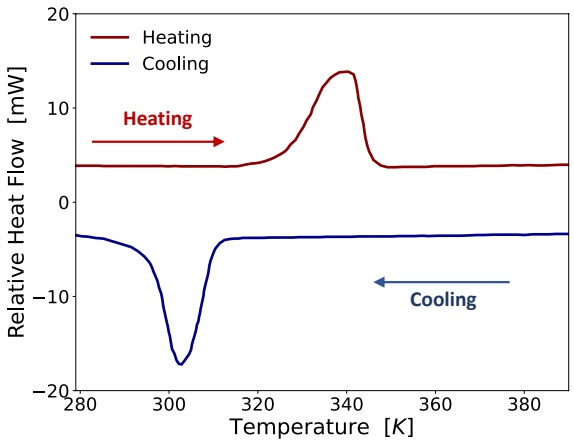

Figure 1.12: Heat generation and absorption (latent heat) during thermal-induced phase transformation [59]

transformation latent heat, which is assumed to be the same.

The phenomenon was also exposed in [94] based on the psuedoelastic loading path. Figure 1.13 illustrates a pseudoelastic uniaxial tensile tests performed on polycrystalline NiTi specimens (50.1 at.% Ni) at three different strain rates $4\% \cdot s^{-1}$, $0.4\% \cdot s^{-1}$, $0.04\% \cdot s^{-1}$. In the referenced experiment, the heat exchange with the surrounding takes place by means of natural air convection with the external temperature maintained at 343 K. The stress-strain response is presented in Figure 1.13(a), and the relative temperature variations is in Figure 1.13(b).

To understand the phenomenon, an explanation is given as follows. If a quasi-static loading is assumed, the temperature changes due to endothermic or exothermic reactions are compensated by the convection between the material and the ambient air, keeping the temperature unchanged. Contrary in dynamic loading paths during the forward transformation the convection is not sufficient to compensate the generated energy due to the exothermic reactions. Therefore, the material temperature is increasing hindering the evolution of transformation and changing materials response. In the same manner during the unloading the temperature of the material is decreasing due to the endothermic reaction which prevents the

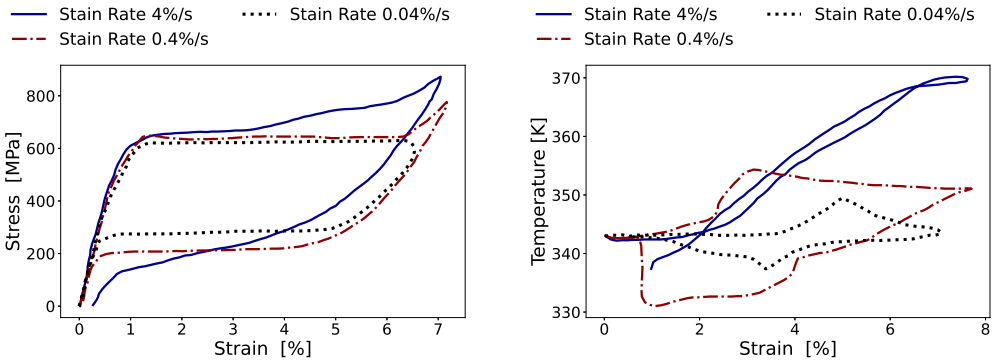

(a) Stress-strain response

(b) Temperature-strain response

Figure 1.13: Thermomechanical coupling response of SMAs at different strain rates reported by [106] and [94]

evolution of the transformation and leads to further changes of the material response. To this end, in dynamic loading paths, SMAs response is expected to deviate significantly in comparison to its quasi-static response due to the presence of strong thermomechanical coupling.

1.5 Tailorable Thermal Expansion of SMAs

Thermal expansion (TE) of SMAs is a critical design factor in engineering applications in which thermal fatigue resistance or dimensional stability over a wide range of temperatures are required [28, 99, 46]. Such applications drive the design of materials and structures with negative TE or zero TE. The most widely known mechanisms that yield negative TE include the magneto-volume effect, atomic radius contraction upon electronic transitions, and flexible networks [100].

Metallic materials that undergo martensitic transformation have been recently shown to exhibit tailorable bulk TE with thermal expansion and contraction ranges projected to achieve TE tensor values between -40 ppmK^{-1} and +50 ppmK^{-1}

due to the TE anisotropy of the low-crystallographic-symmetry martensite lattice [73, 1, 34]. The comparison of the lattice parameter mismatch between austenite and martensite phases can be used to predict the sign and relative magnitude of the thermal expansion rate for any given direction of the martensite lattice. The martensite lattice along a lattice vector direction in which the interatomic distance is greater (lower) than the interatomic distance along the same vector in austenite at the same temperature is observed to contract (expand) when heated. Martensitic materials with anisotropic crystallographic TE include shape memory alloys (SMAs) (*e.g.*, NiTi, NiTiPd, CoNiGa, NiMnGa, and TiNb), α-uranium [64] and lead titanate. In these materials, the TE anisotropy of bulk polycrystals can be exploited through crystallographic and martensite variant texturing upon deformation processing. Materials with ordered martensite can be textured through variant (re)orientation [73]. For example, tensile deformation of a polycrystalline NiTiPd SMA demonstrated sufficient martensite orientation for TE tensor values to change from +14 ppmK^{-1} to -3 ppm K^{-1} after 5% tensile deformation. In materials with disordered martensite, simple deformation processing such as rolling produce crystallographic texturing, creating anisotropically varying (anvar) TE alloys [73, 34].

Figure 1.14 gives an example of thermal expansion evolution according to martensite state at different strain levels. In the experiments [73], the material was uniaxially cyclically strained in tension while at the martensite state. Five loading–unloading cycles were performed with the maximum strain reached in each loading equal to 1.0, 1.9, 2.7, 4.0 and 5.0%, respectively, as shown in Figure 1.14 (a). A heating (420 K)-cooling (300 K) cycle was then performed after each mechanical loading when the material reaches zero stress level. The strain-temperature response was shown in Figure 1.14 (b) and the evolution of thermal

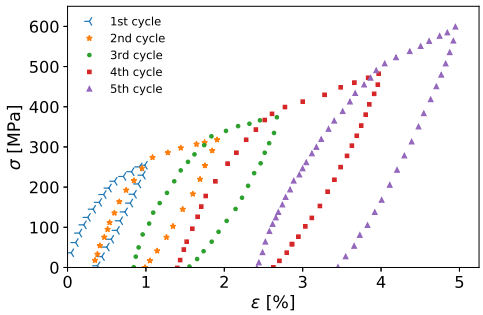

(a) Cyclic stress–strain response

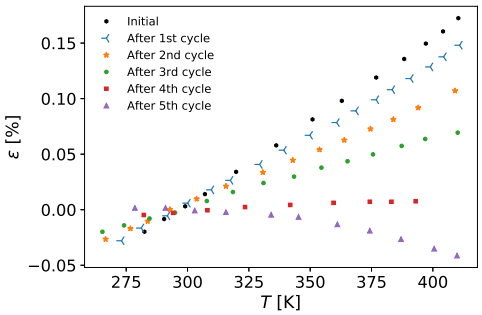

(b) Strain–temperature responses of the undeformed state and after each loading–unloading cycle in the direction of loading

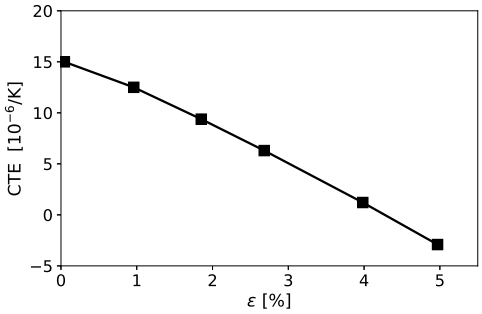

(c) Evolution of the TE tensor component (CTE) in the loading direction, calculated from the strain–temperature response in (b), as a function of the maximum strain achieved in each loading–unloading cycle in (a)

Figure 1.14: NiTiPd response observed in the experiments performed in [73]

expansion attributed to the strain level is presented in Figure 1.14 (c). It is obviously to see that the thermal expansion tensor is highly affected by the magnitude martensite variants. Further researches also indicate that thermal expansion evolves with the directions of martensite variants.

1.6 Constitutive Models of the Thermomechanical Response of SMAs Proposed in Literature

Modeling of the deformation response of SMAs has been an active research field during the last few decades [60, 83, 57, 101, 58, 22, 17, 81, 116, 25, 130, 104, 44,

108, 132]. The majority of the *phenomenological* models addressing the deformation response of polycrystalline SMAS can be characterized as classical *J_2-flow theory based* models. These models rely on continuum thermomechanics with internal variables to account for the changes in the microstructure, do not directly depend on material parameters at the microscopic level, and are easily implementable in numerical methods for the solution of boundary value problems on the structural (macroscopic) level. The choice of the evolution laws for the internal state variables is a key point in their formulation. In general, two main approaches are noteworthy; the *direct*, in which the evolution equations are derived from a postulated "yield" function and the *potential* approach, in which the evolution equations are derived from a "dissipation" potential. The evolution equations are either explicitly integrated or through a minimum principle (*variational* approach).

The finite strain SMA models proposed in literature are based on either the additive split of the rate of deformation [76] or on multiplicative decomposition of the deformation gradient into elastic and inelastic parts [19, 2, 106, 119]. The additive decomposition based finite strain models achieve a simple model structure and an easier implementation procedure, which makes them widely adopted in current available finite element softwares (*e.g.*, Abaqus, ANSYS). To satisfy the principle of objectivity, additive models are required to use an objective rate for integrating the hypoelastic constitutive relation. The Eulerian logarithmic strain, sometimes referred to as true or natural or Hencky strain, is the only strain measure that its corotational rate (associated with the so-called logarithmic spin) is the rate of deformation tensor, also-called stretching [89, 112]. Other stress objective rates (*e.g.*, Zaremba-Jaumann-Noll rate, Green-Naghdi-Dienes rate, and Truesdell rate) combined with the rate of deformation may result in spurious phenomena (*e.g.*, shear stress oscillation, artificial stress residuals, *etc*). Moreover, only the

spherical and the deviatoric parts of the Hencky strain can, in an additive manner, separate the volumetric deformation and the isochoric deformation from the total deformation [113] and it is the only finite strain measure that satisfies the so-called Seth-Hill requirements that strain should approach $+\infty$ ($-\infty$) when the stretch approaches $+\infty$ (0) [24].

Variant orientation is the main inelastic mechanism during proportional mechanical loading of self-accommodated martensite and variant reorientation has a significant influence in the deformation response of SMAs during non-proportional loading [102, 61, 41, 42, 35]. Experimental evidence under various loading paths, such as tension–torsion, axial–shear, and biaxial paths [102, 41, 42, 35] have been reported in literature highlighting the reorientation response of SMAs. Constitutive models accounting for orientation include [84, 128, 74, 107] and those accounting for reorientation include [3, 16, 127, 92, 5, 125, 48]. At the single crystal level, the tension–compression asymmetry reported in literature [21, 82, 45] is rooted in differences in the (re)orientation/detwinning response of different habit plane variants, their unidirectional nature[1], and the size of precipitates [33, 31]. At the polycrystalline level it is further rooted in texture [62]. Models that account for tension–compression asymmetry include [6, 27, 129, 48]. In general the deformation response of SMAs is non-linear, path-dependent, and hysteretic. The hysteresis originates from energy dissipation accompanying phase transformation, mainly caused by friction associated with the movement of austenite–martensite interfaces. Models describing the hysteretic response under minor/partial/inner loops, *i.e.*, loops involving partial phase transformation as opposed to the major loops that involve full phase transformation, can be roughly distinguished to (i) Preisach models [68, 88], (ii) Duhem–Madelung models [26, 29, 69], and (iii)

[1] in contrast to dislocation slip, for example, that may occur in either the positive or negative direction on a slip plane, the polar nature of the atomic arrangements for phase transformation results in its unidirectional nature.

thermodynamically-based continuum mechanics models [9, 97, 51, 65, 52]. As already mentioned, phase transformation can result in self-heating or self-cooling of the alloy, depending on the transformation direction, with immediate consequences on the deformation response. The isothermal assumption is valid for a range of strain rates within the regime of quasi-static processes at room temperature even for complex geometries and loadings [85]. At higher strain rates, the generation or absorption of latent heat may have a strong impact on the deformation response and the stress–strain hysteresis loop area of SMAs, as shown experimentally in [93, 85, 38]. The rate dependence of hysteresis has been shown to be actually non-monotonic with a hysteresis peak at an intermediate strain rate which depends on ambient conditions and the minimum hysteresis at adiabatic conditions [40, 39, 120, 122]. Thermomechanical coupling has been accounted for in [7, 131, 16, 74, 75, 121, 124, 105, 123].

SMAs have been recently shown to exhibit tailorable bulk thermal expansion (TE) response (through crystallographic and martensite variant texturing) with thermal expansion and contraction ranges projected to achieve TE tensor values between -40 ppm $ppm\ K^{-1}$ and +50 ppm $ppm\ K^{-1}$ due to the crystallographic TE anisotropy of the low-crystallographic-symmetry martensite [73, 1, 34]. A micromechanics-based single crystal model was proposed to describe the TE evolution in NiTiPd during (re)orientation of martensite variants [126]. The single crystal's averaged TE tensor was approximated by the isotropic coefficient of TE of the high-crystallographic-symmetry austenite (B2), the anisotropic TE tensor of martensite (B19) (in the local coordinate system of each variant), the transformation relationships between a global coordinate system and each variant's, and the volume fraction of the variants forming in the crystal. In order to reduce the computational cost of the model in simulating the TE of polycrystalline aggregates, the authors further proposed a rate-dependent self-consistent scale-transition scheme.

The extension of these models to other SMA material systems entails substantial complexity in their construction, numerical implementation, and, particularly, parameter calibration at the microscopic level. Herein, a macroscale phenomenological model within the framework of irreversible thermodynamics with internal state variables is alternatively proposed, in which physical rigor in its formulation is offset by simplicity and reduced calibration (and in turn experimental) and computational effort in capturing the overall TE response of polycrystalline SMAs. The TE response description in the model relies on the volume fraction of the most prevalent martensite variants and a macroscopic description of the "effective" orientation of the martensite variants. The common assumption in the macroscopic models for the deformation response of SMAs, *e.g.*, [57, 58, 3, 74, 4, 15], has been that of a constant, isotropic TE tensor for martensite.

1.7 Motivation and Outline of the Dissertation

SMAs have been traditionally desirable in engineering applications that can take advantage of the martensitic transformation occuring in these intermetallics under appropriate stimuli. The recent discovery that SMAs exhibit tailorable bulk TE renders SMAs desirable as low-CTE materials in engineering applications in which dimensional stability is of outmost importance.

In order to ultimately realize the true potential of SMAs in engineering applications as "smart" or low-CTE materials, constitutive models capable of effectively describing their response to thermomechanical stimuli are needed to enable efficient design of SMA-based devices. Although there are constitutive models proposed in literature that address most of the aspects of the deformation response of SMAs, none includes in a single formulation all those ones that are collectively important under complex non-proportional thermo-mechanical loading and none

can facilitate choosing deformation processing routes to achieve targeted CTE values.

The motivation of the present work is, thus, to address the aforementioned limitations of existing constitutive models in i) adequately describing the deformation response of SMAs under complex non-proportional thermo-mechanical loading conditions, and ii) tailoring the CTE of SMAs during deformation processing. The proposed model is based on the Eulerian logarithmic strain and the corotational logarithmic objective rate and can efficiently describe the main inelastic processes associated with the thermomechanical deformation response of SMAs, *i.e.*, the growth/shrinking, orientation, and reorientation of variants. The model adopts the magnitude of the inelastic strain, its direction, and the volume fraction of martensite as internal state variables, allowing for an implicit description of a fourth, the volume fraction of oriented martensite. The resulting constitutive response describes superelasticity, *one-way shape memory effect*[2], orientation, reorientation, tension-compression asymmetry, latent heat effect, and minor loops assuming isotropic material responses, neglecting ferroelasticity, plasticity, cyclic evolution, and irreversible strains due to retained martensite. The model can further describe a number of secondary effects associated with phase transformation, such as smooth thermomechanical response, dependence of hysteresis width on bias load level under thermomechanical loading (and on temperature in isothermal mechanical loading), asymmetry between forward and reverse phase transformation, and it is flexible one to address the deformation response in the presence of all phases, *i.e.*, when austenite, self-accommodated and oriented martensite co-exist in the microstructure. Moreover, the model can capture the overall TE

[2]in which forward phase transformation under no externally applied mechanical load results in self-accommodated martensite as opposed to the acquired characteristic of the *two-way shape memory effect* in which phase transformation results in oriented martensite even in the absence of an externally applied mechanical load.

response of SMAs based the volume fraction of oriented martensite and a macroscopic description of the "effective" orientation of the martensite variants.

The dissertation is organized as follows,

- Chapter 2 presents a brief review of the fundamental elements for the constitutive modeling of SMAs. These fundamental elements consist of the basic kinematics from continuum mechanics, strain measure, the adopted objective rate, and the basic principles of thermodynamics.

- Chapter3 is the proposition of a finite strain constitutive model for polycrystalline SMAs. The model is developed through classical thermodynamic laws combined with the standard Coleman-Noll procedure. The scalar martensitic volume fraction ξ, effective inelastic strain magnitude H^{cur}, scalar variable λ^r associated with reorientation and the second-order inelastic strain tensor $\boldsymbol{h}^{in}$ are chosen as the internal state variables to capture the material response including forward/reverse phase transformation, orientation and reorientation. The anisotropic thermal expansion of SMAs are predicted based on the assumption that thermal expansion evaluates with the orientation of martensite variants.

- Chapter 4 focuses on the return mapping algorithm of the constitutive model. The numerical implementation is demonstrated in three sections. Pre-calculation of the finite strain calculators is firstly introduced, including the calculation of logarithmic rate and the according rotation tenor. The return mapping algorithm is described in the second part. Finally, the consistent tangent moduli tensors are listed.

- Chapter 5 presents the numerical simulations to validate the proposed model against experimental results and verify the stability and efficiency of the numerical algorithm. The model's capability to capture all the aspects of the

martensitic transformation, including the major thermomechanical response (phase transformation and shape memory effect) together with their inherent characteristics (tension-compression asymmetry, minor loops, latent heat effect, phase transformation asymmetry between forward and reverse, temperature and load dependence of the hysteresis width, temperature dependence of the critical force required for (re)orientation) is demonstrated. The model is validated against the experimental results on the deformation response of SMAs under complex multiaxial non-proportional loading conditions, such as tension/compression/torsion box loading. The results indicate that the model significantly improves the prediction accuracy by accounting for all the aforementioned aspects and highlight their collective importance under non-proportional loading conditions. Furthermore, the validation of the proposed model on tailoring the TE evolution response is presented. The model also shows its ability to tailor the TE coefficient during non-proportional deformation processing. Finally, three simulations of complicated 3D structures (spring actuator, self-expanding stent and SMAs tube buckling) are introduced to verify the stability of numerical algorithm.

- Chapter 6 provides summaries and conclusions of this dissertation.

2 PRELIMINARIES

2.1 Kinematics

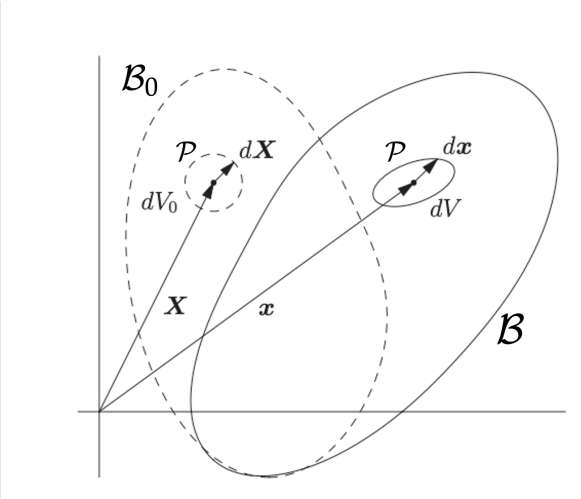

Figure 2.1: The schematics of mapping material point $\boldsymbol{X}$ in the reference configuration to the spatial point $\boldsymbol{x}$ in the deformed configuration

In this section, we adopt the symbol $\mathcal{B}$ refers to as the material body. S and V indicates the surface and volume of the body respectively (see in Fig. 2.1). A body $\mathcal{B}$ can take on many different shapes or configurations depending on the loading applied to it. We choose one of these configurations to be the reference configuration of the body and label it $\mathcal{B}_0$. The reference configuration provides a convenient fixed state of the body to which other configurations can be compared to gauge their deformation, typically it corresponds to the state where no external loading is applied to the body at time t_0. We denote the position of a particle $\mathcal{P}$ in the reference configuration by $\boldsymbol{X} = \boldsymbol{X}(\mathcal{P})$. Since particles cannot be formed or destroyed, we can use the coordinates of a particle in the reference configuration as a label distinguishing this particle from all others. Once we have defined the reference configuration, the deformed configuration at time t occupied by the body is described in terms of a deformation mapping function that maps the

reference position of every particle $\boldsymbol{X} \in \mathcal{B}_0$ to its deformed position $\boldsymbol{x}$,

$$\boldsymbol{x} = \boldsymbol{x}(\boldsymbol{X}, t). \tag{2.1}$$

Therefore, the deformation process of point $\mathcal{P}$ between the reference configuration and the current configuration can be defined through the well-known deformation gradient tensor $\boldsymbol{F}(\boldsymbol{x}, t)$,

$$\boldsymbol{F}(\boldsymbol{x}, t) = \frac{\partial \boldsymbol{x}}{\partial \boldsymbol{X}}. \tag{2.2}$$

The deformation gradient $\boldsymbol{F}$ can be divided into the polar decomposition equation,

$$\boldsymbol{F} = \boldsymbol{R}\boldsymbol{U} = \boldsymbol{V}\boldsymbol{R}, \tag{2.3}$$

where $\boldsymbol{R}$ is an orthogonal tensor, which is called the rotation tensor, $\boldsymbol{U}$ and $\boldsymbol{V}$ are the right (or Lagrangian) or left (or Eulerian) stretch tensor, respectively. The polar decomposition indicates that any admissible deformation processes for the continuous body can be decomposed into a pure rigid body rotation followed by a pure stretch, *i.e.*, $\boldsymbol{F} = \boldsymbol{V}\boldsymbol{R}$, or into a pure stretch first followed by a rigid body rotation, *i.e.*, $\boldsymbol{F} = \boldsymbol{R}\boldsymbol{U}$.

The spectrum decomposition of the left/right stretch tensors can be received as following, for right stretch $\boldsymbol{U}$,

$$\boldsymbol{U} = \sum_{i=1}^{3} \lambda_i \boldsymbol{Q}_i \otimes \boldsymbol{Q}_i, \tag{2.4}$$

and for left stretch $\boldsymbol{V}$,

$$\boldsymbol{V} = \sum_{i=1}^{3} \lambda_i \boldsymbol{q}_i \otimes \boldsymbol{q}_i, \tag{2.5}$$

where the scalars $\{\lambda_1,\ \lambda_2,\ \lambda_3\}$ are called the principal stretches which are the

eigenvalues of $\boldsymbol{U}$ and $\boldsymbol{V}$, and the unit base vectors $\{\boldsymbol{Q}_1,\ \boldsymbol{Q}_2\ \boldsymbol{Q}_3\}$ and $\{\boldsymbol{q}_1,\ \boldsymbol{q}_2\ \boldsymbol{q}_3\}$ are called, respectively, the Lagrangian and Eulerian triads dictating the Lagrangian and Eulerian principal directions.

The right Cauchy-Green tensor $\boldsymbol{C}$ and the left Cauchy-Green tensor $\boldsymbol{b}$ can be obtained based on the left/right stretch tensors, as follows:

$$\boldsymbol{C} = \boldsymbol{F}^T\boldsymbol{F} = \boldsymbol{U}^2, \tag{2.6}$$

$$\boldsymbol{b} = \boldsymbol{F}\boldsymbol{F}^T = \boldsymbol{V}^2. \tag{2.7}$$

Considering the kinematics rate, the velocity field $\boldsymbol{v}(\boldsymbol{x}, t)$ of a motion is defined as,

$$\boldsymbol{v} = \frac{d\boldsymbol{x}}{dt} = \dot{\boldsymbol{x}}, \tag{2.8}$$

and the gradient of the velocity $\boldsymbol{v}$ can be derived as,

$$\boldsymbol{l} = \nabla\boldsymbol{v}(\boldsymbol{x}, t) = \frac{\partial \boldsymbol{v}}{\partial \boldsymbol{x}} = \dot{\boldsymbol{F}}\boldsymbol{F}^{-1}, \tag{2.9}$$

where $\boldsymbol{l}$ is the velocity gradient.

The velocity gradient $\boldsymbol{l}$ can be additively decomposed into a symmetric part, the stretching (rate of deformation) tensor $\boldsymbol{d}$ and an anti-symmetric part, the spin tensor $\boldsymbol{w}$, which are defined as:

$$\boldsymbol{l} = \boldsymbol{d} + \boldsymbol{w}, \quad \boldsymbol{d} = \frac{1}{2}(\boldsymbol{l} + \boldsymbol{l}^T), \quad \boldsymbol{w} = \frac{1}{2}(\boldsymbol{l} - \boldsymbol{l}^T). \tag{2.10}$$

2.1.1 Strain measures

There are many different strain measures available in the literature, and there is by no means a unique method of defining strain. In fact, a specific choice of

strain measure is usually willful and mainly controlled by its mathematical convenience for specific model construction. Despite the various preferences on different strain measures, two major categories can be listed based on their formulation triads. A category of strain measure is introduced as Lagrangian strain tensors as follows, *i.e.*, strain measures formulated by using Lagrangian triads. The Eulerian strain tensors which have the Eulerian principal directions, i.e., strain measures formulated based on the Eulerian triads [80, 43]. Based on the left stretch, the Eulerian strain tensors are defined as Eqn.(2.11)[3]

$$\boldsymbol{e}^{(m)} = \begin{cases} \frac{1}{m}(\boldsymbol{V}^m - \boldsymbol{I}); & m \neq 0, \\ \ln(\boldsymbol{V}); & m = 0. \end{cases} \tag{2.11}$$

The Eulerian strain tensors can be reformulated by virtue of the principal stretches and Eulerian triads as,

$$\boldsymbol{e}^{(m)} = \sum_{i=1}^{3} f(\lambda_i)\boldsymbol{q}_i \otimes \boldsymbol{q}_i, \tag{2.12}$$

where $f(\lambda_i)$ is defined as,

$$f(\lambda_i) = \begin{cases} \frac{1}{m}(\lambda_i^m - 1); & m \neq 0, \\ \ln\lambda_i; & m = 0, \end{cases} \tag{2.13}$$

λ_i and $\boldsymbol{q}_i$ is the principal stretches and unit base vectors of left stretch tensor $\boldsymbol{V}$ defined in Eqn. (2.5). Commonly utilized strain measures can also be deduced from the discussed strain family. For examples, Hencky strain with $m = 0$, the Biot strain with $m = 1$, and Almansi strain with $m = -2$.

[3]In this equation, the logarithm of a tensor is defined and the definition is as follows: given a tensor $\boldsymbol{\mathcal{B}}$, another tensor $\boldsymbol{\mathcal{A}}$ is said to be a tensor logarithm of $\boldsymbol{\mathcal{B}}$ if $\boldsymbol{\mathcal{B}} = e^{\boldsymbol{\mathcal{A}}}$, where $e^{\boldsymbol{\mathcal{A}}} = \sum_{n=0}^{\infty} \frac{\boldsymbol{\mathcal{A}}^n}{n!}$.

The proposed finite strain constitutive model is based on the Eulerian logarithmic strain (Hencky strain),

$$\boldsymbol{h} = \ln(\boldsymbol{V}) = \frac{1}{2}\ln \boldsymbol{b} = \frac{1}{2}\sum_{i=1}^{n} \ln \lambda_i \boldsymbol{b}_i, \tag{2.14}$$

which is introduced as the logarithmic measure of the left Cauchy-Green deformation tensor Eqn. (2.14) (λ_i are the n distinct eigenvalues of $\boldsymbol{b}$, and $\boldsymbol{b}_i$ are the corresponding eigenprojections $\boldsymbol{b}_i = \boldsymbol{q}_i \otimes \boldsymbol{q}_i$ expressed by the eigenvectors $\boldsymbol{q}_i$).

2.1.2 Stress measures

Motions are accompanied by forces. Classically, forces in continuum mechanics are described spatially by [36]:

(i) contact forces between adjacent spatial regions; that is, spatial regions that intersect along their boundaries;

(ii) contact forces exerted on the boundary of the body by its environment;

(iii) body forces exerted on the interior points of a body by the environment.

Those body forces are exerted throughout the entire continua regardless of its location and time and measured per volume in the reference body. Contact forces per unit area in the deformed body and described in conception of stress.

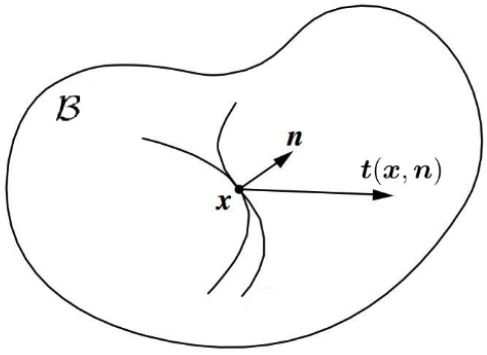

Figure 2.2: The schematics of traction forces at current configuration

One of the most basic axioms in continuum mechanics is **Cauchy's stress principle** which states that there exists a linear relationship between the surface traction $\boldsymbol{t}(\boldsymbol{x}, \boldsymbol{n})$ and the unit normal vector $\boldsymbol{n}$ (see in Fig. 2.2), in other words, there is a second-order tensor field $\boldsymbol{\sigma}$ such that the traction vector is given by

$$\boldsymbol{t}(\boldsymbol{x}, \boldsymbol{n}) = \boldsymbol{\sigma}(\boldsymbol{x})\boldsymbol{n}. \tag{2.15}$$

Cauchy stress tensor is defined in the deformed configuration and valid only in an averaging sense for a sufficiently representative volume of material.

Another important stress measure that has the same principal directions as Cauchy stress tensor is the **Kirchhoff stress tensor** $\boldsymbol{\tau}$ defined in the Eqn. (2.16), wherein J is the determinant of the deformation gradient $\boldsymbol{F}$, *i.e.*, $J = \text{Det } |\boldsymbol{F}|$. The scalar value J gives the volume change of a particle. Therefore, $\boldsymbol{\tau}$ is also an Eulerian variable defined in the current configuration,

$$\boldsymbol{\tau} = J\boldsymbol{\sigma}. \tag{2.16}$$

The Kirchhoff stress tensor is regarded as an energetic conjugate pair with the Hencky strain of its Eulerian type $\boldsymbol{h}$ (discussed in Section 2.22), and they are utilized as stress and strain measures in the formulation of the proposed constitutive model for SMAs.

2.1.3 Objective rate–logarithmic strain, logarithmic rate and logarithmic spin

Two kinematic assumptions, *i.e.*, the multiplicative decomposition of deformation gradient $\boldsymbol{F}$ ($\boldsymbol{F} = \boldsymbol{F}^e\boldsymbol{F}^{in}$)[4] and the additive decomposition of the rate of deformation tensor $\boldsymbol{d}$ ($\boldsymbol{d} = \boldsymbol{d}^e + \boldsymbol{d}^{in}$), are usually used in finite deformation theory. Hyperelastic constitutive relation is often used in multiplicative models while

[4]The superscript ^{e} contributes to the elastic part and ^{in} contributes to the inelastic part.

hypoelastic constitutive equation is utilized for additive models.

The hypoelastic constitutive equations are more straight forward way and designed in the form of a relation between a stress-rate and a strain-rate (or the rate of deformation tensor). However, the "objective" of the rate form should be carefully considered. The mechanical response of a material should not depend on the frame of reference. In other words, material constitutive equations should be frame-indifferent (objective). If the stress and strain measures are Lagrangian quantities then objectivity is automatically satisfied. However, if the quantities are spatial (Eulerian), then the objectivity of the stress-rate and strain-rate may not be guaranteed. Many well-known objective stress rates are proposed in literature, such as Zaremba-Jaumann rate, Green-Naghdi rate, and Truesdell rate, *etc.*. However, the theories have been criticized for its failure to be fully integrable to describe a simple recoverable elastic behavior. Many spurious phenomenons, such as shear stress oscillation, dissipation or stress errors are observed in simple elastic deformation [114].

The aforementioned issues regarding objective rates are resolved via the logarithmic rate proposed by [114, 112, 111, 10, 11, 12, 70, 71]. The Eulerian logarithmic (Hencky) strain is the only strain measure whose objective time rate with respect to a corrotational frame yields the total stretching (or rate of deformation) $\boldsymbol{d}$, which is defined in Eqn. (2.10)

$$\mathring{\boldsymbol{h}} = \dot{\boldsymbol{h}} + \boldsymbol{h}\boldsymbol{\Omega}^L - \boldsymbol{\Omega}^L\boldsymbol{h} = \boldsymbol{d}, \tag{2.17}$$

where the superscript "$\circ$" denotes the objective logarithmic time rate of any tensor $\boldsymbol{a}$,

$$\mathring{\boldsymbol{a}} = \dot{\boldsymbol{a}} + \boldsymbol{a}\boldsymbol{\Omega}^L - \boldsymbol{\Omega}^L\boldsymbol{a}, \tag{2.18}$$

defined by the logarithmic spin $\boldsymbol{\Omega}^L = \boldsymbol{w} + \sum_{\alpha\neq\beta}^{n} \left(\frac{1+(\lambda^\alpha/\lambda^\beta)}{1-(\lambda^\alpha/\lambda^\beta)} + \frac{2}{\ln(\lambda^\alpha/\lambda^\beta)} \right) \boldsymbol{b}^\alpha \boldsymbol{d}\boldsymbol{b}^\beta$, and "$\dot{}$" denotes material time rate.

On account of Eqn. (2.18), relation

$$\dot{\overline{\boldsymbol{R}^{L^T} \boldsymbol{a} \boldsymbol{R}^L}} = \boldsymbol{R}^{L^T} \mathring{\boldsymbol{a}} \boldsymbol{R}^L \tag{2.19}$$

holds, where the logarithmic rotation, $\boldsymbol{R}^L$, is defined from the differential equation

$$\dot{\boldsymbol{R}}^L = \boldsymbol{\Omega}^L \boldsymbol{R}^L; \;\; \boldsymbol{R}^L|_{t=0} = \boldsymbol{\delta}. \tag{2.20}$$

The left hand side of Eqn. (2.19) represents the material time rate of a Lagrangian quantity and, thus, Eqn. (4.1) generates a one-parameter subgroup of rotations that define a locally rotating coordinate system in which the material time rates of the obtained rotated tensors remain unaltered by superposed spatial rigid body motions [115]. Time integration of Eqn. (2.19), assuming $\boldsymbol{a} = \boldsymbol{h}$ and $\boldsymbol{h}|_{t=0} = \boldsymbol{0}$, yields

$$\boldsymbol{h} = \boldsymbol{R}^{L^T} \left(\int_0^t \boldsymbol{R}^L \mathring{\boldsymbol{h}} \boldsymbol{R}^{L^T} \mathrm{d}t \right) \boldsymbol{R}^L \overset{2.17}{=} \boldsymbol{R}^{L^T} \left(\int_0^t \boldsymbol{R}^L \boldsymbol{d} \boldsymbol{R}^{L^T} \mathrm{d}t \right) \boldsymbol{R}^L. \tag{2.21}$$

2.2 Stress Power

The stress power per unit volume at deformed configuration $\mathcal{B}$ is given by

$$\dot{W} = J\boldsymbol{\sigma} : \boldsymbol{d} = \boldsymbol{\tau} : \boldsymbol{d}. \tag{2.22}$$

Here, W is the stress power, $\boldsymbol{\sigma}$ is the Cauchy stress and $\boldsymbol{\tau} = J\boldsymbol{\sigma}$ the Kirchhoff stress (see in Section 2.1.2).

Eqn. (2.22) describes a physical quantity, the rate of work of the stresses on the body. However, this expression for stress power is difficult to incorporate in the

formulation of constitutive laws as it is based on the rate of stretching $\boldsymbol{d}$. Hence, to fulfill the conservation of energy requirement in formulating constitutive laws, relation Eqn.(2.17) is introduced to Eqn.(2.22) to give

$$\dot{W} = \boldsymbol{\tau} : \mathring{\boldsymbol{h}}. \tag{2.23}$$

The additive decomposition of $\boldsymbol{d}$ (*e.g.*, $\boldsymbol{d} = \boldsymbol{d}^e + \boldsymbol{d}^{in}$) also allows to split the rate of work according to

$$\dot{W} = \dot{W}^e + \dot{W}^{in} = \boldsymbol{\tau} : (\boldsymbol{d}^e + \boldsymbol{d}^{in}), \tag{2.24}$$

where $\dot{W}$ is related to the elastic part of the stress power,

$$\dot{W}^e = \boldsymbol{\tau} : \boldsymbol{d}^e = \boldsymbol{\tau} : \mathring{\boldsymbol{h}}^e, \tag{2.25}$$

and $\boldsymbol{h}^e$ is the reversible elastic part of the Hencky strain.

We note in passing that with Eqn.(2.23) the above mentioned shortcoming of the Eulerian formulation can be overcome, namely, the stretching $\boldsymbol{d}$ can be expressed as logarithmic rate of the Hencky strain $\boldsymbol{h}$. This allows in a very straightforward manner to extend the classical description of elastic–inelastic material for small deformations, including the whole thermomechanical frame, to finite deformations. We therefore have to replace in these relations the infinitesimal strain $\boldsymbol{\varepsilon}$ by Hencky strain $\boldsymbol{h}$ and the material time derivative of any tensorial quantity by the logarithmic rate of these tensors.

2.3 Fundamental Principles of Continuum Mechanics

The basic physical laws that govern the behavior of continuum systems are [98, 117]:

1. Conservation of mass,
2. Balance of Linear Momentum,
3. Balance of Angular Momentum,
4. Conservation of Energy (First principle of Thermodynamics),
5. Entropy Inequality (Second principle of Thermodynamics).

According to the the definition of undeformed configuration ($\mathcal{B}_0$) and deformed configuration ($\mathcal{B}$) in Section 2 (See Fig. 2.1), tensor fields can be described in the referential (material) form based on $\boldsymbol{X}$ and spatial form based on $\boldsymbol{x}$. The time derivative of fields exist particularly apparent difference between the two descriptions. Consider a field $\mathbf{g}$, which can be written within the material or spatial descriptions,

$$\mathbf{g} = g(\boldsymbol{x}, t) = \breve{g}\left(\boldsymbol{X}, t\right), \tag{2.26}$$

here $\mathbf{g}$ represents the value of the field variable, while g and $\breve{g}$ represent the functional dependence of $\mathbf{g}$ on specific arguments. There are two possibilities for taking a time derivative:

$$\left.\frac{\partial \breve{g}\left(\boldsymbol{X}, t\right)}{\partial t}\right|_{X}, \tag{2.27}$$

material time derivative, which $\boldsymbol{X}$ is held fixed during the partial derivative; or

$$\left.\frac{\partial g\left(\boldsymbol{x}, t\right)}{\partial t}\right|_{x}, \tag{2.28}$$

local rate of change of $\mathbf{g}$, of which the rate of change is held fixed at spatial position $\boldsymbol{x}$.

The material time derivative is the appropriate derivative to use whenever considering the time rate of change of properties tied to the material itself, and it

is denoted as Eqn. (2.29) in the following section,

$$\frac{D\mathbf{g}}{Dt} = \frac{\partial \breve{g}(\boldsymbol{X}, t)}{\partial t} \tag{2.29}$$

In some cases, it may be necessary to compute the material time derivative within a spatial description. This can be readily done by using the chain rule,

$$\begin{aligned} \frac{D\mathbf{g}}{Dt} = \frac{Dg(\boldsymbol{x}(\boldsymbol{X}, t), t)}{Dt} &= \frac{\partial g(\boldsymbol{x}, t)}{\partial t} + \frac{\partial g(\boldsymbol{x}, t)}{\partial \boldsymbol{x}_j} \frac{\partial \boldsymbol{x}_j(\boldsymbol{X}, t)}{\partial t} \\ &= \frac{\partial g(\boldsymbol{x}, t)}{\partial t} + \frac{\partial g(\boldsymbol{x}, t)}{\partial \boldsymbol{x}_j} \boldsymbol{v}_j(\boldsymbol{x}, t). \end{aligned} \tag{2.30}$$

Conservation of Mass

This principle indicates that mass is a fixed quantity that cannot be formed or destroyed, but only deformed by the applied loads. That means the mass of a continua keeps constant from one configuration to the next,

$$m_0(\mathcal{B}_0) = m(\mathcal{B}), \tag{2.31}$$

then the rate of mass is equal to zero. According to the Eqn.(2.30), time derivative in local (spatial) form is written as,

$$\dot{m} = \int_V \dot{\rho} + \rho(\boldsymbol{\nabla} \cdot \ [\boldsymbol{v}]) dV = 0, \tag{2.32}$$

where $\boldsymbol{v}$ is the velocity fields of the material point, and $\boldsymbol{\nabla} \cdot \ [\boldsymbol{v}]$ represents the divergence of the velocity field, and ρ is the density of the material in the deformed configuration $\mathcal{B}$. The conservation of mass in spatial form can be written as Eqn. (2.33),

$$\frac{\partial \rho}{\partial t} + (\boldsymbol{\nabla} \cdot \ [\rho \boldsymbol{v}]) = 0. \tag{2.33}$$

Balance of Linear Momentum

Balance of linear momentum indicates that the rate change of linear momentum of a continuum system is equal to the total external force acting on the system, including the body forces as well as the traction act on the surfaces. The expression can be given as,

$$\frac{D}{Dt}\int_V \rho \boldsymbol{v}\, dV = \int_V \rho\, \boldsymbol{b}_{\mathcal{B}}\, dV + \int_{\partial V} \boldsymbol{t}\, dS, \tag{2.34}$$

where $\boldsymbol{b}_{\mathcal{B}}$ is the body force [5] field act on the entire system, and $\boldsymbol{t}$ is the traction act on the surfaces. According to Eqn. (2.30), the left hand side item can be written as,

$$\begin{aligned}\frac{D}{Dt}\int_V \rho \boldsymbol{v}\, dV &= \int_V \dot{\overline{\rho}\overline{\boldsymbol{v}}} + \rho \boldsymbol{v}\boldsymbol{\nabla}\cdot[\boldsymbol{v}]\, dV \\ &= \int_V \rho\dot{\boldsymbol{v}} + \underbrace{(\dot{\rho} + \rho\boldsymbol{\nabla}\cdot[\boldsymbol{v}])}_{=0;\text{ based on Eqn.(2.32)}} \boldsymbol{v}\, dV \\ &= \int_V \rho\dot{\boldsymbol{v}}\, dV.\end{aligned} \tag{2.35}$$

The expression

$$\frac{D}{Dt}\int_V \rho \boldsymbol{g}\, dV = \int_V \rho\dot{\boldsymbol{g}}\, dV \tag{2.36}$$

is referred to as **Reynolds transport theorem**, where $\boldsymbol{g}$ can be any fields in spatial description.

The the balance of linear momentum Eqn.(2.34) can be written in local form as follows,

$$\rho\, \boldsymbol{a}_{\mathcal{B}} = \boldsymbol{\nabla}\cdot\boldsymbol{\sigma} + \rho\, \boldsymbol{b}_{\mathcal{B}}, \tag{2.37}$$

where $\boldsymbol{a}_{\mathcal{B}}$ is the acceleration field of the material point.

Balance of angular momentum

[5] We use specific form of $\boldsymbol{b}_{\mathcal{B}}$ and $\boldsymbol{a}_{\mathcal{B}}$ to distinguish them from the symbols $\boldsymbol{b}$ and $\boldsymbol{a}$ defined in the following constitutive model

The balance of angular momentum states that the change in angular momentum of a system is equal to the resultant moment applied to it,

$$\frac{D}{Dt}\boldsymbol{H_0} = \boldsymbol{M}_0^{ext}, \tag{2.38}$$

where the left hand side expression represents the angular momentum of the system about the origin,

$$\frac{D}{Dt}\boldsymbol{H_0} = \frac{D}{Dt}\int_V \boldsymbol{x} \times (\rho \dot{\boldsymbol{x}})\ dV, \tag{2.39}$$

and the right hand side represents the total external moment about the origin,

$$\boldsymbol{M}_0^{ext} = \int_V \boldsymbol{x} \times (\rho\ \boldsymbol{b}_{\mathcal{B}})\ dV + \int_{\partial V} \boldsymbol{x} \times \boldsymbol{t}\ dS. \tag{2.40}$$

Based on Eqn.(2.30), we obtain balance of angular momentum in local form Eqn. (2.41) , which implies that Cauchy stress tensor is symmetric,

$$\boldsymbol{\sigma} = \boldsymbol{\sigma}^T. \tag{2.41}$$

First Principle of Thermodynamics

The first law of thermodynamics is also called the principal of conservation of energy, states that the rate of change of summation of kinetic and internal energy for the continua is equal to the summation of the rate of work applied by surface and body forces, rate of heat flow across the boundary, and heat supply within the body. The integral form of this principal can be expressed as follows,

$$\frac{D}{Dt}\int_V \left(\frac{1}{2}\rho \boldsymbol{v}^2 + \rho u\right) dV = \int_{\partial V} \boldsymbol{t} \cdot \boldsymbol{v} dS + \int_V\ \rho \boldsymbol{b}_{\mathcal{B}}\ \cdot \boldsymbol{v} dV - \int_{\partial V} (\boldsymbol{q} \cdot \boldsymbol{n}) dS + \int_V \rho r dV. \tag{2.42}$$

In the proceeding equation, u is the internal energy per unit mass, $\boldsymbol{q}$ is the heat

flux vector, r is the heat supply per unit mass, $\boldsymbol{n}$ is a unit normal vector on the body surface ∂V, $-(\boldsymbol{q}\cdot\boldsymbol{n})$ indicates the rate of heat flowing into the body.

The kinetic energy in left hand side can be written in the following form based on Reynolds transport theorem Eqn.(2.36)

$$\frac{D}{Dt}\int_V \left(\frac{1}{2}\rho v^2\right)\, dV = \int_V \rho \boldsymbol{a}_{\mathcal{B}}\cdot\boldsymbol{v}\, dV, \tag{2.43}$$

and the external forces item on right hand side can be written as,

$$\begin{aligned}\int_{\partial V}\boldsymbol{t}\cdot\boldsymbol{v}dS + \int_V \rho\boldsymbol{b}_{\mathcal{B}}\cdot\boldsymbol{v}dV &= \int_V \boldsymbol{\nabla}\cdot[\sigma]\cdot\boldsymbol{v} + \boldsymbol{\sigma}:\boldsymbol{d}\, dV + \int_V \rho\boldsymbol{b}_{\mathcal{B}}\cdot\boldsymbol{v}\, dV \\ &= \int_V \underbrace{(\boldsymbol{\nabla}\cdot[\sigma]+\rho\boldsymbol{b}_{\mathcal{B}})}_{=\rho\boldsymbol{a}_{\mathcal{B}}\text{ based on Eqn.(2.37)}}\cdot\boldsymbol{v}\, dV + \int_V \boldsymbol{\sigma}:\boldsymbol{d}\, dV.\end{aligned} \tag{2.44}$$

Substituting Eqn.(2.43) and Eqn.(2.44) and combining the balance of linear momentum Eqn.(2.37), the local form of principle of conservation of energy can be expressed as,

$$\rho\dot{u} = \boldsymbol{\sigma}:\boldsymbol{d} - \boldsymbol{\nabla}\cdot(\boldsymbol{q}) + \rho r. \tag{2.45}$$

$(\boldsymbol{\sigma}:\boldsymbol{d})$[6] represents the stress power per unit deformed volume, then the local form of conservation of energy indicates that the rate of change of internal energy equals the stress power per unit deformed volume minus the divergence of the heat flux, plus heat production within the body.

Second Principle of Thermodynamics

The second principle of thermodynamics is also known as the entropy inequality, states that the entropy of an isolated system can never decrease in any process. It can only increase or stay the same.

[6]The operator ":" is the contraction operation between two tensors, which $\boldsymbol{\sigma}:\boldsymbol{d} = \sigma_{ij}\boldsymbol{d}_{ij}$.

The inequality can be written as,

$$\frac{D}{Dt}\left(\int_V \rho s dV\right) + \int_{\partial V} \frac{\boldsymbol{q}}{T} \cdot \boldsymbol{n} dS - \int_V \frac{\rho r}{T} dV \geq 0, \tag{2.46}$$

we then obtain Clausius-Duhem inequality in local form,

$$\rho \dot{s} + \boldsymbol{\nabla} \cdot (\frac{\boldsymbol{q}}{T}) - \frac{\rho r}{T} \geq 0. \tag{2.47}$$

It can also be written as,

$$\rho \dot{s} + \frac{1}{T} \boldsymbol{\nabla} \cdot \boldsymbol{q} - \frac{1}{T^2} \boldsymbol{q} \boldsymbol{\nabla} \cdot T - \frac{\rho r}{T} \geq 0, \tag{2.48}$$

based on experimental observations that heat only flows spontaneously from a hotter material point to a colder one, we can assume that the term $-\frac{1}{T^2} \boldsymbol{q} \boldsymbol{\nabla} \cdot T$ is always greater than or equal to zero [55] (P. 125), the strong form of the second law then reduces to

$$\rho \dot{s} + \frac{1}{T} \boldsymbol{\nabla} \cdot \boldsymbol{q} - \frac{\rho r}{T} \geq 0. \tag{2.49}$$

3 Constitutive Model of Shape Memory Alloys

In this chapter, the constitutive model will be presented in details.

3.1 Kinematics

Motivated by the the idea of additive decomposition, the total strain is divided into two parts, elastic strain and a recoverable inelastic strain due to the detwinning of martensite, which reads as,

$$\boldsymbol{h} = \boldsymbol{h}^e + \boldsymbol{h}^{in}. \tag{3.1}$$

Assuming that there are three proccesses contributing to the accumulation of inelastic strain, which are:

$\boldsymbol{h}^t$, the transformation strain due to the phase transformation from austenite to martensite;

$\boldsymbol{h}^o$, the orientation strain caused by the detwining of self-accommodated martensite to oriented martensite;

$\boldsymbol{h}^r$, the reorientation strain describes the reorientation of the martensite direction according to the non-proportional loading.

Then the total strain can be written as

$$\boldsymbol{h} = \boldsymbol{h}^e + \boldsymbol{h}^{in} = \boldsymbol{h}^e + \boldsymbol{h}^t + \boldsymbol{h}^o + \boldsymbol{h}^r. \tag{3.2}$$

The rate of inelastic strain is taken to be,

$$\mathring{\boldsymbol{h}}^{in} = \mathring{\boldsymbol{h}}^t + \mathring{\boldsymbol{h}}^o + \mathring{\boldsymbol{h}}^r = \sqrt{\frac{3}{2}} \left(\xi \dot{H} \boldsymbol{N}^o + \dot{\xi} H \boldsymbol{N}^t + \xi H \mathring{\boldsymbol{N}} \right), \tag{3.3}$$

where,

ξ is the martensite volume fraction, and is restricted by $0 \leq \xi \leq 1$;

H is the effective inelastic strain restricted by $0 \leq H \leq H_{max}$;

$\boldsymbol{N}^t$ and $\boldsymbol{N}^t$ are the flow direction of phase transformation and orientation respectively;

$\boldsymbol{N}$ is the "effective" direction of oriented martensite, which is defined as, $\boldsymbol{N} = \boldsymbol{h}^{in}/\|\boldsymbol{h}^{in}\|$, and $\dot{\boldsymbol{N}}$ suggests the reorientation direction under sufficient non-proportional loading.

And the multiplier $\sqrt{\frac{3}{2}}$ is induced to the measure of effective inelastic strain, *i.e.*,$H_{max} = \sqrt{\frac{2}{3}\boldsymbol{h}^{in}_{max} : \boldsymbol{h}^{in}_{max}}$.

3.2 Thermodynamic Potential

To derivative the constitutive relation, a free energy potential and complementary independent state variables should be chosen. By following the framework of Lagoudas and coworkers [55, 58, 118], Gibbs free energy is adopted. The external state variables $\boldsymbol{\tau}$ and absolute temperature T are regarded as the independent state variables. And a set of internal state variables is defined as $\mathbf{Y} = \{\xi, \boldsymbol{h}^{in}, \kappa^t, \kappa^o, \kappa^r\}$, where ξ is martensite volume fraction, $\boldsymbol{h}^{in}$ is the effective inelastic strain and $\kappa^t, \kappa^o, \kappa^r$ are the isotrpic hardening variables associated with phase transformation, orientation and reorientation process respectively.

The specific Gibbs Free energy is defined by the rule of mixture as,

$$G(\boldsymbol{\tau}, T, \xi, \boldsymbol{h}^{in}, \kappa^o, \kappa^t, \kappa^r) = (1-\xi)G^A(\boldsymbol{\tau}, T) + \xi G^M(\boldsymbol{\tau}, T) + G^m(\boldsymbol{\tau}, \boldsymbol{h}^{in}, \kappa^o, \kappa^t, \kappa^r), \tag{3.4}$$

where

$$G^\beta(\boldsymbol{\tau}, T) = -\frac{1}{2\rho_0}\boldsymbol{\tau} : \boldsymbol{\mathcal{S}}^\beta : \boldsymbol{\tau} - \frac{1}{\rho_0}\boldsymbol{\tau} : \boldsymbol{\alpha}^\beta(T - T_0) + c^\beta(\xi)\left[T - T_0 - T\ln\left(\frac{T}{T_0}\right)\right] - s_0^\beta T + u_0^\beta, \tag{3.5}$$

for $\beta = A, M$, stand for the thermoelastic contributions to the Gibbs free energy from the regions of austenite and martensite (the superscripts A and M denote

austenite and martensite phases, respectively), and

$$G^m(\boldsymbol{\tau}, \boldsymbol{h}^{in}, \kappa^o, \kappa^t, \kappa^r) = -\frac{1}{\rho_0}\boldsymbol{\tau} : \boldsymbol{h}^{in} \underbrace{+\frac{1}{\rho_0}g^o(\kappa^o) + \frac{1}{\rho_0}g^t(\kappa^t) + \frac{1}{\rho_0}g^r(\kappa^r)}_{\text{hardening term}} \tag{3.6}$$

stands for the contribution due to the interaction between the phases.

The parameter ρ_0 denotes the density which is assumed to be the same regardless of phase. The model parameters $\boldsymbol{\mathcal{S}}^\beta$, $\boldsymbol{\alpha}^\beta$, c^β, s_0^β, and u_0^β denote the compliance tensor, thermal expansion,specific heat capacity, specific entropy, and specific internal energy at the reference state, respectively, which are assumed to be different for each phase.

$$\boldsymbol{\mathcal{S}}(\xi) = \boldsymbol{\mathcal{S}}^A + \xi\left(\boldsymbol{\mathcal{S}}^A - \boldsymbol{\mathcal{S}}^M\right) = \boldsymbol{\mathcal{S}}^A + \xi\Delta\boldsymbol{\mathcal{S}}, \tag{3.7}$$

$$\boldsymbol{\alpha}(\xi) = \boldsymbol{\alpha}^A + \xi\left(\boldsymbol{\alpha}^M - \boldsymbol{\alpha}^A\right) = \boldsymbol{\alpha}^A + \xi\Delta\boldsymbol{\alpha}, \tag{3.8}$$

$$c(\xi) = c^A + \xi\left(c^M - c^A\right) = c^A + \xi\Delta c, \tag{3.9}$$

$$s_0(\xi) = s_0^A + \xi\left(s_0^M - s_0^A\right) = s_0^A + \xi\Delta s_0, \tag{3.10}$$

$$u_0(\xi) = u_0^A + \xi\left(u_0^M - u_0^A\right) = u_0^A + \xi\Delta u_0, \tag{3.11}$$

where, g^t, g^o, and g^r which describe the free energy blocked in the microstructure due to phase transformation, orientation and reorientation, respectively, depend only on the respective isotropic hardening variables κ^o, κ^t, and κ^r.

Considering the evolution of anisotropic thermal expansion, we make a special assumption to TE tensor,

$$\boldsymbol{\alpha}^A = \alpha^A\boldsymbol{\delta}, \tag{3.12}$$

where α^A is a scalar and $\boldsymbol{\delta}$ is the unit tensor with components $\delta_{ij} = 1$ if $i = j$ and $\delta_{ij} = 0$ if $i \neq j$.

The thermal expansion of martensite is assumed to evolve with (re)orientation as a function of the oriented martensite volume fraction, $\xi^o = \xi H/H^{\max}$, and orientation direction, $\boldsymbol{N} = \boldsymbol{h}^{in}/\|\boldsymbol{h}^{in}\|$, as follows

$$\boldsymbol{\alpha}^M = \alpha_0^M \boldsymbol{\delta} + \alpha^M \xi^o \boldsymbol{N}, \tag{3.13}$$

where α_0^M and α^M are scalar parameters to be determined from experiments. $\alpha_0^M \boldsymbol{\delta}$ corresponds to the isotropic CTE of self-accommodated martensite. Thus, in view of Eqn. (3.8), (3.12) and (3.13), the effective value of the TE tensor reads as

$$\boldsymbol{\alpha} = \boldsymbol{\alpha}^A + \xi \Delta \boldsymbol{\alpha} = \boldsymbol{\alpha}^A + \xi \left(\alpha_0^M - \alpha^A\right) \boldsymbol{\delta} + \xi^2 \alpha^M \frac{H}{H^{max}} \boldsymbol{N}. \tag{3.14}$$

3.3 Constitutive Relations

In this section, we derive the necessary constitutive relations following a standard thermodynamic procedure, which is referred as Coleman-Noll procedure. The phase transformation in SMAs is a dissipative process that involves an entropy increase. The material response of dissipative process is constrained by the second law of thermodynamics, which adopting the strong form of the Clausius-Duhem inequality (Eqn. (3.15)),

$$\rho_0 \dot{s} + \frac{1}{T} \boldsymbol{\nabla} \cdot \boldsymbol{q} - \frac{\rho_0 r}{T} \geq 0, \tag{3.15}$$

where $\boldsymbol{q}$,r and s denote the heat flux heat sources and entropy respectively. Combined with the first law of thermodynamics Eqn. (3.16) and the relation between specific internal energy u and Gibbs free energy G Eqn. (3.17):

$$\rho_0 \dot{u} = \boldsymbol{\tau} : \boldsymbol{d} - \boldsymbol{\nabla} \cdot \boldsymbol{q} + \rho_0 r, \tag{3.16}$$

$$G = u - \frac{1}{\rho_0}\boldsymbol{\tau} : \boldsymbol{h} - sT. \tag{3.17}$$

We are able to get

$$D = \rho_0 \dot{s} T + \boldsymbol{\nabla} \cdot \boldsymbol{q} - \rho_0 r = -\rho_0 \dot{G} - \rho_0 s \dot{T} - \boldsymbol{h} : \mathring{\boldsymbol{\tau}} \geq 0. \tag{3.18}$$

Taking into account Eqn. (3.4), the rate of change of the Gibbs free energy is given by,

$$\dot{G} = \frac{\partial G}{\partial \boldsymbol{\tau}} : \mathring{\boldsymbol{\tau}} + \frac{\partial G}{\partial T}\dot{T} + \frac{\partial G}{\partial \boldsymbol{h}^{in}} : \mathring{\boldsymbol{h}}^{in} + \frac{\partial G}{\partial \xi} : \dot{\xi} + \frac{\partial G}{\partial \kappa^t} : \dot{\kappa^t} + \frac{\partial G}{\partial \kappa^o} : \dot{\kappa^o} + \frac{\partial G}{\partial \kappa^r} : \dot{\kappa^r}. \tag{3.19}$$

Substituting Eqn. (3.19) into Eqn. (3.18), we obtain,

$$\underbrace{-\left(\rho_0 \frac{\partial G}{\partial \boldsymbol{\tau}} + \boldsymbol{h}\right) : \mathring{\boldsymbol{\tau}} - \rho_0 \left(\frac{\partial G}{\partial T} + s\right)\dot{T}}_{\text{Thermoelastic Region}}$$
$$\underbrace{-\rho_0 \frac{\partial G}{\partial \boldsymbol{h}^{in}} : \mathring{\boldsymbol{h}}^{in} - \rho_0 \frac{\partial G}{\partial \xi} : \dot{\xi} - \rho_0 \frac{\partial G}{\partial \kappa^t} : \dot{\kappa^t} - \rho_0 \frac{\partial G}{\partial \kappa^o} : \dot{\kappa^o} - \rho_0 \frac{\partial G}{\partial \kappa^r} : \dot{\kappa^r}}_{\text{Dissipation}} \geq 0. \tag{3.20}$$

The first two items represent the thermoelastic region and the rest items contribute to dissipation due to the rate of internal state variables $\mathring{\mathbf{Y}}$.

In the thermoelastic region, $\mathring{\mathbf{Y}}$ is zero. To make sure the above inequality valid for all $\mathring{\boldsymbol{\tau}}$ and $\dot{T}$, the following constitutive relations should be satisfied:

$$\boldsymbol{h} = -\rho_0 \partial_{\boldsymbol{\tau}} G = \boldsymbol{\mathcal{S}} : \boldsymbol{\tau} + \boldsymbol{\alpha}(T - T_0) + \boldsymbol{h}^{in}, \tag{3.21}$$

$$s = -\partial_T G = \frac{1}{\rho_0}\boldsymbol{\tau} : \boldsymbol{\alpha} + c \ln\left(\frac{T}{T_0}\right) + s_0. \tag{3.22}$$

These constitutive relations are also assumed to be valid everywhere at the boundary of the thermoelastic region. A detailed discussion on this assumption is presented in [86].

3.4 Evolution of Internal State Variables

The dissipation inequality is defined as Eqn. (3.23)

$$D = -\boldsymbol{\Gamma} : \mathring{\mathbf{Y}} = p\dot{\xi} + \boldsymbol{\pi} : \left(\mathring{\boldsymbol{h}}^t + \mathring{\boldsymbol{h}}^o + \mathring{\boldsymbol{h}}^r\right) + \mu^t\dot{\kappa}^t + \mu^o\dot{\kappa}^o + \mu^r\dot{\kappa}^r \geq 0, \tag{3.23}$$

where, $\boldsymbol{\Gamma}$ is defined as a set of generalized thermodynamic forces which conjugate to the rate of internal state variable set $\dot{\mathbf{Y}}$, as Eqn. (3.24)

$$\boldsymbol{\Gamma} = -\rho_0 \frac{\partial G}{\partial \mathbf{Y}}. \tag{3.24}$$

The components of the thermodynamic forces set are listed as follows:

$$\begin{aligned} p = -\rho_0 \partial_{\tilde{\xi}} G = \frac{1}{2}\boldsymbol{\tau} : \Delta\boldsymbol{\mathcal{S}} : \boldsymbol{\tau} + \boldsymbol{\tau} : \partial_{\tilde{\xi}}\boldsymbol{\alpha}(T - T_0) \\ - \rho\Delta c \left[T - T_0 - T\ln\left(\frac{T}{T_0}\right)\right] + \rho_0 \Delta s_0 T - \Delta u_0, \end{aligned} \tag{3.25}$$

$$\boldsymbol{\pi} = -\rho_0 \partial_{\boldsymbol{h}^{in}} G = \left[\boldsymbol{I} + \alpha^M \xi^2 \frac{H}{H^{max}} \frac{\boldsymbol{I} - \boldsymbol{N}\otimes\boldsymbol{N}}{\|\boldsymbol{h}^{in}\|}(T - T_0)\right] : \boldsymbol{\tau}, \tag{3.26}$$

$$\mu^a = -\rho_0 \partial_{\kappa^a} G, \tag{3.27}$$

and a stands for any of the superscripts t, o or r.

Motivated by the assumption that the inelastic strain is induced due to three procedures, phase transformation, orientation and reorientation, we consider a strong form of dissipation, which is definitely satisfied Eq. (3.23),

$$\begin{cases} D^t = p\dot{\xi} + \boldsymbol{\pi} : \mathring{\boldsymbol{h}}^t + \mu^t\dot{\kappa}^t > 0; & \dot{\xi} \neq 0, \\ D^o = \boldsymbol{\pi} : \mathring{\boldsymbol{h}}^o + \mu^o\dot{\kappa}^o > 0; & \mathring{\boldsymbol{h}}^o \neq \mathbf{0}, \\ D^r = \boldsymbol{\pi} : \mathring{\boldsymbol{h}}^r + \mu^r\dot{\kappa}^r > 0; & \mathring{\boldsymbol{h}}^r \neq \mathbf{0}. \end{cases} \tag{3.28}$$

These relations are the rate of work done by phase transformation, orientation

and reorientation due to changes in micro-structure induced by $\dot{\mathbf{Y}}$ in generalized thermodynamic force space and they are obeyed at all times so that the dissipation inequality is concurrently satisfied.

The above inequalities, Eqn. (3.28), are used to determine the kinetic relations for the internal state variables, *i.e.*, the flow rules, as follows.

Denoting as $\mathbf{Y}$ any set of internal state variables $\{\boldsymbol{h}^o, \kappa^o\}$, $\{\boldsymbol{h}^t, \xi, \kappa^t\}$, or $\{\boldsymbol{h}^r, \kappa^r\}$, the dissipation inequalities in Eqn. (3.28) can be written in the generic form

$$D(\boldsymbol{\Gamma}; \mathring{\mathbf{Y}}) = \boldsymbol{\Gamma} : \mathring{\mathbf{Y}} \geq 0, \tag{3.29}$$

where $\boldsymbol{\Gamma} = -\rho_0 \partial_{\mathbf{Y}} G$ is the set of generalized thermodynamic forces conjugate to $\mathring{\mathbf{Y}}$.

In view of the above definitions, *generalized normality* allows one to define evolution equations of the internal variables

$$\mathring{\mathbf{Y}} = \dot{\lambda} \partial_{\boldsymbol{\Gamma}} Q, \tag{3.30}$$

subjecting to the Kuhn–Tucker conditions:

$$\dot{\lambda} \geq 0; \;\; \Phi \leq 0; \;\; \dot{\lambda}\Phi = 0, \tag{3.31}$$

where $Q(\boldsymbol{\Gamma}; T)$ is a given smooth (at least once differentiable), scalar function called *potential*, which may not be coincident with the respective *yield function*, $\Phi(\boldsymbol{\Gamma}; T)$. In view of Eqn.(3.30), a yield function that satisfies the dissipation inequality Eqn. (3.29) is

$$\Phi = \boldsymbol{\Gamma} : \partial_{\boldsymbol{\Gamma}} Q - Y \leq 0, \tag{3.32}$$

where $Y = -Q(\mathbf{0}; T) > 0$. If Q is convex, then

$$D = \dot{\lambda}\boldsymbol{\Gamma} : \partial_{\boldsymbol{\Gamma}} Q \geq \dot{\lambda}\left(Q + Y\right), \tag{3.33}$$

and, thus, yield functions such that

$$\Phi \leq Q \;\text{ and }\; \Phi(\mathbf{0}; T) = Q(\mathbf{0}; T), \tag{3.34}$$

satisfy the dissipation inequality. The special case $\Phi = Q$ in the above inequality corresponds to the so-called standard dissipative materials obeying *associative* flow rules for which D is the global maximum for the space of the admissible generalized thermodynamic forces conjugate to $\mathring{\mathbf{Y}}$.

Therefore, the next important step for establishing the desired kinetic relations for the internal state variables is the selection of the appropriate form of the potential functions, Q, and yield functions, Φ.

3.4.1 Flow rules associated with orientation

As discussion in Section 3.3, assuming the internal state variables $\mathbf{Y}^o = \{\boldsymbol{h}^o, \kappa^o\}$ are associated with orientation process. The orientation potential function is proposed based on the thermodynamic forces $\boldsymbol{\Gamma} = \{\boldsymbol{\pi}, \mu^o\}$ conjugated to $\mathbf{Y}^o$ and temperature T, which is written as Eqn. (3.35),

$$Q^o\left(\boldsymbol{\pi}, \mu^o, T; \xi\right) = \xi\left(\overline{\pi}R - \mu^o - Y^o + c^o T\right) \quad (\xi \neq 0), \tag{3.35}$$

where Y^o and c^o are positive scalars, such that $Y^o - c^o T > 0$ for $\xi \neq 0$, *i.e.*, $0 < c^o < Y^o / A_f$, the orientation related internal state variables read as

$$\begin{cases} \mathring{\boldsymbol{h}}^o = \dot{\lambda}^o \partial_{\boldsymbol{\pi}} Q^o, \\ \dot{\kappa}^o = \dot{\lambda}^o \partial_{\mu^o} Q^o, \end{cases} \tag{3.36}$$

or equivalently as

$$\begin{cases} \mathring{\boldsymbol{h}}^o = \dot{\lambda}^o \xi \partial_{\boldsymbol{\pi}} \left(\overline{\pi} R \right), \\ \dot{\kappa}^o = -\dot{\lambda}^o \xi, \end{cases} \tag{3.37}$$

where $\overline{\pi} = \sqrt{\frac{3}{2} \boldsymbol{\pi}' : \boldsymbol{\pi}'}$ stands for the deviatoric part of thermodynamic force ($\boldsymbol{\pi}' = \boldsymbol{\pi} - \frac{1}{3} \mathrm{tr}(\boldsymbol{\pi}) \boldsymbol{\delta}$ and $\boldsymbol{\delta}$ is the unit tensor with components $\delta_{ij} = 1$ if $i = j$ and $\delta_{ij} = 0$ if $i \neq j$), and

$$R(\boldsymbol{\pi}) = \left[1 + \gamma \frac{\det \left(\boldsymbol{\pi}' \right)}{\overline{\pi}^3} \right]^{\frac{1}{n}}, \tag{3.38}$$

accounts for tension-compression asymmetry, and the convexity condition is dissussed in section A.1.

Note that with respect to the notation introduced in Eqn. (3.3), $\dot{\lambda}^o = \dot{H}$, *i.e.*, the rate of the orientation multiplier defines the rate of increase of the effective inelastic strain.

3.4.2 Flow rules associated with forward phase transformation

The potential function associated with forward phase transformation reads as

$$Q_f^t(\boldsymbol{\pi}, p, \mu^t, T; H) = H \overline{\pi} R + p - \mu_f^t - Y^t, \tag{3.39}$$

where Y^t is a strictly positive scalar.

The transformation related internal state variables are then given by

$$\begin{cases} \mathring{\boldsymbol{h}}^t = \dot{\lambda}_f^t \partial_{\boldsymbol{\pi}} Q_f^t = \dot{\lambda}_f^t H \partial_{\boldsymbol{\pi}} \left(\overline{\pi} R \right), \\ \dot{\xi} = \dot{\lambda}_f^t \partial_p Q_f^t = \dot{\lambda}_f^t, \\ \dot{\kappa}^t = \dot{\lambda}_f^t \partial_{\mu_f^t} Q_f^t = -\dot{\lambda}_f^t, \end{cases} \tag{3.40}$$

and equivalently, in view of Eqn. (3.39), by

$$\begin{cases} \mathring{\boldsymbol{h}}^t = \dot{\xi} H \partial_{\boldsymbol{\pi}} \left(\overline{\pi} R \right), \\ \dot{\kappa}^t = -\dot{\xi}. \end{cases} \tag{3.41}$$

3.4.3 Flow rules associated with reorientation

The following choice of the reorientation potential function

$$Q^r \left(\boldsymbol{\pi}, \mu^r, \boldsymbol{h}^{in}, T \right) = \xi H \left(\overline{\pi}_M - Y^r + c^r T \right), \tag{3.42}$$

where Y^r and c^r are positive scalars, such that $Y^r - c^r T > 0$ for $\xi \neq 0$, $\overline{\pi}_M$ is given by replacing $\boldsymbol{\pi}$ with $\boldsymbol{M} : \boldsymbol{\pi}$ in the definition of the von misses stress, $\boldsymbol{M} = \boldsymbol{I} - \boldsymbol{N} \otimes \boldsymbol{N}$, and $\boldsymbol{I}$ is the unit fourth-order tensor with components $\boldsymbol{I}_{ijkl} = \delta_{ik}\delta_{jl}$, yields

$$\mathring{\boldsymbol{h}}^r = \dot{\lambda}^r \partial_{\boldsymbol{\pi}} Q^r = \dot{\lambda}^r \xi H \partial_{\boldsymbol{\pi}} \overline{\pi}_M. \tag{3.43}$$

Note that $\boldsymbol{M} : \boldsymbol{\pi}$ is the projection of $\boldsymbol{\pi}$ on the hyperlpane with normal $\boldsymbol{N}$ and represents the orientation difference between the applied stress tensor and the inelastic strain.

With respect to the notation introduced in Eqn.(3.3), $\dot{\boldsymbol{N}} = \dot{\lambda}^r \sqrt{\frac{2}{3}} \partial_{\boldsymbol{\pi}} \overline{\pi}_M$ and, thus, the constraint $\|\boldsymbol{N}\| = 1$ is satisfied, as in fact $\boldsymbol{N} : \dot{\boldsymbol{N}} = 0$.

3.4.4 Flow rules associated with reverse phase transformation

Assuming

$$Q_r^t\left(\boldsymbol{\pi}, P, \mu_r^t, T; \boldsymbol{h}^{in}\right) = -\frac{\boldsymbol{\pi} : \boldsymbol{h}^{in}}{\xi} - p + \mu_r^t - Y^t, \tag{3.44}$$

the flow rules for reverse phase transformation are given by

$$\begin{cases} \mathring{\boldsymbol{h}}^{in} = \dot{\lambda}_r^t \partial_{\boldsymbol{\pi}} Q_r^t = -\dot{\lambda}_r^t \dfrac{\boldsymbol{h}^{in}}{\xi}, \\ \dot{\xi} = \dot{\lambda}_r^t \partial_p Q_r^t = -\dot{\lambda}_r^t, \\ \dot{\kappa}^t = \dot{\lambda}_r^t \partial_{\mu_r^t} Q_r^t = \dot{\lambda}_r^t, \end{cases} \tag{3.45}$$

or equivalently by

$$\begin{cases} \mathring{\boldsymbol{h}}^{in} = \dot{\xi} \dfrac{\boldsymbol{h}^{in}}{\xi}, \\ \dot{\kappa}^t = -\dot{\xi}. \end{cases} \tag{3.46}$$

Thus, the direction of the inelastic strain recovery is governed by the average direction of the martensite variants and the magnitude of strain recovery rate is proportional to the rate of martensite volume fraction, thus, there can be no remanent inelastic strain upon reversal to the austenite state.

3.4.5 Hardening functions associated with phase transformation and (re)orientation

Thus far the hardening functions, μ_f^t, μ_r^t and μ^o, associated with phase transformation and orientation have not been specified. The branched hardening function that changes with transformation direction, introduced in [58], is adopted for

phase transformation

$$\mu^t(\kappa^t) = \mu^t(\xi) := \begin{cases} \mu_f^t(\xi) = \frac{1}{2}a_1^t \left[1 + \xi^{n_1^t} - (1-\xi)^{n_2^t}\right] + a_3^t; \;\; \dot{\xi} > 0, \\ \mu_r^t(\xi) = \frac{1}{2}a_2^t \left[1 + \xi^{n_3^t} - (1-\xi)^{n_4^t}\right] - a_3^t; \;\; \dot{\xi} < 0, \end{cases} \tag{3.47}$$

which allows for the experimentally observed asymmetry in forward and reverse phase transformation and for smooth transitions between the elastic and phase transformation regimes. The coefficients $a_1^t - a_3^t$ are material parameters while the exponents $n_1^t - n_4^t$, which take values in the interval $(0, 1]$, do not have an associated material property but are directly chosen to best fit the four corners of the transformation hysteresis plots.

A similar power-law form for the hardening function associated with orientation is introduced

$$\mu^o(\kappa^o; \xi) = \mu^o(\xi H; \xi) := \frac{1}{2}a_1^o \left\{1 + \left(\frac{H}{H^{\max}}\right)^{n_1^o} - \left[1 - \left(\frac{H}{H^{\max}}\right)\right]^{n_2^o}\right\}, \tag{3.48}$$

where a_1^o are material parameters and $0 < n_1^o \leq 1$, $0 < n_2^o \leq 1$ are chosen to best fit the transitions between the elastic and orientation regimes.

Note that based on the model's performance on simulating the experimental deformation response under non-proportional loading paths, no hardening during reorientation is assumed, *i.e.*, $\mu^o(\kappa^o) = 0$.

3.4.6 Minor loops

In order to simulate minor loops, two scalar-valued functions $\mathcal{Q}_r$ and $\mathcal{Q}_f$ are introduced in the potential functions associated with forward and reverse phase

transformation, respectively,

$$\begin{cases} Q_f^t = H\overline{\pi}R + p - \mu_f^t + \mathcal{Q}_r - Y^t \leq 0, \\ Q_r^t = -\dfrac{\boldsymbol{\pi} : \boldsymbol{h}^{in}}{\xi} - p + \mu_r^t + \mathcal{Q}_f - Y^t \leq 0, \end{cases} \tag{3.49}$$

such that

$$\mathcal{Q}_f = \begin{cases} \left(\mu_f^t - \mu_r^t + 2Y^t\right)(1-\xi); & \Phi_f^t = 0, \\ \mathcal{Q}_f; & \text{else}, \end{cases} \tag{3.50}$$

only evolves when reverse phase transformation is active, and

$$\mathcal{Q}_r = \begin{cases} -\left(\mu_f^t - \mu_r^t + 2Y^t\right)\xi; & \Phi_r^t = 0, \\ \mathcal{Q}_r; & \text{else}, \end{cases} \tag{3.51}$$

only evolves when forward phase transformation is active, *i.e.*, during forward phase transformation, $\mathcal{Q}_r$ is constant, and, similarly, during reverse phase transformation, $\mathcal{Q}_f$ is constant. Thus, the evolution equations and the dissipation inequalities related to phase transformation remain unaltered while the transformation yield functions now read as

$$\begin{cases} \Phi_f^t = H\overline{\pi}R + p - \mu_f^t + \mathcal{Q}_r - Y^t \leq 0, \\ \Phi_r^t = -\dfrac{\boldsymbol{\pi} : \boldsymbol{h}^{in}}{\xi} - p + \mu_r^t + \mathcal{Q}_f - Y^t \leq 0. \end{cases} \tag{3.52}$$

These functions, *i.e.*, $\mathcal{Q}_r$ and $\mathcal{Q}_f$, essentially shift the transformation yield surfaces from being identical at the initiation of either forward or reverse phase transformation to the expressions introduced in (3.57) once phase transformation (forward or reverse) is completed.

Note that this description of minor loops is based only on the major loop data with no additional requirements.

3.4.7 Yield functions

The dissipation inequalities Eqn. (3.28) now read, in view of Eqns. (3.37), (3.41), (3.46) and (3.43), as

$$\begin{cases} D^o = \dot{\lambda}^o \xi \left[\boldsymbol{\pi} : \partial_{\boldsymbol{\tau}} \left(\overline{\pi} R \right) - \mu^o \right] \geq 0; \quad \mathring{\boldsymbol{h}}^o \neq \mathbf{0}, & (3.53) \\ \begin{cases} D_f^t = \dot{\xi} \left[\boldsymbol{\pi} : H \partial_{\boldsymbol{\pi}} \left(\overline{\pi} R \right) + p - \mu_f^t \right] \geq 0; \quad \dot{\xi} > 0, \\ D_r^t = -\dot{\xi} \left(\dfrac{\boldsymbol{\pi} : \boldsymbol{h}^{in}}{\xi} + p + \mu_r^t \right) \geq 0; \quad \dot{\xi} < 0, \end{cases} & (3.54) \\ D^r = \dot{\lambda}^r \xi H \left(\boldsymbol{\pi} : \partial_{\boldsymbol{\pi}} \overline{\pi}_M \right) \geq 0; \quad \mathring{\boldsymbol{h}}^r \neq \mathbf{0}. & (3.55) \end{cases}$$

The convexity of the potential functions Q^o, Q_f^t, Q_r^t, and Q^r are ensured by Eqn. (A.4) in section A.1. Accordingly, the following yield functions are postulated that satisfy the above dissipation inequalities (see section 3.3),

$$\begin{cases} \Phi^o \left(\boldsymbol{\pi}, \mu^o; T \right) = Q^o \left(\boldsymbol{\pi}, \mu^o, T \right) = \overline{\pi} R - \mu^o + c^o T - Y^o \leq 0, & (3.56) \\ \begin{cases} \Phi_f^t(\boldsymbol{\pi}, p, \mu_f^t, T; H) = (1 - C) H \overline{\pi} R + p - \mu_f^t - Y^t \leq 0, \\ \Phi_r^t(\boldsymbol{\pi}, p, \mu_r^t, T; \boldsymbol{h}^{in}) = -(1 + C) \dfrac{\boldsymbol{\pi} : \boldsymbol{h}^{in}}{\xi} - p + \mu_r^t - Y^t \leq 0, \end{cases} & (3.57) \\ \Phi^r \left(\boldsymbol{\pi}, \mu^r, T \right) = Q^r \left(\boldsymbol{\pi}, \mu^r T \right) = \overline{\pi}_M + c^r T - Y^r \leq 0. & (3.58) \end{cases}$$

Note that the introduced parameter $0 < C < 1$ in the expressions of Φ_f^t and Φ_r^t, which results in $\Phi_\alpha^t < Q_\alpha^t$ and $\Phi_\alpha^t(\mathbf{0}) = Q_\alpha^t(\mathbf{0})$ (Section 3.4), where α stands for f or r, accounts for the dissimilar slopes of the transformation boundaries on the SMA phase diagram (Clapeyron slopes), *i.e.*, on the temperature and load dependence of the width of the hysteresis loop evident for example in isobaric cooling–heating experiments at different bias load levels.

The constitutive model is summarized in Table 1.

Table 1: Model Summary

State Variables	Thermodynamic force $\boldsymbol{\pi}$, temperature T, total strain train $\boldsymbol{h}$, inelastic strain $\boldsymbol{h}^{in}$, transformation strain $\boldsymbol{h}^{t}$, orientation strain $\boldsymbol{h}^{o}$, reorientation strain $\boldsymbol{h}^{r}$, volume fraction of martensite ξ, hardening variables $\left\{\kappa^{t}, \kappa^{o}, \kappa^{r}\right\}$
Gibbs Free Energy	$G(\boldsymbol{\pi}, T, \xi, \boldsymbol{h}^{in}, \kappa^{o}, \kappa^{t}, \kappa^{r}) = (1-\xi)G^{A}(\boldsymbol{\pi}, T) + \xi G^{M}(\boldsymbol{\pi}, T) + G^{m}(\boldsymbol{\pi}, \boldsymbol{h}^{in}, \kappa^{o}, \kappa^{t}, \kappa^{r})$ $G^{\beta}(\boldsymbol{\pi}, T) = -\frac{1}{2\rho_0}\boldsymbol{\pi} : \boldsymbol{S}^{\beta} : \boldsymbol{\pi} - \frac{1}{\rho_0}\boldsymbol{\pi} : \boldsymbol{\alpha}^{\beta}(T - T_0) + c^{\beta}(\xi)\left[T - T_0 - T\ln\left(\frac{T}{T_0}\right)\right] - s_0^{\beta}T + u_0^{\beta}$ $G^{m}(\boldsymbol{\pi}, \boldsymbol{h}^{in}, \kappa^{o}, \kappa^{t}, \kappa^{r}) = -\frac{1}{\rho_0}\boldsymbol{\pi} : \boldsymbol{h}^{in} + \frac{1}{\rho_0}g^{o}(\kappa^{o}) + \frac{1}{\rho_0}g^{t}(\kappa^{t}) + \frac{1}{\rho_0}g^{r}(\kappa^{r})$ (β stands for any of the superscripts A or M)
Thermal Expansion	$\boldsymbol{\alpha}^{A} = \alpha^{A}\boldsymbol{\delta}; \;\; \boldsymbol{\alpha}^{M} = \alpha_0^{M}\boldsymbol{\delta} + \alpha^{M}\xi^{o}\boldsymbol{N}$ $\boldsymbol{\alpha} = \boldsymbol{\alpha}^{A} + \xi\Delta\boldsymbol{\alpha} = \boldsymbol{\alpha}^{A} + \xi\left(\alpha_0^{M} - \alpha^{A}\right)\boldsymbol{\delta} + \xi^{2}\alpha^{M}\frac{H}{H^{max}}\boldsymbol{N}$
Thermodynamic Forces	$p = -\rho_0\partial_{\xi}G = \frac{1}{2}\boldsymbol{\tau} : \Delta\boldsymbol{S} : \boldsymbol{\tau} - \rho_0\Delta c\left[T - T_0 - T\ln\left(\frac{T}{T_0}\right)\right] + \rho_0\Delta s_0 T - \Delta u_0,$ $\mu^{t}(\kappa^{t}) = \mu^{t}(\xi) = -\rho_0\partial_{\kappa^{t}}G := \begin{cases} \mu_f^{t} = \frac{1}{2}a_1^{t}\left[1 + \xi^{n_1^{t}} - (1-\xi)^{n_2^{t}}\right] + a_3^{t}; \;\; \dot{\xi} > 0, \\ \mu_r^{t} = \frac{1}{2}a_2^{t}\left[1 + \xi^{n_3^{t}} - (1-\xi)^{n_4^{t}}\right] - a_3^{t}; \;\; \dot{\xi} < 0, \end{cases}$ $\mu^{o}(\kappa^{o}; \xi) = \mu^{o}(\xi H; \xi) = -\rho_0\partial_{\kappa^{o}}G := \frac{1}{2}a_1^{o}\left\{1 + \left(\frac{H}{H^{\max}}\right)^{n_1^{o}} - \left[1 - \left(\frac{H}{H^{\max}}\right)\right]^{n_2^{o}}\right\}$ $\mu^{r}(\kappa^{r}) = -\rho_0\partial_{\kappa^{r}}G = 0$
Yield Surfaces	
· Orientation	$\Phi^{o}\left(\boldsymbol{\pi}, \mu^{o}, T\right) = Q^{o}\left(\boldsymbol{\pi}, \mu^{o}; T\right) = \overline{\pi}R - \mu^{o} + c^{o}T - Y^{o} \leq 0$
· Phase Transformation	$\begin{cases} \Phi_f^{t}(\boldsymbol{\pi}, p, \mu_f^{t}, T; H) = (1-C)H\overline{\pi}R + p - \mu_f^{t} + \mathcal{Q}_r - Y^{t} \leq 0 \\ \Phi_r^{t}(\boldsymbol{\pi}, p, \mu^{t}, T; \boldsymbol{h}^{in}) = -(1+C)\dfrac{\boldsymbol{\pi} : \boldsymbol{h}^{in}}{\xi} - p + \mu_r^{t} + \mathcal{Q}_f - Y^{t} \leq 0 \end{cases}$
· Reorientation	$\Phi^{r}\left(\boldsymbol{\pi}, \mu^{r}, T\right) = Q^{r}\left(\boldsymbol{\tau}, \mu^{r}, T\right) = \overline{\tau}_{M} + c^{r}T - Y^{r} \leq 0$
Evolution Equations	
· Orientation	$\mathring{\boldsymbol{h}}^{o} = \xi\dot{H}\partial_{\boldsymbol{\pi}}Q^{o}$
· Phase Transformation	Forward: $\mathring{\boldsymbol{h}}^{t} = \dot{\xi}H\partial_{\boldsymbol{\pi}}\left(\overline{\pi}R\right)$; Reverse: $\mathring{\boldsymbol{h}}^{in} = \dot{\xi}\dfrac{\boldsymbol{h}^{in}}{\xi}$
· Reorientation	$\mathring{\boldsymbol{h}}^{r} = \dot{\lambda}^{r}\xi H\partial_{\boldsymbol{\pi}}\overline{\pi}_{M}$

3.5 Thermomechanical Coupling: Latent Heat Effect

Taking into account Eqn.(3.18), (3.23) can be written as

$$D = D^o + D^t + D^r = \rho_0 \dot{s} T + \boldsymbol{\nabla} \cdot \boldsymbol{q} - \rho_0 r. \tag{3.59}$$

In view of the constitutive relationship Eqn. (3.22), the entropy rate is deduced as

$$\dot{s} = c\frac{\dot{T}}{T} + \frac{1}{\rho_0}\mathring{\boldsymbol{\tau}} : \boldsymbol{\alpha} + \left[\frac{1}{\rho_0}\boldsymbol{\tau} : \partial_{\xi}\boldsymbol{\alpha} + \Delta c \ln\left(\frac{T}{T_0}\right) + \Delta s_0\right]\dot{\xi} + \frac{1}{\rho_0}\partial_H \boldsymbol{\alpha}\dot{H} + \frac{1}{\rho_0}\partial_{\boldsymbol{h}^{in}}\boldsymbol{\alpha} : \mathring{\boldsymbol{h}}^{in}, \tag{3.60}$$

where,

$$\begin{aligned}
\partial_{\xi}\boldsymbol{\alpha} &= \left(\alpha_0^M - \alpha^A\right)\boldsymbol{\delta} + 2\xi\alpha^M\frac{H}{H^{max}}\boldsymbol{N}, \\
\partial_H\boldsymbol{\alpha} &= \xi^2\alpha^M\frac{1}{H^{max}}\boldsymbol{N}, \\
\partial_{\boldsymbol{h}^{in}}\boldsymbol{\alpha} &= \xi^2\alpha^M\frac{H}{H^{max}}\frac{\boldsymbol{I} - \boldsymbol{N}\otimes\boldsymbol{N}}{\|\boldsymbol{h}^{in}\|}.
\end{aligned} \tag{3.61}$$

And, thus, Eqn. (3.59) reads as

$$\begin{aligned}
&\rho_0 c\dot{T} + \mathring{\boldsymbol{\tau}} : \boldsymbol{\alpha} T - \underbrace{\dot{H}\xi\left[\boldsymbol{\pi} : \partial_{\boldsymbol{\pi}}\left(\overline{\pi}R\right) - \mu^o - \boldsymbol{\pi} : \partial_H\boldsymbol{\alpha}T\right]}_{\text{heat released during orientation}} \\
&- \begin{cases}
\underbrace{\dot{\xi}\left\{\boldsymbol{\pi} : H\partial_{\boldsymbol{\pi}}\left(\overline{\pi}R\right) + p - \mu_f^t - \left[\boldsymbol{\pi} : \partial_{\xi}\boldsymbol{\alpha} + \rho_0\Delta c\ln\left(\frac{T}{T_0}\right) + \rho_0\Delta s_0\right]T\right\}}_{\text{heat released during forward phase transformation}} \\
\text{or} \\
\underbrace{\dot{\xi}\left\{-\frac{\boldsymbol{\pi} : \boldsymbol{h}^{in}}{\xi} - p + \mu_r^t - \left[\boldsymbol{\pi} : \partial_{\xi}\boldsymbol{\alpha} + \rho_0\Delta c\ln\left(\frac{T}{T_0}\right) + \rho_0\Delta s_0\right]T\right\}}_{\text{heat absorbed during reverse phase transformation}}
\end{cases} \\
&\qquad - \underbrace{\dot{\lambda}^r\xi H\left\{\boldsymbol{\pi} - \partial_{\boldsymbol{h}^{in}}\boldsymbol{\alpha}T\right\} : \partial_{\pi}\overline{\pi}_M}_{\text{heat released during reorientation}} = -\boldsymbol{\nabla}\cdot\boldsymbol{q} + \rho_0 r,
\end{aligned} \tag{3.62}$$

which is the 3D form of the fully thermomechanically-coupled energy balance equation for SMAs. The first term of the left-hand side of the above equation is the energy change associated with the specific heat capacity. The second term demonstrates the energy change according to the stress rate. The third, fourth, and fifth terms on the left-hand side express temperature variations due to orientation, phase transformation, and reorientation, respectively. The first and second terms of the right-hand side are related to the heat transfer processes by the heat flux, $\boldsymbol{q}$, and heat sources, $\rho_0 r$.

The heat flux $\boldsymbol{q}$ is assumed to be governed by Fourier's law

$$\boldsymbol{q} = -\boldsymbol{k}(\xi)\boldsymbol{\nabla} T, \tag{3.63}$$

where $\boldsymbol{k}(\xi) = (1-\xi)\boldsymbol{k}^A + \xi \boldsymbol{k}^M$ stands for the thermal conductivity, which is approximated from the conductivities of austenite, $\boldsymbol{k}^A$, and martensite, $\boldsymbol{k}^M$, by the rule of mixtures.

The latent heat produced during forward transformation in the stress-free state can be obtained by integrating the term

$$\dot{\xi}\left\{\boldsymbol{\pi} : H\partial_{\boldsymbol{\pi}}\left(\overline{\pi}R\right) + p - \mu_f^t - \left[\boldsymbol{\pi} : \partial_{\xi}\boldsymbol{\alpha} + \rho_0 \Delta c \ln\left(\frac{T}{T_0}\right) + \rho_0 \Delta s_0\right] T\right\}, \tag{3.64}$$

of the heat equation Eqn. (3.62) that corresponds to the rate of excess heat during transformation [56]. The latent heat produced during forward transformation is equal to the latent heat absorbed during reverse phase transformation as a result of conservation of energy.

3.6 Model Calibration

The calibration of the proposed model, based on the experimentally determined deformation response of the material under *uniaxial loading*, is described

in this section. In the case of finite strains, experimental evaluation of the onset of phase transformation and post-transformation stress-strain behavior generally should be based on either the 1st Piola-Kirchhoff stresses or of Cauchy stresses, *i.e.*, either on the undeformed or deformed configuration, respectively. However, since elastic and transformation-induced volumetric deformations in SMAs are small, the specific choice of the stress measure is not significant and may include the Kirchhoff stress, $\boldsymbol{\tau} = J\boldsymbol{\sigma} \sim \boldsymbol{\sigma}$. Thus, the calibration procedure of the finite- and infinitesimal-strain models differ only on experimental evaluation of the logarithmic strain in the former instead of the engineering strain in the latter.

Assuming experimental evaluation of the engineering strain, the constitutive equations are first reduced to 1D. The relation between the current stress and strain, Eqn. (3.21), reduces to

$$\sigma = E(\xi)\left[\varepsilon - \alpha(\xi)\,(T - T_0) - \varepsilon^t - \varepsilon^o - \varepsilon^r\right], \tag{3.65}$$

where

$$E(\xi) = \left[\frac{1}{E_A} + \xi\left(\frac{1}{E_M} - \frac{1}{E_A}\right)\right]^{-1}. \tag{3.66}$$

The evolution equations, Eqn. (3.37), (3.41), and (3.46), are reduced to

$$\begin{cases} \dot{\varepsilon}^o = \dot{H}\xi \mathrm{sgn}(\sigma)\left[1 + \mathrm{sgn}(\sigma)\dfrac{2}{27}\gamma\right]^{\frac{1}{n}}, \\ \dot{\varepsilon}^t = \begin{cases} \dot{\xi} H \mathrm{sgn}(\sigma)\left[1 + \mathrm{sgn}(\sigma)\dfrac{2}{27}\gamma\right]^{\frac{1}{n}}; \;\; \dot{\xi} > 0, \\ \dot{\xi} H \mathrm{sgn}(\sigma)\left[1 + \mathrm{sgn}(\sigma)\dfrac{2}{27}\gamma\right]^{\frac{1}{n}}; \;\; \dot{\xi} < 0, \end{cases} \end{cases} \tag{3.67}$$

and the yield surfaces, Eqn. (3.56), (3.57), and (3.58), neglecting the effects of Δc

(common engineering assumptions), are reduced to

$$\begin{cases} \Phi^o(\sigma,T,\xi) = \mathrm{sgn}(\sigma)\sigma\left[1+\mathrm{sgn}(\sigma)\dfrac{2}{27}\gamma\right]^{\frac{1}{n}} - \mu^o - Y^o \le 0, \\ \begin{cases} \Phi^t_f(\sigma,T,\xi) = \mathrm{sgn}(\sigma)(1-C)\sigma H\left[1+\mathrm{sgn}(\sigma)\dfrac{2}{27}\gamma\right]^{\frac{1}{n}} + p - \mu^t_f - Y^t_0 \le 0; \;\; \dot{\xi} > 0, \\ \Phi^t_r(\sigma,T,\xi;\varepsilon^{in}) = -\mathrm{sgn}(\sigma)(1+C)\sigma\dfrac{\varepsilon^{in}}{\xi} - p + \mu^t_r - Y^t_0 \le 0; \;\; \dot{\xi} < 0. \end{cases} \end{cases} \tag{3.68}$$

3.6.1 Calibration of the elastic constants, E^A, E^M, ν_A, ν_M.

E^A, E^M can be calculated directly from isothermal stress–strain curves where loads are applied at temperatures outside the transformation regions. It is generally assumed that $\nu_A = \nu_M = 0.3$.

3.6.2 Calibration of TE tensor

The calibration of the TE constants of austenite, α^A, and self-accommodated martensite, α^M_0, can be calibrated from temperature variations under zero bias load above the austenite-finish and below the martensite-finish temperatures, respectively. The parameter α^M can be calibrated from experiments like the ones performed in [73], and reviewed in Section 3.2, by fitting the expression (3.13) to the experimentally determined values of the TE tensor. In Eqn. (3.13), the H-value can be measured in such experiments from the irrecoverable strain upon unloading and the orientation tensor $\boldsymbol{N}$ is given by

$$\boldsymbol{N} = \sqrt{\frac{2}{3}}\begin{bmatrix} 1 & 0 & 0 \\ 0 & -1/2 & 0 \\ 0 & 0 & -1/2 \end{bmatrix}.$$

3.6.3 Calibration of the transformation related parameters

Assuming thermally-induced transformation occurring under load-free conditions, the following independent equations are obtained:

1. Forward transformation ($\dot{\xi} > 0$) at zero stress begins at the martensitic start temperature M_s,

$$\Phi_f^t(0, M_s, 0) = 0.$$

2. Forward transformation ($\dot{\xi} > 0$) at zero stress ends at the martensitic finish temperature M_f,

$$\Phi_f^t(0, M_f, 1) = 0.$$

3. Reverse transformation ($\dot{\xi} < 0$) at zero stress begins at the austenitic start temperature A_s,

$$\Phi_r^t(0, A_s, 1) = 0.$$

4. Reverse transformation ($\dot{\xi} < 0$) at zero stress ends at austenitic finish temperature A_f,

$$\Phi_r^t(0, A_f, 0) = 0.$$

5. For a full transformation loop, the material should return to its initial state, which requires the Gibbs free energy to return to its initial value. This requirement, given the form of Gibbs free energy adopted Eqn. (3.4), yields

$$\int_0^1 \mu_f^t d\xi + \int_1^0 \mu_r^t d\xi = 0.$$

The above five conditions yield the following expressions for the model parameters:

$$
\begin{aligned}
&a_1^t = \rho\Delta s_0 \left(M_f - M_s\right), \;\; a_2^t = \rho\Delta s_0 \left(A_s - A_f\right), \\
&a_3^t = -\frac{a_1^t}{4}\left(1 + \frac{1}{n_1^t + 1} - \frac{1}{n_2^t + 1}\right) + \frac{a_2^t}{4}\left(1 + \frac{1}{n_3^t + 1} - \frac{1}{n_4^t + 1}\right), \\
&\rho\Delta u_0 = \frac{\rho\Delta s_0}{2}\left(M_s + A_f\right), \;\; Y^t = \rho\Delta s_0 \left(M_s - A_f\right) - a_3^t.
\end{aligned}
\tag{3.69}
$$

Calibration of $\rho\Delta s_0$ and C is performed by considering the slope of the transformation surface in a uniaxial stress–temperature space assuming constant ξ. Then, the Kuhn–Tucker conditions imply

$$
d\Phi^t = \partial_\sigma \Phi^t d\sigma + \partial_T \Phi^t dT = 0. \tag{3.70}
$$

Assuming $\sigma > \sigma_f$ (Figure 1.5), the above yields

$$
\begin{cases}
\left.\dfrac{d\sigma}{dT}\right|_{\Phi_f^t = 0} = \dfrac{-\rho\Delta s_0}{\left(1 - C\right) H^{\max}\left(1 + \frac{2}{27}\gamma\right)^{\frac{1}{n}} + \sigma\left(\frac{1}{E_M} - \frac{1}{E_A}\right)}, \\
\left.\dfrac{d\sigma}{dT}\right|_{\Phi_r^t = 0} = \dfrac{-\rho\Delta s_0}{\left(1 + C\right) H^{\max}\left(1 + \frac{2}{27}\gamma\right)^{\frac{1}{n}} + \sigma\left(\frac{1}{E_M} - \frac{1}{E_A}\right)}.
\end{cases}
\tag{3.71}
$$

Note that $\left.\dfrac{d\sigma}{dT}\right|_{\Phi_f^t}$ and $\left.\dfrac{d\sigma}{dT}\right|_{\Phi_r^t = 0}$ are nearly constants since $\sigma\left(\frac{1}{E_M} - \frac{1}{E_A}\right)$ at load levels of interest are small values in comparison to $\left(1 \pm C\right) H^{\max}\left(1 + \frac{2}{27}\gamma\right)^{\frac{1}{n}}$. Thus, dropping $\sigma\left(\frac{1}{E_M} - \frac{1}{E_A}\right)$ and by denoting the forward and reverse transformation slopes, C^M and C^A, respectively, Eqn. (3.71) yields

$$
\begin{cases}
\rho\Delta s_0 = -H^{\max}\left(1 + \frac{2}{27}\gamma\right)^{\frac{1}{n}} \dfrac{2C^M C^A}{C^M + C^A}, \\
C = \dfrac{C^M - C^A}{C^M + C^A}.
\end{cases}
\tag{3.72}
$$

As already mentioned, the hardening coefficients $n_1^t - n_4^t$ are directly chosen to best fit the four corners of the transformation hysteresis plots.

Next, γ and H^{max} are calibrated from the experimentally determined values of maximum transformation strain. At completion of forward phase transformation, integration of Eqn. (3.41), gives

$$\begin{cases} {}_m\varepsilon_t^t = H^{\max}\left(1+\dfrac{2}{27}\gamma\right)^{\frac{1}{n}}; \ \text{tension}, \\ {}_m\varepsilon_c^t = -H^{\max}\left(1-\dfrac{2}{27}\gamma\right)^{\frac{1}{n}}; \ \text{compression}, \end{cases} \tag{3.73}$$

where ${}_m\varepsilon_t^t$, and ${}_m\varepsilon_c^t$ are the experimentally determined maximum transformation strains under tensile and compressive loading, respectively. The above system yields

$$\begin{cases} \gamma = \dfrac{27}{2}\dfrac{\varepsilon_*^n+1}{\varepsilon_*^n-1}, \\ H^{\max} = \dfrac{{}_m\varepsilon_t^t}{\left(1+\frac{2}{27}\gamma\right)^{\frac{1}{n}}}, \end{cases} \tag{3.74}$$

where $\varepsilon_* = \dfrac{{}_m\varepsilon_t^t}{{}_m\varepsilon_c^t}$, and n can take any value that ensures convexity of the yield functions Eqn. (A.3).

3.6.4 Calibration of the orientation related parameters

During orientation under tension, the orientation yield function, Eqn. (3.56), yields

$$\Phi^o = \sigma\left(1+\frac{2}{27}\gamma\right)^{\frac{1}{n}} - \mu^o - Y^o + c^o T = 0, \tag{3.75}$$

where μ^o is defined in Eqn. (3.48).

The above equation, (3.75), evaluated at $H = 0$ and $H = H^{\max}$, reads as

$$\begin{cases} \sigma_s^t \left(1 + \dfrac{2}{27}\gamma\right)^{\frac{1}{n}} - Y^o + c^o T = 0, \\ \sigma_f^t \left(1 + \dfrac{2}{27}\gamma\right)^{\frac{1}{n}} - a_1^o - Y^o + c^o T = 0, \end{cases} \tag{3.76}$$

where σ_s^t is the stress level required for initiation of orientation and σ_f^t for completion of orientation.

From the above, we obtain

$$\begin{cases} a_1^o = \left(\sigma_f^t - \sigma_s^t\right) \left(1 + \dfrac{2}{27}\gamma\right)^{\frac{1}{n}}, \\ Y^o = \sigma_s^t \left(1 + \dfrac{2}{27}\gamma\right)^{\frac{1}{n}} + c^o T. \end{cases} \tag{3.77}$$

Experimental determination of σ_s^t and σ_f^t at two temperatures, $T = T^*$ and $T = T^{**}$, yields

$$\begin{cases} c^o = -\dfrac{\sigma_s^t(T^*) - \sigma_s^t(T^{**})}{T^* - T^{**}} \left(1 + \dfrac{2}{27}\gamma\right)^{\frac{1}{n}}, \\ a_1^o = \left(\sigma_f^t(T^*) - \sigma_s^t(T^*)\right) \left(1 + \dfrac{2}{27}\gamma\right)^{\frac{1}{n}}, \\ Y^o = \dfrac{\sigma_s^t(T^{**})T^* - \sigma_s^t(T^*)T^{**}}{T^* - T^{**}} \left(1 + \dfrac{2}{27}\gamma\right)^{\frac{1}{n}}. \end{cases} \tag{3.78}$$

The hardening coefficients n_1^o and n_2^o are chosen to best fit the corners of the reorientation stress–strain plot.

3.6.5 Calibration of the reorientation related parameters

It is assumed that $Y^r = Y^o$ and $c^r = c^o$. All model parameters and associated material properties are listed in Table 2.

Table 2: Parameter Calibration and Associated Material Properties

Common SMA Material Parameter	Model Parameters	Calibration
E_A, E_M, ν_A, ν_M	$\mathcal{S}^A$, $\mathcal{S}^M$	Section 3.6.1
α^A, α^M	α_0^M	Eqn. (3.13)
M_s, M_f, A_s, A_s	$\rho\Delta u_0$, a_1, a_2, a_3, Y^t	Eqn. (3.69)
C^A C^M	$\rho\Delta s_0$,C	Eqn. (3.72)
${}_m\varepsilon_t^t$, ${}_m\varepsilon_c^t$	γ, H^{max}	Eqn. (3.74)
$\sigma_s^t(T^*)$, $\sigma_s^t(T^{**})$, $\sigma_f^t(T^*)$, $\sigma_f^t(T^{**})$	c^o, a_1^o, Y^o	Eqn. (3.78)
N/A	Y^r,c^r	Section 3.6.5

4 NUMERICAL IMPLEMENTATION

In the previous chapter, we discussed the derivation of a 3-d SMA thermomechanical constitutive model. In this chapters, we address on the numerical implementation of SMAs thermomechanical constitutive response based on the return mapping algorithm, which is appropriate for rate-dependent inelastic constitutive models. To trace the response of an SMA structural model subjected to a given loading history an *incremental–iterative procedure* is needed. The load is applied in a number of increments, and the structural response after each increment is computed from the equilibrium equations (and the energy balance equation). The equilibrium equation is nonlinear and an iterative loop inside the *global* (top-level) loop of load incrementation is needed to restore equilibrium. At every iteration during this loop, it is necessary to evaluate the stress corresponding to a change of the strain (and temperature) field. The stress evaluation, in the case of material models with internal state variables such as the proposed SMA model, requires another iteration loop, the so-called *stress return mapping algorithm*, nested in the global equilibrium(/energy balance) iteration loop. Below the *closest point projection* return mapping algorithm is described, which outputs an increment of stress given an increment of strain and temperature. Furthermore, the algorithmic tangent moduli tensors are given, which are needed for preserving the rate of convergence of the global equilibrium iteration.

4.1 Closed-Form Algorithm for Updating the Rotation Tensor

To update the logarithmic rate, $\boldsymbol{\Omega}^{L}_{n+1}$, given the increments of displacement, $\Delta \boldsymbol{u}_n$, and temperature, ΔT_n, the algorithm proceeds as follows. The deformation gradient

$$\boldsymbol{F}_{n+1} = \left(\boldsymbol{\delta} + \nabla_n[\boldsymbol{\Delta u}_n]\right) \boldsymbol{F}_n; \;\; \text{where} \;\; \nabla_n[\boldsymbol{u}] = \frac{\partial \boldsymbol{u}(\boldsymbol{x}_n)}{\partial \boldsymbol{x}_n},$$

the stretching

$$\boldsymbol{d}_{n+1} = \frac{1}{2}\left[\frac{\boldsymbol{F}_{n+1}-\boldsymbol{F}_n}{\Delta t}\boldsymbol{F}_{n+1}^{-1} + \left(\frac{\boldsymbol{F}_{n+1}-\boldsymbol{F}_n}{\Delta t}\boldsymbol{F}_{n+1}^{-1}\right)^T\right],$$

the spin,

$$\boldsymbol{w}_{n+1} = \frac{1}{2}\left[\frac{\boldsymbol{F}_{n+1}-\boldsymbol{F}_n}{\Delta t}\boldsymbol{F}_{n+1}^{-1} - \left(\frac{\boldsymbol{F}_{n+1}-\boldsymbol{F}_n}{\Delta t}\boldsymbol{F}_{n+1}^{-1}\right)^T\right],$$

the left Cauchy-Green stretch $\boldsymbol{b}_{n+1}$

$$\boldsymbol{b}_{n+1} = \boldsymbol{F}_{n+1}\boldsymbol{F}_{n+1}^T$$

are updated sequentially, and in turn the logarithmic rate

$$\boldsymbol{\Omega}_{n+1}^L \Delta t = \left[\boldsymbol{w}_{n+1} + \sum_{\alpha\neq\beta}^{m}\left(\frac{1+(\lambda_{n+1}^{\alpha}/\lambda_{n+1}^{\beta})}{1-(\lambda_{n+1}^{\alpha}/\lambda_{n+1}^{\beta})} + \frac{2}{\ln(\lambda_{n+1}^{\alpha}/\lambda_{n+1}^{\beta})}\right)\boldsymbol{b}_{n+1}^{\alpha}\boldsymbol{d}_{n+1}\boldsymbol{b}_{n+1}^{\beta}\right]\Delta t,$$

where the λ_{n+1}^{α} and $\boldsymbol{b}_{n+1}^{\alpha}$ are the eigenvectors and their corresponding eigenprojections of $\boldsymbol{b}$.

According to the logarithmic rate $\boldsymbol{\Omega}^L$, logarithmic rotation can be defined as following (see 4.1),

$$\begin{cases} \dot{\boldsymbol{R}}^L(t) & = \boldsymbol{\Omega}^L\boldsymbol{R}^L(t), \\ \boldsymbol{R}^L|_{t=0} & = \boldsymbol{\delta}. \end{cases} \tag{4.1}$$

The existence theorem for ordinary differential equations tells us that this problem has exactly one solution $\boldsymbol{R}^L(t)$, $-\infty < t < +\infty$, which we write in the form [78, 36]

$$\boldsymbol{R}^L(t) = \exp(\boldsymbol{\Omega}^L t), \tag{4.2}$$

and in the incremental form,

$$\boldsymbol{R}_{n+1}^L = \exp\left[\boldsymbol{\Omega}_{n+1}^L \Delta t\right]\boldsymbol{R}_n^L. \tag{4.3}$$

Nakshatrala, K. B. [78] discussed the numerical implementation of the exponential map. The one of the Nineteen dubious methods [72] evaluates the exponential map by truncating the infinite series given by,

$$\exp(\boldsymbol{\Omega}^L) = \boldsymbol{I} + \sum_{n=1}^{n=\infty} \frac{1}{n!} (\boldsymbol{\Omega}^L)^n. \tag{4.4}$$

However this method is prone to round-off errors and not recommended. A highly recommended algorithm for evaluating the exponential of 3×3 skew-symmetric matrices is based on Rodrigues formula [110, 54].

Let the set of all 3×3 real-proper-orthogonal matrices be defined as $SO(3)$,

$$SO(3) = \{R^L : R^L \in \mathbb{R}^{3\times 3}, \boldsymbol{R}^L \boldsymbol{R}^{L^T} = \boldsymbol{I}, \mathrm{Det}(\boldsymbol{R}^L) = 1\}. \tag{4.5}$$

The set of all 3×3 skew-symmetric matrices is denoted by $SK(3)$,

$$SK(3) = \{\boldsymbol{\Omega}^L : \boldsymbol{\Omega}^L \in \mathbb{R}^{3\times 3}, \boldsymbol{\Omega}^{L^T} = -\boldsymbol{\Omega}^L\}. \tag{4.6}$$

Any skew-symmetric matrix $\boldsymbol{\Omega}^L \in SK(3)$ can also be represented in axial vector $\hat{\boldsymbol{\omega}}$, which are,

$$\hat{\boldsymbol{\omega}} = \begin{bmatrix} \omega_1 \\ \omega_2 \\ \omega_3 \end{bmatrix}, \quad \boldsymbol{\Omega}^L = \begin{bmatrix} 0 & -\omega_3 & \omega_2 \\ \omega_3 & 0 & -\omega_1 \\ -\omega_2 & \omega_1 & 0 \end{bmatrix}. \tag{4.7}$$

Rodrigues formula gives a closed-form expression as solution of Eqn. (4.1),

$$\exp[\boldsymbol{\Omega}^L t] = \boldsymbol{I} + \frac{\sin(\|\hat{\boldsymbol{\omega}}\| t)}{\|\hat{\boldsymbol{\omega}}\|} \boldsymbol{\Omega}^L + \frac{1 - \cos(\|\hat{\boldsymbol{\omega}}\| t)}{\|\hat{\boldsymbol{\omega}}\|^2} \boldsymbol{\Omega}^{L^2}. \tag{4.8}$$

4.2 Closest Point Projection Return Mapping Algorithm

Transformation consistency is enforced by determining the intersection of the stress evolution curve with the boundary of the transformation surface (return mapping). In this section, the numerical implementation of SMA thermomechanical constitutive response is presented using return mapping algorithms appropriate for rate-independent inelastic constitutive models.

4.2.1 Implicit Euler method

The goal is to evaluate the stress increment given the increments of total strain and temperature by solving the elastic-transformation-orientation-reorientation problem defined by the total strain relation Eqn. (3.2), the flow rules Eqn. (3.37), (3.41), (3.43), and Eqn.(3.46), and the yield functions (3.56). First, a thermoelastic prediction assumes that the inelastic strain increment is null. If the predicted thermoelastic state violates the yield criteria an iterative loop of corrections restores the consistency conditions.

For the system of algebraic and ordinary differential equations (ODEs), this algorithm integrates the transformation evolution equation for the transformation correction using the backward Euler method (λ= 1 in (4.9)) resulting in a nonlinear algebraic set of equations that are solved using the Newton iteration method. The numerical discretization with the initial conditions given in Eqn. (4.10) is performed on the SMA model as the transformation strain are discretized using the generalized trapezoidal rule,

$$\boldsymbol{h}^{in}_{n+1} = \boldsymbol{h}^{in}_{n} + (\kappa_{n+1} - \kappa_n)\left[(1-\lambda)\boldsymbol{\Lambda}_n + \lambda\boldsymbol{\Lambda}_{n+1}\right]. \tag{4.9}$$

4.2.2 Thermoelastic prediction

The evolution of stress state toward the transformation surface ($\Phi = 0$) starts at the trial thermoelastic state. To begin, a thermoelastic predictor problem is solved that is described by assuming that the increments of the internal state variables $\{\Delta\xi_{n+1}, \Delta H^{cur}_{n+1}, \Delta\lambda^{r}_{n+1}\}$[7] are zero, then the trial thermoelastic state written as,

$$\begin{cases} \boldsymbol{h}_{n+1} = \boldsymbol{h}_n + \Delta\boldsymbol{h}_{n+1} = \dfrac{1}{2}\ln(\boldsymbol{b}_{n+1}), \\ T_{n+1} = T_n + \Delta T_{n+1}, \\ \xi^{(0)}_{n+1} = \xi_n, \\ H^{cur\,(0)}_{n+1} = H^{cur}_n, \\ \boldsymbol{\alpha}^{(0)}_{n+1} = \boldsymbol{\alpha}_n, \\ \boldsymbol{h}^{in\,(0)}_{n+1} = \boldsymbol{h}^{in}_n \\ \boldsymbol{\tau}^{(0)}_{n+1} = \boldsymbol{\mathcal{S}}^{-1}_n : \left[\boldsymbol{h}_{n+1} - \boldsymbol{h}^{in\,(0)}_{n+1} - \boldsymbol{\alpha}^{(0)}_{n+1}(T_{n+1} - T_0)\right], \end{cases} \tag{4.10}$$

where $\Delta\boldsymbol{h}_{n+1}$ and ΔT_{n+1} [8] are the specified strain and temperature increments and the subscript $(\cdot)_n$ denotes the converged values from the previous global iteration, the yield criteria

$$\begin{cases} \Phi^{o\,(0)}_{n+1} = \Phi^o\left(\boldsymbol{\tau}^{(0)}_{n+1}, H^{cur\,(0)}_{n+1}, T_{n+1}; \xi^{(0)}_{n+1}\right) \leq 0, \\ \Phi^{t\,(0)}_{n+1} = \Phi^t\left(\boldsymbol{\tau}^{(0)}_{n+1}, p^{(0)}_{n+1}, \xi^{(0)}_{n+1}, T_{n+1}; H^{cur\,(0)}_{n+1}, \boldsymbol{h}^{in\,(0)}_{n+1}\right) \leq 0, \\ \Phi^{r\,(0)}_{n+1} = \Phi^r\left(\boldsymbol{\tau}^{(0)}_{n+1}, \boldsymbol{h}^{in\,(0)}_{n+1}, T_{n+1}\right) \leq 0, \end{cases} \tag{4.11}$$

[7] The internal state variable set is defined as $[\boldsymbol{h}^{in}, \xi, \kappa^t, \kappa^o, \kappa^r]$ at beginning, and it reduced to the current set $\{\xi, H^{cur}, \lambda^r\}$ according to Eqn. (3.36)(3.41)(3.46)

[8] ΔT_{n+1} and $\Delta\boldsymbol{h}_{n+1}$ is given by the global iteration, and they are not implemented in yield correction

are examined, where

$$\Phi_{n+1}^{t\,(0)} = \begin{cases} \Phi_f^t \left(\boldsymbol{\tau}_{n+1}^{(0)}, p_{n+1}^{(0)}, \xi_{n+1}^{(0)}, T_{n+1}; H_{n+1}^{cur\,(0)} \right); & \dot{\xi} > 0, \\ \Phi_r^t \left(\boldsymbol{\tau}_{n+1}^{(0)}, p_{n+1}^{(0)}, \xi_{n+1}^{(0)}, T_{n+1}; \boldsymbol{h}_{n+1}^{in\,(0)} \right); & \dot{\xi} < 0. \end{cases} \tag{4.12}$$

If all are less than zero, then the trial state is taken as the final state. Otherwise, a correction is used to restore consistency.

4.2.3 Yield correction on phase transformation

According to Eqn.(4.9), the algorithm integrates the transformation (forward/ reverse) evolution equation for the transformation correction using the implicit Euler method resulting in a nonlinear algebraic set of equations, including a constrained function (Kuhn-Tucker optimality conditions), residual strain (evolution law) and residual stress (constitutive equation),

$$\begin{cases} \begin{cases} \Phi_{f\,n+1}^{t\,(0)} = (1-C) H_{n+1}^{cur} (\overline{\tau} R)_{n+1} + p_{n+1}^{(0)} - \mu_f^t(\xi_{n+1}^{(0)}) + \mathcal{Q}_r - Y^t, \\ \Phi_{r\,n+1}^{t\,(0)} = -(1+C) \left(\dfrac{\boldsymbol{\tau} : \boldsymbol{h}^{in}}{\xi} \right)_{n+1}^{(0)} - p_{n+1}^{(0)} + \mu_r^t(\xi_{n+1}^{(0)}) + \mathcal{Q}_f - Y^t, \end{cases} \\ \boldsymbol{R}_{n+1}^{\boldsymbol{h}\,(0)} = \boldsymbol{h}_n^{in} - \boldsymbol{h}_{n+1}^{in\,(0)} + \begin{cases} (\xi_{n+1}^{(0)} - \xi_n) H_{n+1}^{cur} \partial_{\boldsymbol{\tau}} (R\overline{\tau})_{n+1}^{(0)}; & \dot{\xi} > 0, \\ (\xi_{n+1}^{(0)} - \xi_n) \dfrac{\boldsymbol{h}_{n+1}^{in\,(0)}}{\xi_{n+1}^{(0)}}; & \dot{\xi} < 0, \end{cases} \\ \boldsymbol{R}_{n+1}^{\boldsymbol{\tau}\,(0)} = \boldsymbol{\mathcal{S}}_{n+1}^{(0)} : \boldsymbol{\tau}_{n+1}^{(0)} + \boldsymbol{\alpha}_{n+1}^{(0)} (T_{n+1} - T_0) + \boldsymbol{h}_{n+1}^{in\,(0)} - \boldsymbol{h}_{n+1}, \end{cases} \tag{4.13}$$

where p is defined as in Eqn. (3.26).

In the nonlinear system, there are 13 unknowns [$\Delta\xi_{n+1}$ (1), $\Delta\boldsymbol{\tau}_{n+1}$ (6), $\Delta\boldsymbol{h}_{n+1}^{in}$ (6)] and 13 equations $\{\Phi^t$ (1), $\boldsymbol{R}^{\boldsymbol{h}}$ (6) and $\boldsymbol{R}^{\boldsymbol{\tau}}$ (6)$\}$. Newton-Raphson method is adopted to solve the nonlinear system.

By the method, the root of the nonlinear system is searched by following the

steepest descent path with respect to unknown state variables $[\Delta\xi_{n+1}, \Delta\boldsymbol{\tau}_{n+1}, \Delta\boldsymbol{h}^{in}_{n+1}]$. The nonlinear system is firstly linearized by differentiating with respect to the unknowns,[9]

$$\begin{cases} \begin{cases} \Phi_{f\ n+1}^{t\ (k)} + \partial_{\boldsymbol{\tau}}\Phi_{f\ n+1}^{t\ (k)} : \Delta\boldsymbol{\tau}_{n+1}^{(k)} + \partial_{\xi}\Phi_{f\ n+1}^{t\ (k)} : \Delta\xi_{n+1}^{(k)} & = 0, \\ \Phi_{r\ n+1}^{t\ (k)} + \partial_{\boldsymbol{\tau}}\Phi_{r\ n+1}^{t\ (k)} : \Delta\boldsymbol{\tau}_{n+1}^{(k)} + \partial_{\xi}\Phi_{r\ n+1}^{t\ (k)} : \Delta\xi_{n+1}^{(k)} + \partial_{\boldsymbol{h}^{in}}\Phi_{r\ n+1}^{t\ (k)} : \Delta\boldsymbol{h}_{n+1}^{in\ (k)} & = 0, \end{cases} \\ \boldsymbol{R}_{n+1}^{\boldsymbol{h}\ (k)} + \partial_{\boldsymbol{\tau}}\boldsymbol{R}_{n+1}^{\boldsymbol{h}\ (k)} : \Delta\boldsymbol{\tau}_{n+1}^{(k)} + \partial_{\xi}\boldsymbol{R}_{n+1}^{\boldsymbol{h}\ (k)}\Delta\xi_{n+1}^{(k)} + \partial_{\boldsymbol{h}^{in}}\boldsymbol{R}_{n+1}^{\boldsymbol{h}\ (k)} : \Delta\boldsymbol{h}_{n+1}^{in\ (k)} & = 0, \\ \boldsymbol{R}_{n+1}^{\boldsymbol{\tau}\ (k)} + \partial_{\boldsymbol{\tau}}\boldsymbol{R}_{n+1}^{\boldsymbol{\tau}\ (k)} : \Delta\boldsymbol{\tau}_{n+1}^{(k)} + \partial_{\xi}\boldsymbol{R}_{n+1}^{\boldsymbol{\tau}\ (k)}\Delta\xi_{n+1}^{(k)} + \partial_{\boldsymbol{h}^{in}}\boldsymbol{R}_{n+1}^{\boldsymbol{\tau}\ (k)} : \Delta\boldsymbol{h}_{n+1}^{in\ (k)} & = 0. \end{cases} \tag{4.14}$$

The above system can be written as a linear system,

$$\mathbb{J}_{n+1}^{(k)} \cdot \Delta\mathbb{X}_{n+1}^{(k)} = \mathbb{B}_{n+1}^{(k)},$$

[9] The subscript $_{n+1}$ indicates the (n+1) increment of the global iteration depending on the loading path. The superscript $^{(k)}$ is denoted as the kth iteration in local Newton-Raphson scheme, which is contributing to the yield correction process.

where,

$$\mathbb{J}^{(k)}_{n+1} = \begin{bmatrix} \begin{Bmatrix} [(1-C)H^{cur}\partial_{\boldsymbol{\tau}}(R\overline{\tau}) + \Delta\boldsymbol{\mathcal{S}} : \boldsymbol{\tau} + \partial_{\xi}\boldsymbol{\alpha}(T_{n+1} - T_0)]^{(k)}_{n+1} \\ \left[-(1+C)\dfrac{\boldsymbol{h}^{in}}{\xi} - \Delta\boldsymbol{\mathcal{S}} : \boldsymbol{\tau} - \partial_{\xi}\boldsymbol{\alpha}(T_{n+1} - T_0)\right]^{(k)}_{n+1} \end{Bmatrix} & \begin{Bmatrix} (\xi^{(k)}_{n+1} - \xi_n)[H^{cur}\partial^2_{\boldsymbol{\tau}^2}(R\overline{\tau})]^{(k)}_{n+1} \\ \mathbf{0} \end{Bmatrix} \\ \boldsymbol{\mathcal{S}}^{(k)}_{n+1} & \begin{bmatrix} \begin{Bmatrix} -\partial_{\xi}\mu^{t\,(k)}_{f\,n+1} \\ \left[\dfrac{\boldsymbol{\tau} : \boldsymbol{h}^{in}}{\xi^2} + \partial_{\xi}\mu^{t}_{r}\right]^{(k)}_{n+1} \end{Bmatrix} & \begin{Bmatrix} \mathbf{0} \\ -\left[\dfrac{\boldsymbol{\tau}}{\xi}\right]^{(k)}_{n+1} \end{Bmatrix} \\ \begin{Bmatrix} [H^{cur}\partial_{\boldsymbol{\tau}}(R\overline{\tau})]^{(k)}_{n+1} \\ \dfrac{\boldsymbol{h}^{in\,(k)}_{n+1}}{\xi^{(k)}_{n+1}} \end{Bmatrix} & \begin{Bmatrix} -\boldsymbol{I} \\ -\left(1 - \dfrac{(\xi^{(k)}_{n+1} - \xi_n)}{\xi^{(k)}_{n+1}}\right)\boldsymbol{I} \end{Bmatrix} \\ \Delta\boldsymbol{\mathcal{S}} : \boldsymbol{\tau}^{(k)}_{n+1} + \partial_{\xi}\boldsymbol{\alpha}^{(k)}_{n+1}(T_{n+1} - T_0) & \boldsymbol{I} + \partial_{\boldsymbol{h}^{in}}\boldsymbol{\alpha}^{(k)}_{n+1}(T_{n+1} - T_0) \end{bmatrix} \end{bmatrix};$$

$$\Delta\mathbb{X}^{(k)}_{n+1} = \begin{bmatrix} \Delta\boldsymbol{\tau}^{(k)}_{n+1} \\ \Delta\xi^{(k)}_{n+1} \\ \Delta\boldsymbol{h}^{in\,(k)}_{n+1} \end{bmatrix}; \qquad \mathbb{B}^{(k)}_{n+1} = \begin{bmatrix} \begin{Bmatrix} -\Phi^{t\,(k)}_{f\,n+1} \\ -\Phi^{t\,(k)}_{r\,n+1} \end{Bmatrix} \\ -\boldsymbol{R}^{\boldsymbol{h}\,(k)}_{n+1} \\ -\boldsymbol{R}^{\boldsymbol{\tau}\,(k)}_{n+1} \end{bmatrix}.$$

This procedure is repeated until $\{\Phi^t_{n+1}, \boldsymbol{R}^{\boldsymbol{h}}_{n+1}, \boldsymbol{R}^{\boldsymbol{\tau}}_{n+1}\}$ are converged to zero (a tolerance value).

Detailed expressions in the matrix $\mathbb{J}$ are listed below:

$$
\begin{aligned}
&\partial_{\boldsymbol{\tau}}\boldsymbol{\tau}' = \boldsymbol{I} - \frac{1}{3}\boldsymbol{\delta}\odot\boldsymbol{\delta};\ \ \partial_{\boldsymbol{\tau}}(\det\boldsymbol{\tau}) = (\det\boldsymbol{\tau})\ \boldsymbol{\tau}^{-T};\ \ \partial_{\boldsymbol{\tau}}(\boldsymbol{\tau}^{-1}) = -\boldsymbol{\tau}^{-1}\otimes\boldsymbol{\tau}^{-1},\\
&\partial_{\boldsymbol{\tau}}\left(\overline{\tau}R\right) = R\frac{3}{2}\frac{\boldsymbol{\tau}'}{\overline{\tau}} + \frac{1}{n}\gamma\overline{\tau}R^{(1-n)}\frac{\det(\boldsymbol{\tau}')}{\overline{\tau}^3}\boldsymbol{\chi},\\
&\boldsymbol{\chi} = (\boldsymbol{\tau}')^{-1} : \left(\boldsymbol{I} - \frac{1}{3}\boldsymbol{\delta}\odot\boldsymbol{\delta}\right) - \frac{9}{2}\frac{\boldsymbol{\tau}'}{\overline{\tau}^2},\\
&\partial^2_{\boldsymbol{\tau}^2}\left(\overline{\tau}R\right) = \frac{3\gamma}{2n}R^{(1-n)}\frac{\boldsymbol{\tau}'}{\overline{\tau}}\odot\frac{\det(\boldsymbol{\tau}')}{\overline{\tau}^3}\boldsymbol{\chi} + \frac{3}{2}R\frac{1}{\overline{\tau}}\left(\boldsymbol{I} - \frac{1}{3}\boldsymbol{\delta}\odot\boldsymbol{\delta} - \frac{3}{2}\frac{\boldsymbol{\tau}'}{\overline{\tau}}\odot\frac{\boldsymbol{\tau}'}{\overline{\tau}}\right)\\
&\qquad + \frac{3\gamma}{2n}R^{1-n}\frac{\det(\boldsymbol{\tau}')}{\overline{\tau}^3}\boldsymbol{\chi}\odot\frac{\boldsymbol{\tau}'}{\overline{\tau}} + \frac{1-n}{n^2}\gamma^2\overline{\tau}R^{(1-2n)}\frac{\det(\boldsymbol{\tau}')}{\overline{\tau}^3}\boldsymbol{\chi}\odot\frac{\det(\boldsymbol{\tau}')}{\overline{\tau}^3}\boldsymbol{\chi} + \frac{\gamma}{n}\overline{\tau}R^{(1-n)}\boldsymbol{\chi}\odot\frac{\det(\boldsymbol{\tau}')}{\overline{\tau}^3}\boldsymbol{\chi}\\
&\qquad + \frac{\gamma}{n}\overline{\tau}R^{(1-n)}\frac{\det(\boldsymbol{\tau}')}{\overline{\tau}^3}\left[-(\boldsymbol{\tau}')^{-1}\otimes(\boldsymbol{\tau}')^{-1} : \left(\boldsymbol{I} - \frac{1}{3}\boldsymbol{\delta}\odot\boldsymbol{\delta}\right) - \frac{9}{2}\frac{1}{\overline{\tau}^2}\left(\boldsymbol{I} - \frac{1}{3}\boldsymbol{\delta}\odot\boldsymbol{\delta} - 3\frac{\boldsymbol{\tau}'}{\overline{\tau}}\odot\frac{\boldsymbol{\tau}'}{\overline{\tau}}\right)\right],\\
&\partial_{\tilde{\xi}}\boldsymbol{\alpha} = \left(\alpha_0^M - \alpha^A\right)\boldsymbol{\delta} + 2\tilde{\xi}\alpha^M\frac{H}{H^{max}}\boldsymbol{N},\\
&\partial_{\boldsymbol{h}^{in}}\boldsymbol{\alpha} = \tilde{\xi}^2\alpha^M\frac{H}{H^{max}}\frac{\boldsymbol{I} - \boldsymbol{N}\odot\boldsymbol{N}}{\|\boldsymbol{h}^{in}\|},\\
&\partial_{\tilde{\xi}}\mu_f^t = \frac{1}{2}a_1^t\left[n_1^t\tilde{\xi}^{(n_1^t-1)} + n_2^t(1-\tilde{\xi})^{(n_2^t-1)}\right],\\
&\partial_{\tilde{\xi}}\mu_r^t = \frac{1}{2}a_2^t\left[n_3^t\tilde{\xi}^{(n_3^t-1)} + n_4^t(1-\tilde{\xi})^{(n_4^t-1)}\right],
\end{aligned}
\tag{4.15}
$$

where, $\boldsymbol{I}$ is denoted to the identify fourth order tensor and $\boldsymbol{\delta}$ is the kroneck delta, and the expressions are:

$$
\begin{aligned}
&\boldsymbol{I}_{ijkl} = \frac{1}{2}(\boldsymbol{\delta}_{ik}\boldsymbol{\delta}_{jl} + \boldsymbol{\delta}_{il}\boldsymbol{\delta}_{jk}),\\
&\boldsymbol{\delta}_{ij} = \begin{cases} 1, & \text{if } i = j,\\ 0, & \text{if } i \neq j. \end{cases}
\end{aligned}
\tag{4.16}
$$

The calculator symbol $\odot$ in Eqn.(4.15) means the product of two second order tensors and producing a fourth order tensor with components $(\boldsymbol{f}\odot\boldsymbol{g})_{ijkl} = \boldsymbol{f}_{ij}\boldsymbol{g}_{kl}$, and the symbol $\otimes$ defined as $(\boldsymbol{f}\otimes\boldsymbol{g})_{ijkl} = \boldsymbol{f}_{ik}\boldsymbol{g}_{jl}$.

4.2.4 Yield correction on orientation yield surface

When orientation yield surface active, the dicretitized nonlinear system is as follows,

$$\begin{cases} \Phi^{o\,(0)}_{n+1} = (R\overline{\tau})^{(0)}_{n+1} - \mu^o(H^{cur\,(0)}_{n+1}) + c^o T_{n+1} - Y^o, \\ \boldsymbol{R}^{\boldsymbol{h}\,(0)}_{n+1} = \boldsymbol{h}^{in}_{n} - \boldsymbol{h}^{in\,(0)}_{n+1} + \xi_{n+1}[H^{cur\,(0)}_{n+1} - H^{cur}_{n}]\partial_{\boldsymbol{\tau}}(R\overline{\tau})^{(0)}_{n+1}, \\ \boldsymbol{R}^{\boldsymbol{\tau}\,(0)}_{n+1} = \boldsymbol{\mathcal{S}}_{n+1} : \boldsymbol{\tau}^{(0)}_{n+1} + \boldsymbol{\alpha}^{(0)}_{n+1}(T_{n+1} - T_0) + \boldsymbol{h}^{in\,(0)}_{n+1} - \boldsymbol{h}_{n+1}. \end{cases} \tag{4.17}$$

Linearizing the nonlinear system based on the unknowns $[\Delta H^{cur\,(k)}_{n+1},\ \Delta\boldsymbol{\tau}^{(k)}_{n+1},\ \Delta\boldsymbol{h}^{in\,(k)}_{n+1}]$,

$$\begin{cases} \Phi^{o\,(k)}_{n+1} + \partial_{\boldsymbol{\tau}}\Phi^{o\,(k)}_{n+1} : \boldsymbol{\Delta\tau}^{(k)}_{n+1} + \partial_{H^{cur}}\Phi^{o\,(k)}_{n+1}\Delta H^{cur\,(k)}_{n+1} & = 0, \\ \boldsymbol{R}^{\boldsymbol{h}\,(k)}_{n+1} + \partial_{\boldsymbol{\tau}}\boldsymbol{R}^{\boldsymbol{h}\,(k)}_{n+1} : \Delta\boldsymbol{\tau}^{(k)}_{n+1} + \partial_{H^{cur}}\boldsymbol{R}^{\boldsymbol{h}\,(k)}_{n+1}\Delta H^{cur\,(k)}_{n+1} + \partial_{\boldsymbol{h}^{in}}\boldsymbol{R}^{\boldsymbol{h}\,(k)}_{n+1} : \Delta\boldsymbol{h}^{in\,(k)}_{n+1} & = 0, \\ \boldsymbol{R}^{\boldsymbol{\tau}\,(k)}_{n+1} + \partial_{\boldsymbol{\tau}}\boldsymbol{R}^{\boldsymbol{\tau}\,(k)}_{n+1} : \Delta\boldsymbol{\tau}^{(k)}_{n+1} + \partial_{H^{cur}}\boldsymbol{R}^{\boldsymbol{\tau}\,(k)}_{n+1}\Delta H^{cur\,(k)}_{n+1} + \partial_{\boldsymbol{h}^{in}}\boldsymbol{R}^{\boldsymbol{\tau}\,(k)}_{n+1} : \Delta\boldsymbol{h}^{in\,(k)}_{n+1} & = 0. \end{cases} \tag{4.18}$$

The above system can be written as a linear system,

$$\mathbb{J}^{(k)}_{n+1} \cdot \Delta\mathbb{X}^{(k)}_{n+1} = \mathbb{B}^{(k)}_{n+1},$$

where,

$$\mathbb{J}^{(k)}_{n+1} = \begin{bmatrix} \partial_{\boldsymbol{\tau}}(R\overline{\tau})^{(k)}_{n+1} & -\partial_{H^{cur}}\mu^{o\,(k)}_{n+1} & \boldsymbol{0} \\ (H^{cur\,(k)}_{n+1} - H^{cur}_{n})[\xi\partial^2_{\boldsymbol{\tau}^2}(R\overline{\tau})]^{(k)}_{n+1} & [\xi\partial_{\boldsymbol{\tau}}(R\overline{\tau})]^{(k)}_{n+1} & -\boldsymbol{I} \\ \boldsymbol{\mathcal{S}}^{(k)}_{n+1} & \partial_{H^{cur}}\boldsymbol{\alpha}^{(k)}_{n+1}(T_{n+1} - T_0) & \boldsymbol{I} + \partial_{\boldsymbol{h}^{in}}\boldsymbol{\alpha}^{(k)}_{n+1}(T_{n+1} - T_0) \end{bmatrix}.$$

4.2.5 Yield correction on reorientation yield surface

When reorientation yield surface active, the dicretitized nonlinear system is as follows,

$$\begin{cases} \Phi^{r\,(0)}_{n+1} = (\overline{\tau}_M)^{(0)}_{n+1} + c^r T_{n+1} - Y^r, \\ \boldsymbol{R}^{\boldsymbol{h}\,(0)}_{n+1} = \boldsymbol{h}^{in}_{n} - \boldsymbol{h}^{in\,(0)}_{n+1} + [\xi H^{cur} \lambda^r]^{(0)}_{n+1} (\partial_{\boldsymbol{\tau}} \overline{\tau}_M)^{(0)}_{n+1}, \\ \boldsymbol{R}^{\boldsymbol{\tau}\,(0)}_{n+1} = \boldsymbol{\mathcal{S}}_{n+1} : \boldsymbol{\tau}^{(0)}_{n+1} + \boldsymbol{\alpha}^{(0)}_{n+1} (T_{n+1} - T_0) + \boldsymbol{h}^{in\,(0)}_{n+1} - \boldsymbol{h}_{n+1}. \end{cases} \tag{4.19}$$

Linearizing the nonlinear system based on the unknowns $\{\Delta\lambda^{r\,(k)}_{n+1},\ \Delta\boldsymbol{\tau}^{(k)}_{n+1},\ \Delta\boldsymbol{h}^{in\,(k)}_{n+1}\}$,

$$\begin{cases} \Phi^{r\,(k)}_{n+1} + \partial_{\boldsymbol{\tau}} \Phi^{r\,(k)}_{f\,n+1} : \boldsymbol{\Delta\tau}^{(k)}_{n+1} + \partial_{\boldsymbol{h}^{in}} \Phi^{r\,(k)}_{f\,n+1} \boldsymbol{\Delta h}^{in\,(k)}_{n+1} & = 0, \\ \boldsymbol{R}^{\boldsymbol{h}\,(k)}_{n+1} + \partial_{\boldsymbol{\tau}} \boldsymbol{R}^{\boldsymbol{h}\,(k)}_{n+1} : \Delta\boldsymbol{\tau}^{(k)}_{n+1} + \partial_{\lambda^r} \boldsymbol{R}^{\boldsymbol{h}\,(k)}_{n+1} \Delta\lambda^{r\,(k)}_{n+1} + \partial_{\boldsymbol{h}^{in}} \boldsymbol{R}^{\boldsymbol{h}\,(k)}_{n+1} : \Delta\boldsymbol{h}^{in\,(k)}_{n+1} & = 0, \\ \boldsymbol{R}^{\boldsymbol{\tau}\,(k)}_{n+1} + \partial_{\boldsymbol{\tau}} \boldsymbol{R}^{\boldsymbol{\tau}\,(k)}_{n+1} : \Delta\boldsymbol{\tau}^{(k)}_{n+1} + \partial_{\boldsymbol{h}^{in}} \boldsymbol{R}^{\boldsymbol{\tau}\,(k)}_{n+1} : \Delta\boldsymbol{h}^{in\,(k)}_{n+1} & = 0. \end{cases} \tag{4.20}$$

The above system can be written as a linear system,

$$\mathbb{J}^{(k)}_{n+1} = \begin{bmatrix} (\partial_{\boldsymbol{\tau}} \overline{\tau}_M)^{(k)}_{n+1} & 0 & (\partial_{\boldsymbol{h}^{in}} \overline{\tau}_M)^{(k)}_{n+1} \\ [\xi H^{cur} \lambda^r \partial^2_{\boldsymbol{\tau}^2} (\overline{\tau}_M)]^{(k)}_{n+1} & [\xi H^{cur} \partial_{\boldsymbol{\tau}} (\overline{\tau}_M)]^{(k)}_{n+1} & -\boldsymbol{I} + [\xi H^{cur} \lambda^r (\partial_{\boldsymbol{h}^{in}} \partial_{\boldsymbol{\tau}} \overline{\tau}_M)]^{(k)}_{n+1} \\ \boldsymbol{\mathcal{S}}^{(k)}_{n+1} & \boldsymbol{0} & \boldsymbol{I} + \partial_{\boldsymbol{h}^{in}} \boldsymbol{\alpha}^{(k)}_{n+1} (T_{n+1} - T_0) \end{bmatrix}.$$

The expressions of symbols in matrix $\mathbb{J}_{n+1}^{(k)}$ are listed as follows,

$$\boldsymbol{\tau}_M' = \boldsymbol{\tau}_M : (\boldsymbol{I} - \frac{1}{3}\boldsymbol{\delta} \odot \boldsymbol{\delta}), \quad \boldsymbol{\tau}_M = \boldsymbol{M} : \boldsymbol{\tau}, \quad \boldsymbol{M} = \boldsymbol{I} - \boldsymbol{N} \odot \boldsymbol{N},$$

$$\partial_{\boldsymbol{\tau}} \overline{\tau}_M = \frac{3}{2} \frac{\boldsymbol{\tau}_M^{'}}{\overline{\tau}_M},$$

$$\partial_{\boldsymbol{h}^{in}} \overline{\tau}_M = -\frac{3}{2} \frac{(\boldsymbol{\tau} : \boldsymbol{N})\, \boldsymbol{\tau}_M^{'}}{\overline{\tau}_M \|\boldsymbol{h}^{in}\|},$$

$$\partial^2_{\boldsymbol{\tau}^2} \overline{\tau}_M = \frac{3}{2} \frac{1}{\overline{\tau}_M} \left(\boldsymbol{I} - \frac{1}{3}\boldsymbol{\delta} \odot \boldsymbol{\delta} - \boldsymbol{N} \odot \boldsymbol{N} - \frac{3}{2} \frac{\boldsymbol{\tau}_M^{'}}{\overline{\tau}_M} \odot \frac{\boldsymbol{\tau}_M^{'}}{\overline{\tau}_M} \right),$$

$$\partial_{\boldsymbol{h}^{in}} \partial_{\boldsymbol{h}^{\tau}} \overline{\tau}_M = \frac{3}{2} \frac{1}{\overline{\tau}_M \|\boldsymbol{h}^{in}\|} \left[-\boldsymbol{N} \odot \boldsymbol{\tau}_M^{'} - \boldsymbol{\tau}' : \boldsymbol{N} \left(\boldsymbol{I} - \boldsymbol{N} \odot \boldsymbol{N} - \frac{3}{2} \frac{\boldsymbol{\tau}_M^{'}}{\overline{\tau}_M} \odot \frac{\boldsymbol{\tau}_M^{'}}{\overline{\tau}_M} \right) \right].$$

4.2.6 Several yield surfaces active simultaneously

In this section, we will present the numerical implementation when several yield surfaces active simultaneously. There are five possible co-currencies of yield surfaces, and they are:

- forward phase transformation and orientation;
- forward phase transformation and reorientation;
- reverse phase transformation and reorientation;
- orientation and reorientation ;
- forward phase transformation, orientation and reorientation.

We take the co-currency of forward phase transformation and reorientation as an example to describe the numerical iterations of combined internal state variables evolution induced by more than one yield surface. The nonlinear system is given as follows,

$$
\begin{cases}
\Phi_{f\,n+1}^{t\,(0)} = (1-C)H_{n+1}^{cur}(\overline{\tau}R)_{n+1}^{(0)} + p_{n+1}^{(0)} - \mu_f^t(\xi_{n+1}^{(0)}) + \mathcal{Q}_r - Y^t, \\
\Phi_{n+1}^{r\,(0)} = (\overline{\tau}_M)_{n+1} + c^r T_{n+1}^{(0)} - Y^r, \\
\boldsymbol{R}_{n+1}^{\boldsymbol{h}\,(0)} = \boldsymbol{h}_n^{in} - \boldsymbol{h}_{n+1}^{in\,(0)} + (\xi_{n+1}^{(0)} - \xi_n)H_{n+1}^{cur}\partial_{\boldsymbol{\tau}}(R\overline{\tau})_{n+1}^{(0)} + [\xi H^{cur}\lambda^r]_{n+1}^{(0)}(\partial_{\boldsymbol{\tau}}\overline{\tau}_M)_{n+1}^{(0)}, \\
\boldsymbol{R}_{n+1}^{\boldsymbol{\tau}\,(0)} = \boldsymbol{\mathcal{S}}_{n+1}^{(0)} : \boldsymbol{\tau}_{n+1}^{(0)} + \boldsymbol{\alpha}_{n+1}^{(0)}(T_{n+1} - T_0) + \boldsymbol{h}_{n+1}^{in\,(0)} - \boldsymbol{h}_{n+1}.
\end{cases}
\tag{4.21}
$$

Linearizating the system, we get,

$$
\begin{cases}
\Phi_{f\,n+1}^{t\,(k)} + \partial_{\boldsymbol{\tau}}\Phi_{f\,n+1}^{t\,(k)} : \Delta\boldsymbol{\tau}_{n+1}^{(k)} + \partial_{\xi}\Phi_{f\,n+1}^{t\,(k)} : \Delta\xi_{n+1}^{(k)} = 0, \\
\Phi_{f\,n+1}^{r\,(k)} + \partial_{\boldsymbol{\tau}}\Phi_{f\,n+1}^{r\,(k)} : \boldsymbol{\Delta\tau}_{n+1}^{(k)} + \partial_{\boldsymbol{h}^{in}}\Phi_{f\,n+1}^{r\,(k)}\boldsymbol{\Delta h}_{n+1}^{in\,(k)} = 0, \\
\boldsymbol{R}_{n+1}^{\boldsymbol{h}\,(k)} + \partial_{\boldsymbol{\tau}}\boldsymbol{R}_{n+1}^{\boldsymbol{h}\,(k)} : \Delta\boldsymbol{\tau}_{n+1}^{(k)} + \partial_{\xi}\boldsymbol{R}_{n+1}^{\boldsymbol{h}\,(k)}\Delta\xi_{n+1}^{(k)} + \partial_{\lambda^r}\boldsymbol{R}_{n+1}^{\boldsymbol{h}\,(k)}\Delta\lambda_{n+1}^{r\,(k)} + \partial_{\boldsymbol{h}^{in}}\boldsymbol{R}_{n+1}^{\boldsymbol{h}\,(k)} : \Delta\boldsymbol{h}_{n+1}^{in\,(k)} = 0, \\
\boldsymbol{R}_{n+1}^{\boldsymbol{\tau}\,(k)} + \partial_{\boldsymbol{\tau}}\boldsymbol{R}_{n+1}^{\boldsymbol{\tau}\,(k)} : \Delta\boldsymbol{\tau}_{n+1}^{(k)} + \partial_{\xi}\boldsymbol{R}_{n+1}^{\boldsymbol{\tau}\,(k)}\Delta\xi_{n+1}^{(k)} + \partial_{\boldsymbol{h}^{in}}\boldsymbol{R}_{n+1}^{\boldsymbol{\tau}\,(k)} : \Delta\boldsymbol{h}_{n+1}^{in\,(k)} = 0.
\end{cases}
\tag{4.22}
$$

The linearilized system can be written in the following matrix format,

$$
\mathbb{J}^{(k)} \cdot \Delta\mathbb{X}^{(k)} = \mathbb{B}^{(k)},
$$

where,

$$\mathbb{J}_{n+1}^{(k)} = \begin{bmatrix} [(1-C)H^{cur}\partial_{\boldsymbol{\tau}}(R\overline{\tau}) + \Delta\boldsymbol{\mathcal{S}} : \boldsymbol{\tau} + \partial_{\xi}\boldsymbol{\alpha}(T-T_0)]_{n+1}^{(k)} & -\partial_{\xi}\mu_{f\ n+1}^{t\ (k)} \\ \partial_{\boldsymbol{\tau}}(\overline{\tau}_M)_{n+1}^{(k)} & 0 \\ (\xi_{n+1}^{(k)} - \xi_n)[H^{cur}\partial_{\boldsymbol{\tau}^2}^2(R\overline{\tau})]_{n+1}^{(k)} + [\xi H^{cur}\lambda^r\partial_{\boldsymbol{\tau}^2}^2\overline{\tau}_M]_{n+1}^{(k)} & [H^{cur}\partial_{\boldsymbol{\tau}}(R\overline{\tau})]_{n+1}^{(k)} \\ \boldsymbol{\mathcal{S}}_{n+1}^{(k)} & \Delta\boldsymbol{\mathcal{S}} : \boldsymbol{\tau}_{n+1}^{(k)} + \partial_{\xi}\boldsymbol{\alpha}_{n+1}^{(k)}(T-T_0) \end{bmatrix}$$

$$\begin{bmatrix} 0 & \mathbf{0} \\ 0 & \partial_{\boldsymbol{h}^{in}}(\overline{\tau}_M)_{n+1}^{(k)} \\ [\xi H^{cur}\partial_{\boldsymbol{\tau}}\overline{\tau}_M]_{n+1}^{(k)} & -\boldsymbol{I} + [\xi H^{cur}\lambda^r(\partial_{\boldsymbol{h}^{in}}\partial_{\boldsymbol{\tau}}\overline{\tau}_M)]_{n+1}^{(k)} \\ 0 & \boldsymbol{I} + \partial_{\boldsymbol{h}^{in}}\boldsymbol{\alpha}_{n+1}^{(k)}(T-T_0) \end{bmatrix},$$

$$\Delta\mathbb{X}_{n+1}^{(k)} = \begin{bmatrix} \Delta\boldsymbol{\tau}_{n+1}^{(k)} \\ \Delta\xi_{n+1}^{(k)} \\ \Delta\lambda_{n+1}^{r\ (k)} \\ \Delta\boldsymbol{h}_{n+1}^{in\ (k)} \end{bmatrix}, \qquad \mathbb{B}_{f\ n+1}^{(k)} = \begin{bmatrix} -\boldsymbol{\Phi}_{f\ n+1}^{t\ (k)} \\ -\boldsymbol{\Phi}_{n+1}^{r\ (k)} \\ -\boldsymbol{R}_{n+1}^{\boldsymbol{h}\ (k)} \\ -\boldsymbol{R}_{n+1}^{\boldsymbol{\tau}\ (k)} \end{bmatrix}.$$

Expressions in $\mathbb{J}$ are listed previously.

4.3 Consistent Tangent Moduli Tensors

This section demonstrates the algorithmic process of calculating the consistent tangent moduli tensor of the proposed constitutive model. As shown previously, the solution of the rate-type constitutive model is obtained through integrating a number of time steps. The stress tensor, as a result of the process, is defined as a function of the deformation history as well as temperature history up to a given instant. The global finite element problem is commonly solved by the the well-known Newton's iteration method and the tangent moduli tensor is important to maintain the quadratic rate of asymptotic convergence in the linearized problem. In other words, the notion of a consistent tangent stiffness tensor and tangent thermal moduli tensor arises due to the enforcement of the consistency condition on the discrete algorithmic problem. The tangent moduli are the tensors that relate the strain and temperature increments (input) to the calculated stress increment (output). It should be written in an incremental form as follows,

$$\Delta\boldsymbol{\tau}_{n+1} = \mathcal{L} : \Delta\boldsymbol{h}_{n+1} + \boldsymbol{\Theta}\Delta T_{n+1}, \tag{4.23}$$

where $\mathcal{L}$ is the tangent stiffness tensor and $\boldsymbol{\Theta}$ is the tangent thermal moduli tensor.

Considering the constitutive relation

$$\boldsymbol{\mathcal{S}}^{-1} : \boldsymbol{\tau} = \boldsymbol{h} - \boldsymbol{\alpha}(T - T_0) - \boldsymbol{h}^t - \boldsymbol{h}^o - \boldsymbol{h}^r, \tag{4.24}$$

and the incremental form of the constitutive relation based on the time increments is given as,

$$\boldsymbol{\mathcal{S}} : \Delta\boldsymbol{\tau} + \Delta\xi\Delta\boldsymbol{\mathcal{S}} : \boldsymbol{\tau} = \boldsymbol{d} - \boldsymbol{\alpha}\Delta T - \boldsymbol{\Delta\alpha}(T - T_0) - \Delta\boldsymbol{h}^t - \Delta\boldsymbol{h}^o - \Delta\boldsymbol{h}^r. \tag{4.25}$$

Accounting for the expression of thermal expansion (Eqn. 3.61) and evolution

law of yield surfaces, we finally obtain [10]

$$\boldsymbol{\mathcal{S}} : \Delta\boldsymbol{\tau} + \Delta\xi\Delta\boldsymbol{\mathcal{S}} : \boldsymbol{\tau} \doteq \boldsymbol{d} - \boldsymbol{\alpha}\Delta T - \left[\Delta\xi\partial_{\xi}\boldsymbol{\alpha} + \Delta H\partial_{H}\boldsymbol{\alpha} + \Delta\lambda^{r}H\xi\partial_{\boldsymbol{h}^{in}}\boldsymbol{\alpha} : \boldsymbol{\Lambda}^{r}\right](T - T_0) \\ - \Delta\xi H\boldsymbol{\Lambda}^{t} - \Delta H\xi\boldsymbol{\Lambda}^{o} - \Delta\lambda^{r}H\xi\boldsymbol{\Lambda}^{r}. \tag{4.26}$$

This section will demonstrate the detailed procedure of calculating the consistent tangent moduli when only forward phase transformation active, and then list the tangent moduli tensors in all possible conditions.

Forward Phase Transformation

The incremental form of constitutive relation reduces to Eqn. (4.27) if the forward phase transformation is the only active yield surface,

$$\begin{aligned}\boldsymbol{\mathcal{S}} : \Delta\boldsymbol{\tau} &= \Delta\boldsymbol{h} - \boldsymbol{\alpha}\Delta T - \Delta\xi\Delta\boldsymbol{\mathcal{S}} : \boldsymbol{\tau} - \Delta\xi\partial_{\xi}\boldsymbol{\alpha}(T - T_0) - \Delta\xi H\partial_{\boldsymbol{\tau}}(R\overline{\tau}) \\ &= \Delta\boldsymbol{h} - \boldsymbol{\alpha}\Delta T - \Delta\xi\partial_{\tau}\Phi_{f}^{t}.\end{aligned} \tag{4.27}$$

According to the Kuhn-Tucker consistency condition, the differentiation of the transformation function results in[11],

$$\Delta\Phi_{f}^{t} = \partial_{\boldsymbol{\tau}}\Phi_{f}^{t} : \Delta\boldsymbol{\tau} + \partial_{T}\Phi_{f}^{t}\Delta T + \partial_{\xi}\Phi_{f}^{t}\Delta\xi = 0. \tag{4.28}$$

Substitute the constitutive relation (4.27) into the consistency condition, we obtain Eqn. (4.29),

$$\partial_{\boldsymbol{\tau}}\Phi_{f}^{t} : \left\{\boldsymbol{\mathcal{S}}^{-1} : \left[\Delta\boldsymbol{h} - \boldsymbol{\alpha}\Delta T - \Delta\xi\partial_{\boldsymbol{\tau}}\Phi_{f}^{t}\right]\right\} + \partial_{T}\Phi_{f}^{t}\Delta T + \partial_{\xi}\Phi_{f}^{t}\Delta\xi = 0. \tag{4.29}$$

[10] We need to note the slight difference between thermodynamic forces π we defined in the constitutive model and the kirchhoff stress τ.The relation is defined as $\boldsymbol{\pi} = \left[\boldsymbol{I} + \alpha^{M}\xi^{2}\frac{H}{H^{max}}\frac{\boldsymbol{I}-\boldsymbol{N}\otimes\boldsymbol{N}}{\|\boldsymbol{h}^{in}\|}(T - T_0)\right] : \boldsymbol{\tau} = \boldsymbol{K} : \boldsymbol{\tau}$, and the symbol $\doteq$ in Eqn. (4.26) is denoted that the minor difference of the two tensor can be neglected in numerical calculation

[11] In this section, the superscript indicates the active yield surfaces, and ^{t} stands for phase transformation, ^{r} for reorientation and ^{o} for orientation respectively. Moreover, forward and reverse phase transformation are distinguished by the subscript $_{f}$ for forward and $_{r}$ for reverse respectively. For instances, symbols $^{to}_{f}$ represents forward phase transformation and orientation active simultaneously

Then the increment of state variable $\Delta\xi$ can be expressed by the given increments (strain and temperature) as Eqn. (4.30),

$$\Delta\xi = \frac{\partial_{\boldsymbol{\tau}}\Phi_f^t : \boldsymbol{\mathcal{S}}^{-1} : \Delta\boldsymbol{h} + (\partial_T\Phi_f^t - \partial_{\boldsymbol{\tau}}\Phi_f^t : \boldsymbol{\mathcal{S}}^{-1} : \boldsymbol{\alpha})\Delta T}{\partial_{\boldsymbol{\tau}}\Phi_f^t : \boldsymbol{\mathcal{S}}^{-1} : \partial_{\boldsymbol{\tau}}\Phi_f^t - \partial_{\xi}\Phi_f^t}. \tag{4.30}$$

Subtitute the expression of $\Delta\xi$ Eqn. (4.30) into constitutive Eqn. (4.29), we are able to obtain the stiffness moduli and thermal moduli tensor,

$$\Delta\boldsymbol{\tau} = \mathcal{L}_f^t : \Delta\boldsymbol{h} + \boldsymbol{\Theta}_f^t\Delta T, \tag{4.31}$$

where,

$$\boldsymbol{\mathcal{L}}_f^t = \boldsymbol{\mathcal{S}}^{-1} - \boldsymbol{\mathcal{S}}^{-1} : \partial_{\boldsymbol{\tau}}\Phi_f^t \odot \boldsymbol{\mathcal{Z}}_{f\,\xi}^t, \text{ and } \boldsymbol{\Theta}_f^t = \boldsymbol{\mathcal{L}}_f^t : \boldsymbol{\alpha} - \mathcal{T}_{f\,\xi}^t\boldsymbol{\mathcal{S}}^{-1} : \partial_{\boldsymbol{\tau}}\Phi_f^t.$$

The expression of the symbols are shown as follows:

$$\boldsymbol{\mathcal{Z}}_{f\,\xi}^t = \frac{\partial_{\boldsymbol{\tau}}\Phi_f^t : \boldsymbol{\mathcal{S}}^{-1}}{a_f^t}, \qquad \mathcal{T}_{f\,\xi}^t = \frac{\partial_T\Phi_f^t}{a_f^t},$$
$$a_f^t = \partial_{\boldsymbol{\tau}}\Phi_f^t : \boldsymbol{\mathcal{S}}^{-1} : \partial_{\boldsymbol{\tau}}\Phi_f^t - \partial_{\xi}\Phi_f^t.$$

Reverse Phase Transformation

$\boldsymbol{\mathcal{L}}_r^t$ and $\boldsymbol{\Theta}_r^t$ represent stiffness tangent moduli and thermal tangent moduli respectively when reverse phase transformation is the only active yield surface,

$$\Delta\boldsymbol{\tau} = \boldsymbol{\mathcal{L}}_r^t : \Delta\boldsymbol{h} - \boldsymbol{\Theta}_r^t : \Delta T, \tag{4.32}$$

where,

$$\boldsymbol{\mathcal{L}}_r^t = \boldsymbol{\mathcal{S}}^{-1} - \boldsymbol{\mathcal{S}}^{-1} : \partial_{\boldsymbol{\tau}}\Phi_r^t \odot \boldsymbol{\mathcal{Z}}_{r\,\xi}^t, \text{ and } \boldsymbol{\Theta}_r^t = \boldsymbol{\mathcal{L}}_r^t : \boldsymbol{\alpha} - \mathcal{T}_{r\,\xi}^t\boldsymbol{\mathcal{S}}^{-1} : \partial_{\boldsymbol{\tau}}\Phi_r^t.$$

The expression of the symbols are shown as follows:

$$\boldsymbol{\mathcal{Z}}^t_{r\,\xi} = \frac{\partial_{\boldsymbol{\tau}}\Phi^t_r : \boldsymbol{\mathcal{S}}^{-1}}{a^t_f}, \qquad \mathcal{T}^t_{r\,\xi} = \frac{\partial_T \Phi^t_r}{a^t_r},$$
$$a^t_f = \partial_{\boldsymbol{\tau}}\Phi^t_r : \boldsymbol{\mathcal{S}}^{-1} : \partial_{\boldsymbol{\tau}}\Phi^t_r + \partial_{\xi}\Phi^t_r.$$

Orientation Yield Surfaces

$\boldsymbol{\mathcal{L}}^o$ and $\boldsymbol{\Theta}^o$ represent stiffness tangent moduli and thermal tangent moduli respectively when orientation is the only active yield surface,

$$\Delta\boldsymbol{\tau} = \boldsymbol{\mathcal{L}}^o : \Delta\boldsymbol{h} - \boldsymbol{\Theta}^o : \Delta T, \tag{4.33}$$

where,

$$\boldsymbol{\mathcal{L}}^o = \boldsymbol{\mathcal{S}}^{-1} - \boldsymbol{\mathcal{S}}^{-1} : \xi\partial_{\boldsymbol{\tau}}\Phi^o \odot \boldsymbol{\mathcal{Z}}^o_{H^{cur}}, \text{ and } \boldsymbol{\Theta}^o = \boldsymbol{\mathcal{L}}^o : \boldsymbol{\alpha} - \mathcal{T}^o_{H^{cur}}\boldsymbol{\mathcal{S}}^{-1} : \xi\partial_{\boldsymbol{\tau}}\Phi^o.$$

The expression of the symbols are displayed as follows:

$$\boldsymbol{\mathcal{Z}}^o_{H^{cur}} = \frac{\partial_{\boldsymbol{\tau}}\Phi^o : \boldsymbol{\mathcal{S}}^{-1}}{a^o}, \qquad \mathcal{T}^o_{H^{cur}} = \frac{\partial_T \Phi^o}{a^o},$$
$$a^o = \xi\partial_{\boldsymbol{\tau}}\Phi^o : \boldsymbol{\mathcal{S}}^{-1} : \partial_{\boldsymbol{\tau}}\Phi^o - \partial_{H^{cur}}\Phi^o.$$

Reorientation Yield Surface

$\boldsymbol{\mathcal{L}}^r$ and $\boldsymbol{\Theta}^r$ represent stiffness tangent moduli and thermal tangent moduli of reorientation yield surface,

$$\Delta\boldsymbol{\tau} = \boldsymbol{\mathcal{L}}^r : \Delta\boldsymbol{h} - \boldsymbol{\Theta}^r : \Delta T, \tag{4.34}$$

where,

$$\boldsymbol{\mathcal{L}}^r = \boldsymbol{\mathcal{S}}^{-1} - \boldsymbol{\mathcal{S}}^{-1} : \partial_{\boldsymbol{\tau}} \Phi^r \odot \boldsymbol{\mathcal{Z}}^r_{\lambda^r}, \text{ and } \boldsymbol{\Theta}^r = \boldsymbol{\mathcal{L}}^r : \boldsymbol{\alpha} - \mathcal{T}^r_{\lambda^r} \boldsymbol{\mathcal{S}}^{-1} : \partial_{\boldsymbol{\tau}} \Phi^r.$$

The expressions of symbols $\boldsymbol{\mathcal{Z}}^r_{\lambda^r}$, $\mathcal{T}^r_{\lambda^r}$ are listed:

$$\boldsymbol{\mathcal{Z}}^r_{\lambda^r} = \frac{\partial_{\boldsymbol{\tau}} \Phi^r : \boldsymbol{\mathcal{S}}^{-1}}{a^r}, \qquad \mathcal{T}^r_{\lambda^r} = \frac{\partial_T \Phi^r}{a^r},$$
$$a^r = \partial_{\boldsymbol{\tau}} \Phi^r : \boldsymbol{\mathcal{S}}^{-1} : \partial_{\boldsymbol{\tau}} \Phi^r - \partial_{\boldsymbol{h}^{in}} \Phi^r : \partial_{\boldsymbol{\tau}} \Phi^r.$$

Forward and Orientation

$\boldsymbol{\mathcal{L}}^{to}_f$ and $\boldsymbol{\Theta}^{to}_f$ represent stiffness tangent moduli and thermal tangent moduli respectively when forward phase transformation and orientation yield surfaces active simulteneously,

$$\Delta \boldsymbol{\tau} = \boldsymbol{\mathcal{L}}^{to}_f : \Delta \boldsymbol{h} - \boldsymbol{\Theta}^{to}_f : \Delta T, \tag{4.35}$$

where,

$$\boldsymbol{\mathcal{L}}^{to}_f = \boldsymbol{\mathcal{S}}^{-1} - \boldsymbol{\mathcal{S}}^{-1} : \partial_{\boldsymbol{\tau}} \Phi^t_f \odot \boldsymbol{\mathcal{Z}}^{to}_{f\,\xi} - \boldsymbol{\mathcal{S}}^{-1} : \xi \partial_{\boldsymbol{\tau}} \xi \Phi^o \odot \boldsymbol{\mathcal{Z}}^{to}_{f\,H^{cur}},$$

and

$$\boldsymbol{\Theta}^{to}_f = \boldsymbol{\mathcal{L}}^{to}_f : \boldsymbol{\alpha} - \mathcal{T}^{to}_{f\,\xi} \boldsymbol{\mathcal{S}}^{-1} : \partial_{\boldsymbol{\tau}} \Phi^t_f - \mathcal{T}^{to}_{f\,H^{cur}} \boldsymbol{\mathcal{S}}^{-1} : \xi \partial_{\boldsymbol{\tau}} \Phi^o.$$

The detailed expressions of the symbols are listed following:

$$\boldsymbol{\mathcal{Z}}^{to}_{f\,\xi} = \frac{(a^{oo}\partial_{\boldsymbol{\tau}}\Phi^t_f - a^{to}_f\partial_{\boldsymbol{\tau}}\Phi^o) : \boldsymbol{\mathcal{S}}^{-1}}{a^{tt}_f a^{oo} - a^{ot}_f a^{to}_f}, \qquad \mathcal{T}^{to}_{f\,\xi} = \frac{(a^{oo}\partial_T\Phi^t_f - a^{to}_f\partial_T\Phi^o) : \boldsymbol{\mathcal{S}}^{-1}}{a^{tt}_f a^{oo} - a^{ot}_f a^{to}_f},$$

$$\boldsymbol{\mathcal{Z}}^{to}_{H^{cur}} = \frac{(a^{ot}_f\partial_{\boldsymbol{\tau}}\Phi^t_f - a^{tt}_f\partial_{\boldsymbol{\tau}}\Phi^o) : \boldsymbol{\mathcal{S}}^{-1}}{a^{ot}_f a^{to}_f - a^{tt}_f a^{oo}}, \qquad \mathcal{T}^{to}_{f\,H^{cur}} = \frac{(a^{ot}_f\partial_T\Phi^t_f - a^{tt}_f\partial_T\Phi^o) : \boldsymbol{\mathcal{S}}^{-1}}{a^{ot}a^{to}_f - a^{tt}_f a^{oo}},$$

$$a^{tt}_f = \partial_{\boldsymbol{\tau}}\Phi^t_f : \boldsymbol{\mathcal{S}}^{-1} : \partial_{\boldsymbol{\tau}}\Phi^t_f - \partial_\xi\Phi^t_f, \qquad a^{to}_f = \xi\partial_{\boldsymbol{\tau}}\Phi^t_f : \boldsymbol{\mathcal{S}}^{-1} : \partial_{\boldsymbol{\tau}}\Phi^o - \partial_{H^{cur}}\Phi^t_f,$$

$$a^{oo} = \partial_{\boldsymbol{\tau}}\Phi^o : \boldsymbol{\mathcal{S}}^{-1} : \xi\partial_{\boldsymbol{\tau}}\Phi^o - \partial_{H^{cur}}\Phi^o, \qquad a^{ot}_f = \partial_{\boldsymbol{\tau}}\Phi^o : \boldsymbol{\mathcal{S}}^{-1} : \partial_{\boldsymbol{\tau}}\Phi^t_f.$$

Forward and Reorientation

$\boldsymbol{\mathcal{L}}^{tr}_f$ and $\boldsymbol{\Theta}^{tr}_f$ represent stiffness tangent moduli and thermal tangent moduli respectively when forward phase transformation and reorientation yield surfaces active simultaneously,

$$\Delta\boldsymbol{\tau} = \boldsymbol{\mathcal{L}}^{tr}_f : \Delta\boldsymbol{h} + \boldsymbol{\Theta}^{tr}_f\Delta T, \tag{4.36}$$

where,

$$\boldsymbol{\mathcal{L}}^{tr}_f = \boldsymbol{\mathcal{S}}^{-1} - \boldsymbol{\mathcal{S}}^{-1} : \partial_{\boldsymbol{\tau}}\Phi^t_f \otimes \boldsymbol{\mathcal{Z}}^{tr}_{f\,\xi} - \boldsymbol{\mathcal{S}}^{-1} : \partial_{\boldsymbol{\tau}}\Phi^r \otimes \boldsymbol{\mathcal{Z}}^{tr}_{f\,\lambda^r},$$

and

$$\boldsymbol{\Theta}^{tr}_f = -\boldsymbol{\mathcal{L}}^{tr}_f : \boldsymbol{\alpha} - \mathcal{T}_\xi\boldsymbol{\mathcal{S}}^{-1} : \partial_{\boldsymbol{\tau}}\Phi^t_f - \mathcal{T}_{\lambda^r}\boldsymbol{\mathcal{S}}^{-1} : \partial_{\boldsymbol{\tau}}\Phi^r.$$

The expressions of the symbols in the modulus tensor are as follows:

$$\boldsymbol{\mathcal{Z}}^{tr}_{f\,\xi} = \frac{(a^{rr}\partial_{\boldsymbol{\tau}}\Phi^t_f - a^{tr}_f\partial_{\boldsymbol{\tau}}\Phi^r) : \boldsymbol{\mathcal{S}}^{-1}}{a^{tt}_f a^{rr} - a^{rt}_f a^{tr}_f}, \qquad \mathcal{T}^{tr}_{f\,\xi} = \frac{a^{rr}\partial_T\Phi^t_f - a^{tr}_f\partial_T\Phi^r}{a^{tt}_f a^{rr} - a^{rt}_f a^{tr}_f},$$

$$\boldsymbol{\mathcal{Z}}^{tr}_{f\,\lambda^r} = \frac{(a^{rt}_f\partial_{\boldsymbol{\tau}}\Phi^t_f - a^{tt}_f\partial_{\boldsymbol{\tau}}\Phi^r) : \boldsymbol{\mathcal{S}}^{-1}}{a^{rt}_f a^{tr}_f - a^{tt}_f a^{rr}}, \qquad \mathcal{T}^{tr}_{f\,\lambda^r} = \frac{a^{rt}_f\partial_T\Phi^t_f - a^{tt}_f\partial_T\Phi^r}{a^{tt}_f a^{rr} - a^{rt}_f a^{tr}_f},$$

$$a^{tt}_f = \partial_{\boldsymbol{\tau}}\Phi^t_f : \boldsymbol{\mathcal{S}}^{-1} : \partial_{\boldsymbol{\tau}}\Phi^t_f - \partial_{\xi}\Phi^t_f, \qquad a^{tr}_f = \partial_{\boldsymbol{\tau}}\Phi^t_f : \boldsymbol{\mathcal{S}}^{-1} : \partial_{\boldsymbol{\tau}}\Phi^r,$$

$$a^{rr} = \partial_{\boldsymbol{\tau}}\Phi^r : \boldsymbol{\mathcal{S}}^{-1} : \partial_{\boldsymbol{\tau}}\Phi^r - \partial_{\boldsymbol{h}^{in}}\Phi^r : \partial_{\boldsymbol{\tau}}\Phi^r, \qquad a^{rt}_f = \partial_{\boldsymbol{\tau}}\Phi^t_f : \boldsymbol{\mathcal{S}}^{-1} : \partial_{\boldsymbol{\tau}}\Phi^r - \partial_{\boldsymbol{h}^{in}}\Phi^r : \partial_{\boldsymbol{\tau}}\Phi^t_f.$$

Reverse and Reorientation

$\boldsymbol{\mathcal{L}}^{tr}_r$ and $\boldsymbol{\Theta}^{tr}_r$ represent stiffness tangent moduli and thermal tangent moduli respectively when forward phase transformation and reorientation yield surfaces active simultaneously,

$$\Delta\boldsymbol{\tau} = \boldsymbol{\mathcal{L}}^{tr}_r : \Delta\boldsymbol{h} + \boldsymbol{\Theta}^{tr}_r\Delta T, \tag{4.37}$$

where,

$$\boldsymbol{\mathcal{L}}^{tr}_r = \boldsymbol{\mathcal{S}}^{-1} - \boldsymbol{\mathcal{S}}^{-1} : \partial_{\boldsymbol{\tau}}\Phi^t_r \otimes \boldsymbol{\mathcal{Z}}^{tr}_{r\,\xi} - \boldsymbol{\mathcal{S}}^{-1} : \partial_{\boldsymbol{\tau}}\Phi^r \otimes \boldsymbol{\mathcal{Z}}^{tr}_{r\,\lambda^r},$$

and

$$\boldsymbol{\Theta}^{tr}_f = -\boldsymbol{\mathcal{L}}^{tr}_r : \boldsymbol{\alpha} - \mathcal{T}_{\xi}\boldsymbol{\mathcal{S}}^{-1} : \partial_{\boldsymbol{\tau}}\Phi^t_r - \mathcal{T}_{\lambda^r}\boldsymbol{\mathcal{S}}^{-1} : \partial_{\boldsymbol{\tau}}\Phi^r.$$

The expressions of the symbols in the moduli tensor are as follows:

$$\boldsymbol{\mathcal{Z}}^{tr}_{r\,\xi} = \frac{(a^{rr}\partial_{\boldsymbol{\tau}}\Phi^t_f - a^{tr}_r\partial_{\boldsymbol{\tau}}\Phi^r) : \boldsymbol{\mathcal{S}}^{-1}}{a^{tt}_r a^{rr} - a^{rt}_r, a^{tr}_f}, \qquad \mathcal{T}^{tr}_{r\,\xi} = \frac{a^{rr}\partial_T\Phi^t_r - a^{tr}_r\partial_T\Phi^r}{a^{tt}_f a^{rr} - a^{rt}_r a^{tr}_r},$$

$$\boldsymbol{\mathcal{Z}}^{tr}_{r\,\lambda^r} = \frac{(a^{rt}_r\partial_{\boldsymbol{\tau}}\Phi^t_r - a^{tt}_r\partial_{\boldsymbol{\tau}}\Phi^r) : \boldsymbol{\mathcal{S}}^{-1}}{a^{rt}_f a^{tr}_r - a^{tt}_f a^{rr}}, \qquad \mathcal{T}^{tr}_{r\,\lambda^r} = \frac{a^{rt}_r\partial_T\Phi^t_r - a^{tt}_r\partial_T\Phi^r}{a^{tt}_f a^{rr} - a^{rt}_r a^{tr}_r},$$

$$a^{tt}_r = \partial_{\boldsymbol{\tau}}\Phi^t_f : \boldsymbol{\mathcal{S}}^{-1} : \partial_{\boldsymbol{\tau}}\Phi^t_f - \partial_{\xi}\Phi^t_f, \qquad a^{tr}_r = \partial_{\boldsymbol{\tau}}\Phi^t_r : \boldsymbol{\mathcal{S}}^{-1} : \partial_{\boldsymbol{\tau}}\Phi^r,$$

$$a^{rr} = \partial_{\boldsymbol{\tau}}\Phi^r : \boldsymbol{\mathcal{S}}^{-1} : \partial_{\boldsymbol{\tau}}\Phi^r - \partial_{\boldsymbol{h}^{in}}\Phi^r : \partial_{\boldsymbol{\tau}}\Phi^r, \qquad a^{rt}_r = \partial_{\boldsymbol{\tau}}\Phi^t_r : \boldsymbol{\mathcal{S}}^{-1} : \partial_{\boldsymbol{\tau}}\Phi^r - \partial_{\boldsymbol{h}^{in}}\Phi^r : \partial_{\boldsymbol{\tau}}\Phi^t_r.$$

Orientation and Reorientation

$\boldsymbol{\mathcal{L}}^{or}_f$ and $\boldsymbol{\Theta}^{or}_f$ represent stiffness tangent moduli and thermal tangent moduli respectively when martensite variants orients and reorients simulteneously,

$$\Delta\boldsymbol{\tau} = \boldsymbol{\mathcal{L}}^{or} : \Delta\boldsymbol{h} - \boldsymbol{\Theta}^{or} : \Delta T, \tag{4.38}$$

where,

$$\boldsymbol{\mathcal{L}}^{or} = \boldsymbol{\mathcal{S}}^{-1} - \boldsymbol{\mathcal{S}}^{-1} : \xi\partial_{\boldsymbol{\tau}}\Phi^o \odot \boldsymbol{\mathcal{Z}}^{or}_{H^{cur}} - \boldsymbol{\mathcal{S}}^{-1} : \partial_{\boldsymbol{\tau}}\Phi^r \odot \boldsymbol{\mathcal{Z}}^{or}_{\lambda^r},$$

and

$$\boldsymbol{\Theta}^{or} = \boldsymbol{\mathcal{L}}^{or} : \boldsymbol{\alpha} - \mathcal{T}^{or}_{H^{cur}}\boldsymbol{\mathcal{S}}^{-1} : \xi\partial_{\boldsymbol{\tau}}\Phi^o - \mathcal{T}^{or}_{\lambda^r}\boldsymbol{\mathcal{S}}^{-1} : \partial_{\boldsymbol{\tau}}\Phi^r.$$

The detailed expressions are given as follows:

$$\boldsymbol{\mathcal{Z}}^{or}_{H^{cur}} = \frac{(a^{rr}\partial_{\boldsymbol{\tau}}\Phi^o - a^{or}\partial_{\boldsymbol{\tau}}\Phi^r) : \boldsymbol{\mathcal{S}}^{-1}}{a^{rr}a^{oo} - a^{ro}a^{or}}, \qquad \mathcal{T}^{or}_{H^{cur}} = \frac{(a^{rr}\partial_T\Phi^o - a^{or}\partial_T\Phi^r) : \boldsymbol{\mathcal{S}}^{-1}}{a^{rr}a^{oo} - a^{ro}a^{or}},$$

$$\boldsymbol{\mathcal{Z}}^{or}_{\lambda^r} = \frac{(a^{ro}\partial_{\boldsymbol{\tau}}\Phi^o - a^{oo}\partial_{\boldsymbol{\tau}}\Phi^r) : \boldsymbol{\mathcal{S}}^{-1}}{a^{ro}a^{or} - a^{rr}a^{oo}}, \qquad \mathcal{T}^{or}_{\lambda^r} = \frac{(a^{ro}\partial_T\Phi^t_f - a^{oo}\partial_T\Phi^o) : \boldsymbol{\mathcal{S}}^{-1}}{a^{ro}a^{or} - a^{rr}a^{oo}},$$

$$a^{oo} = \partial_{\boldsymbol{\tau}}\Phi^t_f : \boldsymbol{\mathcal{S}}^{-1} : \xi\partial_{\boldsymbol{\tau}}\Phi^o - \partial_{H^{cur}}\Phi^o, \qquad a^{or} = \partial_{\boldsymbol{\tau}}\Phi^o : \boldsymbol{\mathcal{S}}^{-1} : \partial_{\boldsymbol{\tau}}\Phi^r,$$

$$a^{rr} = \partial_{\boldsymbol{\tau}}\Phi^r : \boldsymbol{\mathcal{S}}^{-1} : \partial_{\boldsymbol{\tau}}\Phi^r - \partial_{\boldsymbol{h}^{in}}\Phi^r : \partial_{\boldsymbol{\tau}}\Phi^r, \qquad a^{ro} = \partial_{\boldsymbol{\tau}}\Phi^r : \boldsymbol{\mathcal{S}}^{-1} : \xi\partial_{\boldsymbol{\tau}}\Phi^o - \partial_{\boldsymbol{h}^{in}}\Phi^r : \xi\partial_{\boldsymbol{\tau}}\Phi^o.$$

5 NUMERICAL SIMULATIONS AND DISCUSSION

In this section, the three-fold task of verifying the model's ability to reproduce the intended characteristics of the thermomechanical response of SMAs, validating it against experimental data obtained under complex non-proportional loading conditions, and testing the robustness and efficiency of the numerical implementation is undertaken. Note that whenever no values are provided for certain parameters, these parameters are insignificant for the respective simulations, *e.g.*, reorientation related parameters for proportional loading simulations.

5.1 Proportional Loading

Here, orientation, phase transformation, rate effects, and minor loops are simulated under uniaxial loading paths. It is worth noting that reorientation cannot be triggered from proportional loading and it is thus insignificant in these simulations.

5.1.1 Orientation & phase transformation

In Figure 5.1, the material's deformation response for a loading path that results in shape memory, orientation, and psuedoelasticity is shown. An initially austenitic material is cooled from 300 to 220 K under zero bias load. The resulted self-accommodated martensite is loaded in tension uniaxially and isothermaly to a maximum stress of 320 MPa, resulting in orientation. Subsequent unloading does not alter the orientation-induced deformation. Heating at zero stress to a maximum temperature of 300 K induces the shape memory effect, *i.e.*, reverse phase transformation takes place and the orientation strain is recovered. Then the material is loaded again in tension undergoing forward phase transformation and transformation-induced deformation which is recovered upon unloading due

Table 3: Closet Point projection implicit algorithm for shape memory alloys

1.Known $\begin{cases} \text{Solved by global interation} & \boldsymbol{u}_n, \boldsymbol{u}_{n+1}\ (\boldsymbol{\varepsilon}_n, \boldsymbol{\varepsilon}_{n+1});\ \boldsymbol{F}_n, \boldsymbol{F}_{n+1};\ T_n, T_{n+1};\ \boldsymbol{\tau}_n \\ \text{Internal State Variables} & \kappa_n^t;\ \kappa_n^o;\ \kappa_n^r;\ \boldsymbol{h}_n^{in} \end{cases}$

2.Pre-Calculation (Finite Strain Only)

Calculate the Hencky strain, rate of deformation and increment of rotation, and rotate relative variables

$$\boldsymbol{h}_n = \frac{1}{2}\ln(\boldsymbol{F}_n\boldsymbol{F}_n^T),\ \boldsymbol{h}_{n+1} = \frac{1}{2}\ln(\boldsymbol{F}_{n+1}\boldsymbol{F}_{n+1}^T)$$

$$\boldsymbol{D}_{n+1} = \frac{1}{2}\left[\frac{\boldsymbol{F}_{n+1}-\boldsymbol{F}_n}{\Delta t}\boldsymbol{F}_{n+1}^{-1} + \left(\frac{\boldsymbol{F}_{n+1}-\boldsymbol{F}_n}{\Delta t}\boldsymbol{F}_{n+1}^{-1}\right)^T\right]$$

$$\Delta\boldsymbol{R}_{n+1}^{log} = \exp\left(\boldsymbol{\Omega}_{n+1}^{log}\Delta t\right)$$

$$\boldsymbol{h}_n^{in} = \Delta\boldsymbol{R}_{n+1}^{log}\boldsymbol{h}_n^{in}\Delta\boldsymbol{R}_{n+1}^{log\,T};\ \boldsymbol{\tau}_n = \Delta\boldsymbol{R}_{n+1}^{log}\boldsymbol{\tau}_n\Delta\boldsymbol{R}_{n+1}^{log\,T}$$

3. Thermoelastc Prediction. Let

$$k=0;\ \kappa_{n+1}^{t\,(0)} = \kappa_n^t;\ \kappa_{n+1}^{o\,(0)} = \kappa_n^o;\ \kappa_{n+1}^{r\,(0)} = \kappa_n^r;\ \boldsymbol{h}_{n+1}^{in\,(0)} = \boldsymbol{h}_n^{in}$$

$$\boldsymbol{\alpha}_{n+1}^{(0)} = (1-\xi_{n+1}^{(0)})\boldsymbol{\alpha}^A + \xi_{n+1}^{(0)}\boldsymbol{\alpha}_{n+1}^{M\,(0)}$$

$$\boldsymbol{\tau}_{n+1}^{(0)} = \boldsymbol{\tau}_n + \mathcal{S}_{n+1}^{-1\,(0)} : (\boldsymbol{D}_{n+1} - \boldsymbol{\alpha}_{n+1}^{(0)}(T_{n+1}-T_n))$$

4.Kuhn-Tucker Condition

Calculate the themoelastic prediction, and evaluate the active set. (α stands for the all the yield surfaces and β stands for the active set)

$$|\Phi_{n+1}^{\alpha\,(0)} = \Phi^\alpha(\boldsymbol{\tau}_{n+1}^{(0)}, T_{n+1}, \kappa_{n+1}^{\alpha\,(0)}; (\boldsymbol{h}_{n+1}^{in\,(0)}))| \le \text{tol}_1 \quad \text{Return to global iteration}$$

$$|\Phi_{n+1}^{\alpha\,(0)} = \Phi^\alpha(\boldsymbol{\tau}_{n+1}^{(0)}, T_{n+1}, \kappa_{n+1}^{\alpha\,(0)}; (\boldsymbol{h}_{n+1}^{in\,(0)}))|_\beta > \text{tol}_1 \quad \text{Active Set, Continue } \mathbf{5}$$

5. Yield Correction

• Discretizing the equations in active set, evolution law and constitutive relation based on the implicit backward Euler integration Section 4.2.3

$$\{\Phi_{n+1}^{\alpha\,(k)} = \Phi^\alpha[\boldsymbol{\tau}_{n+1}^{(k)}, T_{n+1}, \kappa_{n+1}^{\alpha\,(k)}; (\boldsymbol{h}_{n+1}^{in\,(k)})]\}_\beta$$

$$\boldsymbol{R}_{n+1}^{\boldsymbol{h}\,(k)} = -\boldsymbol{h}_{n+1}^{in\,(k)} + \boldsymbol{h}_n^{in} + \sum_{\alpha=1}^{\beta}\boldsymbol{\Lambda}_{n+1}^{\alpha\,(k)}\left(\kappa_{n+1}^{\alpha\,(k)} - \kappa_n^\alpha\right)$$

$$\boldsymbol{R}_{n+1}^{\boldsymbol{\tau}\,(k)} = \mathcal{S}_{n+1}^{(k)} : \boldsymbol{\tau}_{n+1}^{(k)} + \boldsymbol{\alpha}_{n+1}^{(k)}(T_{n+1}-T_n) + \boldsymbol{h}_{n+1}^{in\,(k)} - \boldsymbol{h}_{n+1}$$

IF $|\{\Phi_{n+1}^{\alpha\,(k)}\}_\beta| \le \text{tol}_1, \|\boldsymbol{R}_{n+1}^{\boldsymbol{h}\,(k)}\| \le \text{tol}_2$ and $\|\boldsymbol{R}_{n+1}^{\boldsymbol{\tau}\,(k)}\| \le \text{tol}_2$

Retain the value and GOTO **7**

Else

Continue yield correction

• Solved the system by Newton-Raphson iteraton method Section 4.2.3

$$\mathbb{J}^{(k)} \cdot \Delta\mathbb{X}^{(k)} = \mathbb{B}^{(k)}$$

Where $\mathbb{J}^{(k)}$ is the algorithm Jacobin matrix, obtained by differential the system with respect to the independent

state variables $[\boldsymbol{h}^{in}, \boldsymbol{\tau}, \{\kappa^\alpha\}_\beta]$

$\mathbb{B}^{(k)}$ is the residual

$$\mathbb{B}^{(k)} = [\{-\Phi_{n+1}^{\alpha\,(k)}\}_\beta, -\boldsymbol{R}_{n+1}^{\boldsymbol{h}\,(k)}, -\boldsymbol{R}_{n+1}^{\boldsymbol{\tau}\,(k)}]^T$$

$\Delta\mathbb{X}$ is the solution

$$\Delta\mathbb{X}^{(k)} = [\Delta\boldsymbol{h}_{n+1}^{in\,(k)}, \Delta\boldsymbol{\tau}_{n+1}^{(k)}, \{\Delta\kappa_{n+1}^{\alpha\,(k)}\}_\beta]^T$$

6. Update State Varables

$$\{\kappa_{n+1}^{\alpha\,(k+1)} = \kappa_{n+1}^{\alpha\,(k)} + \Delta\kappa_{n+1}^{\alpha\,(k)}\}_\beta;\ \boldsymbol{h}_{n+1}^{in\,(k+1)} = \boldsymbol{h}_{n+1}^{in\,(k)} + \Delta\boldsymbol{h}_{n+1}^{in\,(k)};\ \boldsymbol{\tau}_{n+1}^{(k+1)} = \boldsymbol{\tau}_{n+1}^{(k)} + \Delta\boldsymbol{\tau}_{n+1}^{(k)}$$

$k = k+1$ Return to **5**

7. Update consistent stiffness matrix

Calculate and update consistent stiffness matrix $\boldsymbol{\mathcal{L}}_{n+1}$ and thermal matrix $\boldsymbol{\Theta}_{n+1}$ (Section4.3)

Exit UMAT and return to global iteration

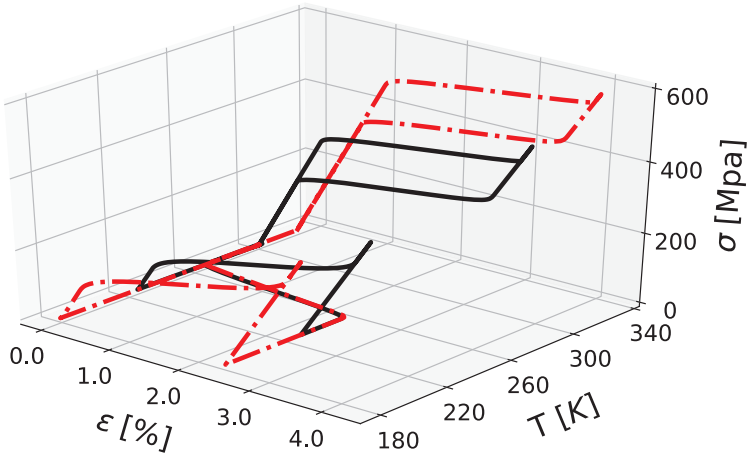

Figure 5.1: Orientation, pseudoelasticity, and shape memory effect under uniaxial thermomechanical loading.The model parameter values adopted in the simulations are given in Table 4

Table 4: Parameter values used for the simulations presented in Fig 5.1

Thermoelastic		Phase Transformation	
parameter	value	parameter	value
E^A [MPa]	37500	H^{max}[%]	2
E^M [MPa]	32500	M_f [K]	220
$\nu^A = \nu^M$	0.33	M_s [K]	248
ρ [g mm^{-3}]	...	A_s [K]	245
$c^A = c^M$ [J g^{-1} K^{-1}]	...	A_f [K]	270
k^A [W mm^{-1} K^{-1}]	...	C_A,C_M [MPa K^{-1}]	7.6, 7.6
k^M [W mm^{-1} K^{-1}]	...	n_1, n_2 ,n_3, n_4	0.12, 0.17 ,0.73, 0.82

(Re)orientation		T/C Asymmetry		Thermal Expansion	
value	parameter	value	parameter	value	parameter
$c^o = c^r$ [MPa K^{-1}]	...	γ, n	0,1.0	α^A [10^{-6}·K^{-1}]	...
$Y^o = Y^r$ [MPa]	10			α_0^M [10^{-6}·K^{-1}]	...
a^o [MPa]	390			α^M [10^{-6}·K^{-1}]	...
n_1^o, n_2^o	0.98,0.32				

to reverse phase transformation (pseudoelasticity). The resulted deformation response is depicted with a solid black line in Figure 5.1. A similar loading path is then followed denoted by the dashed red line in Figure 5.1. The material parameter values used in the simulations are given in Table 4.

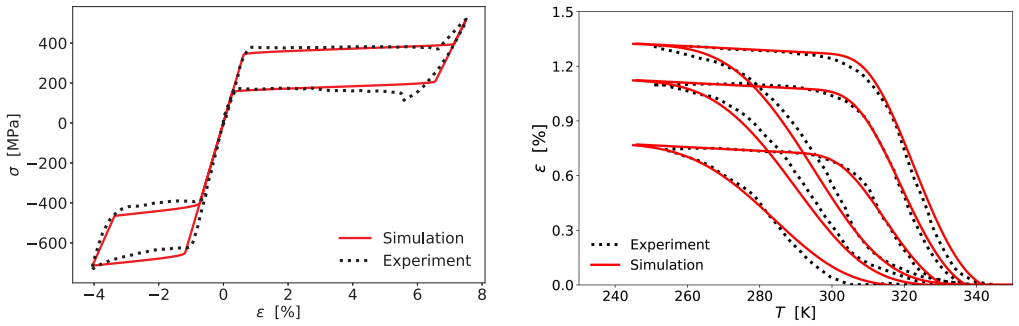

(a) Stress–strain curves resulting from a pseudoelastic loading–unloading cycle in both tension and compression

(b) Strain–temperature curves resulting from isobaric thermal cycles at different bias load levels

Figure 5.2: Simulations compared against experimental results under uniaxial condition

From the plotted deformation response in Figure 5.1, the following capabilities of the model are evident:

(i) the smooth transition from elastic deformation to phase transformation (or orientation)

(ii) the asymmetry between forward and reverse phase transformation

(iii) the dependence of the load level required for phase transformation and orientation

The simulated responses are compared against available experimental data using the calibrated values reported in Tables 5 and 6, respectively. A pseudoelastic loading–unloading cycle in both tension and compression is simulated in Figure 5.2(a), the experimental data are from the experiments performed by [48] and the model parameter values adopted in the simulations are given in Table 5.

A strain–temperature curves resulting from isobaric simulations at different bias stress levels in Figure 5.2(b). The experimental data are reported in [37] and the quantitative material parameters are listed in Table 6. Note that the strain has been adjusted in Figure 5.2(b) so that the difference in the maximum transformation strain reached under each bias load is evident. The model's ability to reproduce (Figure 5.2):

(iv) tension–compression asymmetry

(v) temperature dependence of the hysteresis

(vi) load dependence of maximum transformation strain

Table 5: Parameter values used for the numerical results presented in Figure 5.2a. The simulation is at reference temperature 297 K [48]

Thermoelastic		Phase Transformation	
parameter	value	parameter	value
E^A [MPa]	55000	H^{max}[%]	4.25
E^M [MPa]	32500	M_f [K]	160
$\nu^A = \nu^M$	0.33	M_s [K]	179
ρ [g mm^{-3}]	...	A_s [K]	225
$c^A = c^M$ [J g^{-1} K^{-1}]	...	A_f [K]	245
k^A [W mm^{-1} K^{-1}]	...	C_A,C_M [MPa K^{-1}]	4.2,4.2
k^M [W mm^{-1} K^{-1}]	...	n_1, n_2 ,n_3, n_4	0.4, 0.6 ,0.46, 0.32

(Re)orientation		T/C Asymmetry		Thermal Expansion	
value	parameter	value	parameter	value	parameter
$c^o = c^r$ [MPa K^{-1}]	...	γ, n	2.46,0.5	α^A [10^{-6}·K^{-1}]	...
$Y^o = Y^r$ [MPa]	...			α_0^M [10^{-6}·K^{-1}]	...
a^o [MPa]	...			α^M [10^{-6}·K^{-1}]	...
n_1^o, n_2^o	...				

5.1.2 Minor loops & Latent heat effect

The model's ability to capture minor loops and latent heat effect, *i.e.*, phase-transformation-induced heat generation/absorption, is assessed by uniaxial loading simulations at different loading rates (Figure 5.3). An SMA rectangular bar is clamped on one end and subjected to controlled tensile displacement on the

Table 6: Parameter values used for the numerical results presented in Figure 5.2(b). The material properties of NiTi (55.0 at.%Ni) are calibrated from [37]

Thermoelastic		Phase Transformation	
parameter	value	parameter	value
E^A [MPa]	90000	H^{max}[%]	1.5
E^M [MPa]	63000	M_f [K]	242
$\nu^A = \nu^M$	0.33	M_s [K]	308
ρ [g mm^{-3}]	...	A_s [K]	288
$c^A = c^M$ [J g^{-1} K^{-1}]	...	A_f [K]	342
k^A [W mm^{-1} K^{-1}]	...	C_A,C_M [MPa K^{-1}]	16,10
k^M [W mm^{-1} K^{-1}]	...	n_1, n_2 ,n_3, n_4	0.2, 0.26 ,0.38, 0.21

(Re)orientation		T/C Asymmetry		Thermal Expansion	
value	parameter	value	parameter	value	parameter
$c^o = c^r$ [MPa K^{-1}]	...	γ, n	0,1.0	α^A [10^{-6}·K^{-1}]	...
$Y^o = Y^r$ [MPa]	10			α_0^M [10^{-6}·K^{-1}]	...
a^o [MPa]	390			α^M [10^{-6}·K^{-1}]	...
n_1^o, n_2^o	0.98,0.32				

other end. The mechanical (un)loading is interrupted repeatedly before completion of (reverse) forward phase transformation. The nodes at the ends are kept at a constant temperature throughout the calculations to simulate massive hard grips which act as constant temperature baths. The thermal boundary conditions on the remaining faces correspond to heat flux $\boldsymbol{q}$ due to convection in air of the form $\boldsymbol{q} = h(T - T_s)\boldsymbol{n}$, where h stands for the film coefficient, T_s is the sink temperature, and $\boldsymbol{n}$ is the outward unit normal to the deformed boundary. In the calculations, $h = 12$ W/(m^{2}K), which is standard for air, and $T_s = 300$ K. The thermal conductivity is assumed constant, equal to $k = (k^A + k^M)/2$. In Figure 5.3a, the resulting stress–strain curves for four strain rates equal to $2.5 \cdot 10^{-4}$, $2.5 \cdot 10^{-3}$, $2.5 \cdot 10^{-2}$, and $2.5 \cdot 10^{-1}$ are shown. The hysteresis loops corresponding to the lowest strain rate is very similar to that obtained from the isothermal calculations. The higher the loading rate, the steeper the inelastic response, *i.e.*, the

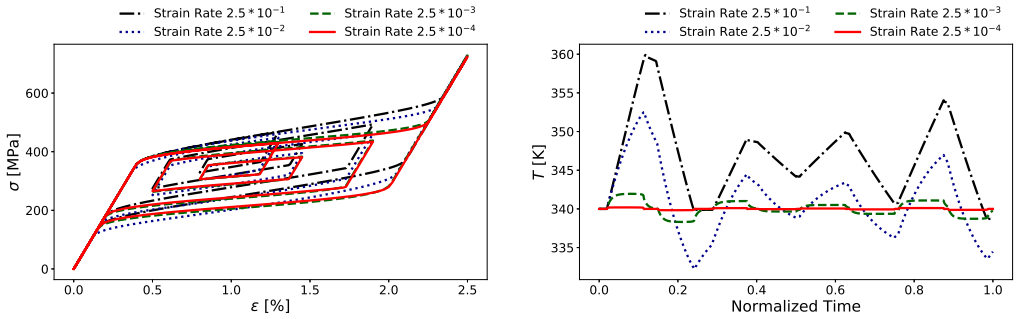

(a) Minor loops for strain rates $2.5 \cdot 10^{-4}$, $2.5 \cdot 10^{-3}$, $2.5 \cdot 10^{-2}$, and $2.5 \cdot 10^{-1}$

(b) Temperature evolution for the simulations depicted in (a)

Figure 5.3: Latent-heat effects on the deformation response. The thermal boundary conditions correspond to heat convection in air. The model parameter values are given in Table 7

Table 7: Parameter values used for the numerical results presented in Figure 5.3

Thermoelastic		Phase Transformation	
parameter	value	parameter	value
E^A [MPa]	90000	H^{max}[%]	1.7
E^M [MPa]	90000	M_f [K]	225
$\nu^A = \nu^M$	0.33	M_s [K]	263
ρ [g mm^{-3}]	0.0065	A_s [K]	275
$c^A = c^M$ [J g^{-1} K^{-1}]	0.48	A_f [K]	310
k^A [W mm^{-1} K^{-1}]	0.0018	C_A,C_M [MPa K^{-1}]	4.2,4.2
k^M [W mm^{-1} K^{-1}]	0.0018	n_1, n_2 ,n_3, n_4	0.3,0.26,0.28,0.31

(Re)orientation		T/C Asymmetry		Thermal Expansion	
value	parameter	value	parameter	value	parameter
$c^o = c^r$ [MPa K^{-1}]	...	γ, n	0,1.0	α^A [10^{-6}·K^{-1}]	...
$Y^o = Y^r$ [MPa]	...			α_0^M [10^{-6}·K^{-1}]	...
a^o [MPa]	...			α^M [10^{-6}·K^{-1}]	...
n_1^o, n_2^o	...				

steeper the slopes of stress–strain curves during transformation/plastic deformation. The resulting response is the outcome of the interplay between the rate of heat generation/absorption during transformation, which influences the load required for phase transformation due to the Clapeyron slopes, and the rate of heat transfer by conduction/convection. During loading, the temperature of the material increases due to heat absorption induced from forward phase transformation despite heat convection in air, which prevails during elastic unloading decreasing the temperature (Figure 5.3b). During reverse phase transformation, the rate of cooling increases due to combined heat convection and transformation-induced heat absorption; it is even possible that the temperature may drop below the ambient temperature depending on the loading rate. It should be noted that the model is not in agreement with the experimental observations of "return points" according to which the minor loops always pass on return through the limiting (σ, ε) points at which the imposed rate of the strain changes its sign.

5.2 Non-Proportional Loading

The aim here is the model's validation against experiments performed on NiTi (50.7 at.% Ni) tubes under non-proportional loading: tension–compression–torsion experiments [35].

In Figure 5.4, the control paths of the simulated experiments are shown that span all four axial/shear strain quadrants resulting in non-proportional loading. Following the notation introduced in [35], $\varepsilon = \varepsilon_{zz}$ stands for the axial strain and $\gamma' = 2\varepsilon_{z\theta}/\sqrt{3}$, where $\varepsilon_{z\theta}$ is the torsional shear strain, on a cylindrical coordinate system. Arrows indicate the loading direction, thus, for example, the box test starts in simple compression, runs in the clockwise direction and ends back at its origin. The numbers characterize points in time (or points in the loading path); respective numbers in the subsequent plots characterize the exact same points.

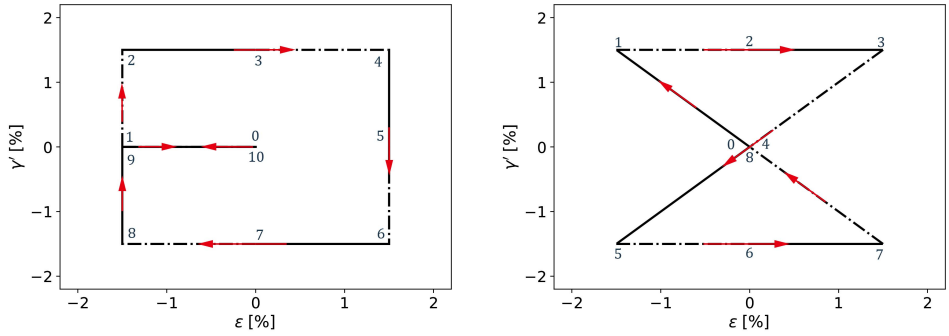

(a) Box loading path

(b) Butterfly loading path

Figure 5.4: Strain–strain diagrams of the controlled loading paths

The butterfly test is substantially different in that the strain space origin is several times traversed and, thus, the overall loading is repeatedly reduced and increased. The maximum strains are $\varepsilon = \gamma' = 0.015$.

The simulation results, based on the calibrated material parameter values given in Table 8, are presented in Figures 5.5, 5.6, and 5.7 and compared with the reported experiment results. Specifically, comparisons are provided for the torsional stress $\tau' = \sqrt{3}\sigma_{z\theta}$ vs axial stress $\sigma = \sigma_{zz}$ responses (Figure 5.5), the torsional stress vs torsional strain responses (Figure 5.6), and the axial stress vs axial strain responses (Figure 5.7). These comparisons demonstrate that the model can capture the response of an SMA subjected to non-proportional loading with a very good accuracy.

In Figure 5.8, the importance of (i) minor loops, (ii) tension–compression asymmetry, and (iii) reorientation in the simulation of the box test is shown (Figures 5.8a, and 5.8b respectively). These figures depict the necessity of an "extended" constitutive model, *i.e.*, a model that incorporates the above referenced

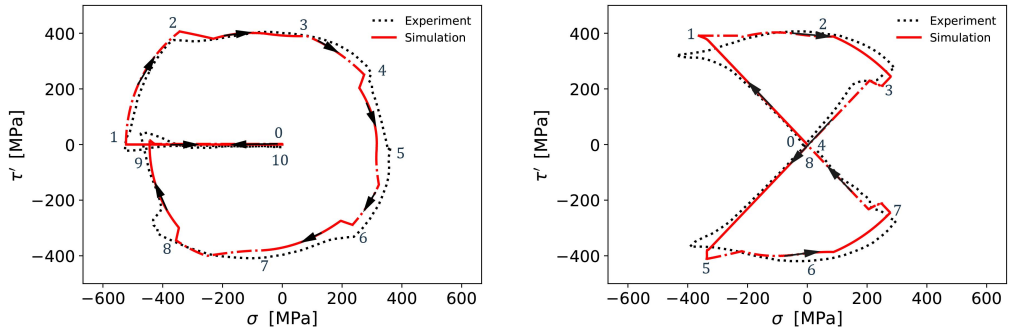

(a) Box test (b) Butterfly test

Figure 5.5: Simulations of the torsional stress vs axial stress responses for the control strain paths shown in Figure 5.4

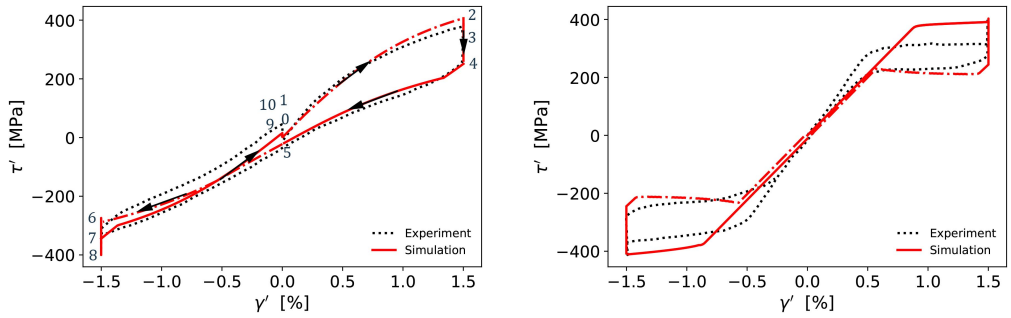

(a) Box test (b) Butterfly test

Figure 5.6: Simulations of the torsional stress vs torsional strain responses for the control strain paths shown in Figure 5.4 ($\tau' = \sqrt{3}\tau$)

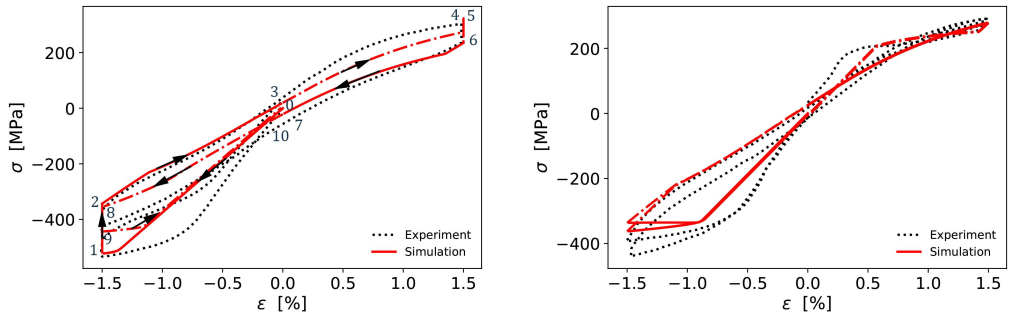

(a) Box test (b) Butterfly test

Figure 5.7: Simulations of the axial stress vs axial strain responses for the control strain paths shown in Figure 5.4

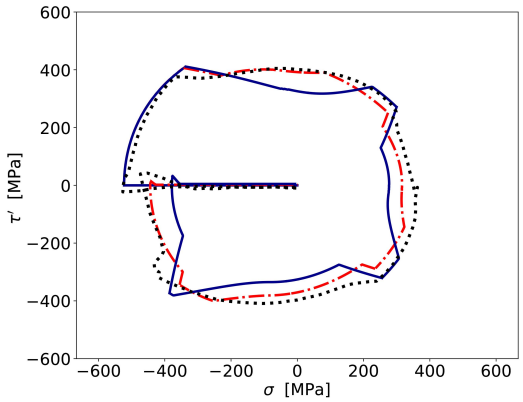

(a) Simulations with and without minor loops.

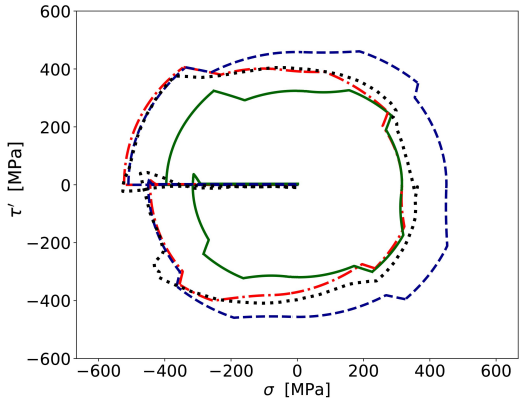

(b) Simulations with and without tension–compression asymmetry (calibration of the model parameters from uniaxial tension or uniaxial compression).

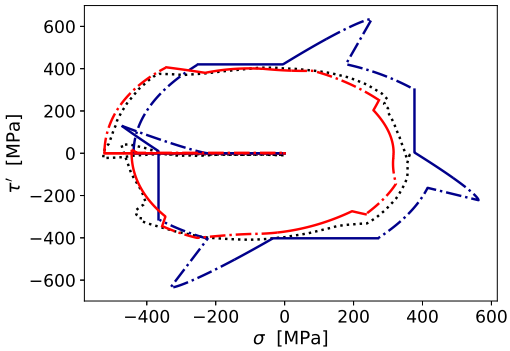

(c) Simulations with and without reorientation.

Figure 5.8: Simulations of the torsional stress vs axial stress response for the box loading path shown Figure 5.4(a). The importance of minor loop, tension-compression asymmetry and reorientation are presented

Table 8: Parameter values used for the numerical results presented in Section 5.2. The calibration of the material parameters included the uniaxial experiments performed by [35]. All simulations are at reference temperature 300K

Thermoelastic		Phase Transformation	
parameter	value	parameter	value
E^A [MPa]	37500	H^{max}[%]	1.6
E^M [MPa]	32500	M_f [K]	178
$\nu^A = \nu^M$	0.33	M_s [K]	198
ρ [g mm^{-3}]	...	A_s [K]	204
$c^A = c^M$ [J g^{-1} K^{-1}]	...	A_f [K]	228
k^A [W mm^{-1} K^{-1}]	...	C_A,C_M [MPa K^{-1}]	4.2,4.2
k^M [W mm^{-1} K^{-1}]	...	n_1, n_2 ,n_3, n_4	0.12, 0.8 ,06, 0.12

(Re)orientation		T/C Asymmetry		Thermal Expansion	
value	parameter	value	parameter	value	parameter
$c^o = c^r$ [MPa K^{-1}]	...	γ, n	1.46,0.6	α^A [10^{-6}·K^{-1}]	...
$Y^o = Y^r$ [MPa]	120			α_0^M [10^{-6}·K^{-1}]	...
a^o [MPa]	...			α^M [10^{-6}·K^{-1}]	...
n_1^o, n_2^o	...				

deformation response characteristics, in capturing the SMAs response under non-proportional loading paths. In Figure 5.8(a), the experimental response (dotted line), full-model simulation (dashed–dotted line), and simulation without accounting for minor loops (solid line) are compared. Partial phase transformation occurs when loading direction is changing, for example, in load step 2-3-4, axial loading is changing from compression to tension with a constant shear loading, and the direction of phase transformation reverses before it completely transform to a certain phase. The results of the solid line indicate the effects of the partial phase transformation during the non-proportional loading. Figure 5.8(b) indicates experimental response (dotted line), full-model simulation (dashed–dotted line), simulations without accounting for tension–compression asymmetry; calibration based on uniaxial tension (solid line) or uniaxial compression (dotted line). Figure 5.8(c) is the experimental response (dotted line), full-model simulation (dashed–dotted line), and simulation without accounting for reorientation

(solid line). Without reorientation assumption, the oriented martensite variants that have already generated by previous loading history will not change their directions when subjected to new loading path, then the predicted direction of transformation strain will not be closely associated with the direction of deviatoric stress and a sudden drop may be resulted during reverse phase transformation based on the proposed model.

5.3 Anisotropic Thermal Expansion Evolution during Deformation Processing

5.3.1 Experimental data, model calibration & validation

The model is calibrated based on the available experimental data on NiTiPd presented in [73]. The calibration of the TE martensite tensor, as described in Section 3.6.2, is depicted in Fig 5.9. A close fit between the experimental data and the expression (3.13) adopted for the dependence of the martensite TE tensor on the volume fraction of oriented martensite, ξ^o, and the unitary orientation tensor, $\mathbf{N}$, is shown under the assumption that the initial microstructure corresponds to self-accommodated martensite. The elastic properties and the orientation related parameters can be calibrated from the experimental stress–strain results presented in Figure 1.14(a) and are listed in Table 9. It is assumed that orientation is completed at 3.56% strain.

A shown in Figure 5.10, the simulated (i) stress–strain response during the loading–unloading cycles (Figure 5.10(a)), (ii) strain–temperature response at zero bias load at the end of every cycle (in the cycle's loading direction) (Figure 5.10(b)), and (iii) evolution of the TE tensor components with cycling (Figure 5.10(c)) adequately approximate the respective experimental results. According to the numerical simulations, the TE response exhibits transverse isotropy since the TE

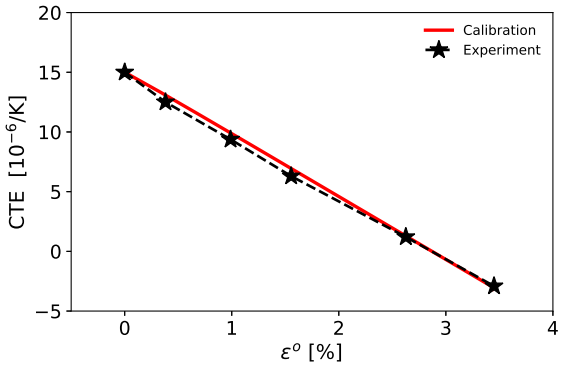

Figure 5.9: Calibration of the martensite TE tensor expression Eqn.(3.13) from experimental data: TE tensor component in the direction reported in Figure 1.14(c)

Table 9: Model parameters calibrated from the experimental data in [73]

Thermoelastic		Phase Transformation	
parameter	value	parameter	value
E^A [MPa]	40000	H^{max}[%]	3.56
E^M [MPa]	37500	M_f [K]	...
$\nu^A = \nu^M$	0.33	M_s [K]	...
ρ [g mm^{-3}]	...	A_s [K]	...
$c^A = c^M$ [J g^{-1} K^{-1}]	...	A_f [K]	...
k^A [W mm^{-1} K^{-1}]	...	C_A,C_M [MPa K^{-1}]	...
k^M [W mm^{-1} K^{-1}]	...	n_1, n_2 ,n_3, n_4	...

(Re)orientation		T/C Asymmetry		Thermal Expansion	
value	parameter	value	parameter	value	parameter
$c^o = c^r$ [MPa K^{-1}]	...	γ, n	0,1.0	α^A [10^{-6}·K^{-1}]	15
$Y^o = Y^r$ [MPa]	150			α_0^M [10^{-6}·K^{-1}]	15
a^o [MPa]	570			α^M [10^{-6}·K^{-1}]	-22.5
n_1^o, n_2^o	0.15,0.95				

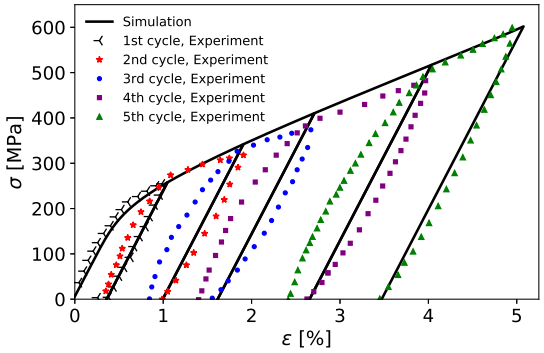

(a) Cyclic stress–strain response

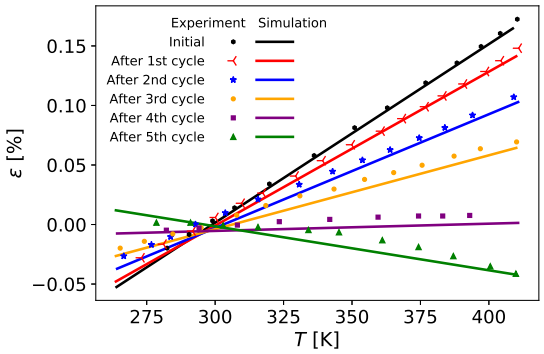

(b) Strain–temperature responses of the undeformed state and after each loading-unloading cycle

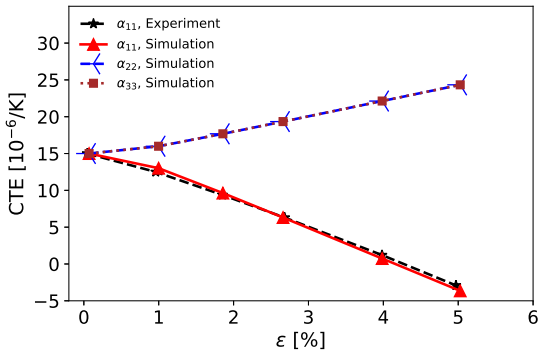

(c) TE tensor components in the loading direction and the transverse directions vs orientation strain

Figure 5.10: Simulated vs experimental NiTiPd response

evolutions curves in the orthogonal directions transverse to the direction of loading coincide (Figure 5.10(c)). The TE tensor components along those directions increase with increasing orientation strain contrarily to the axial TE tensor component which exhibits the opposite dependence. Although, there are no experimental results to verify the predicted response in the transverse directions, it should be noted that it is in accordance with the predictions of the TE response of polycrystalline NiTiPd based on the crystal plasticity-type constitutive model introduced in [126].

5.3.2 Predictions of thermal expansion evolution under uniaxial compressive loading

According to model, the TE tensor components evolution under uniaxial compressive loading beyond the elastic regime is the opposite of that under uniaxial tensile loading; the components in the axial/transverse directions increase/decrease with increasing orientation strain instead of the other way around (Figure 5.11).

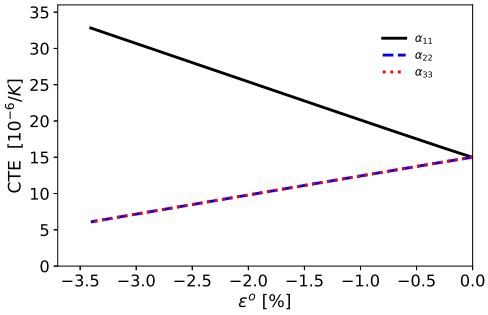

Figure 5.11: Martensite TE tensor components under uniaxial compressive loading vs orientation strain

There are currently no experimental observations to confirm the predicted tendency. However, given (i) the tendency of tensile loading to align in its direction the long axis of the martensite variants vs the tendency of compressive loading to

align in its direction the small axis instead, and (ii) the intrinsic anisotropy of TE tensor of the martensite lattice (Appendix A.2), according to which the TE tensor component along the long axis is negative and that along the short axis positive, the predicted response seems quite plausible. On the basis of the above argument, it is also plausible that there may be a tension–compression asymmetry on the dependence of the TE tensor on martensite variant orientation, which has not been included in the present model for simplicity in the absence of related experimental data.

5.3.3 Model verification

The numerical results presented below are based on the model parameter values listed in Tables 10. The related parameters (Table 10) are not representative of NiTiPd since the experimental results reported in [73] were not sufficient for their calibration.

Table 10: Material parameters used for the simulations presented in Section 5.3.3

Thermoelastic		Phase Transformation	
parameter	value	parameter	value
E^A [MPa]	40000	H^{max}[%]	3.56
E^M [MPa]	37500	M_f [K]	435
$\nu^A = \nu^M$	0.33	M_s [K]	516
ρ [g mm^{-3}]	...	A_s [K]	472
$c^A = c^M$ [J g^{-1} K^{-1}]	...	A_f [K]	538
k^A [W mm^{-1} K^{-1}]	...	C_A,C_M [MPa K^{-1}]	6.5,6.5
k^M [W mm^{-1} K^{-1}]	...	n_1, n_2 ,n_3, n_4	0.6,0.6,0.6,0.6

(Re)orientation		T/C Asymmetry		Thermal Expansion	
value	parameter	value	parameter	value	parameter
$c^o = c^r$ [MPa K^{-1}]	...	γ, n	0,1.0	α^A [10^{-6}·K^{-1}]	15
$Y^o = Y^r$ [MPa]	150			α_0^M [10^{-6}·K^{-1}]	15
a^o [MPa]	570			α^M [10^{-6}·K^{-1}]	-22.5
n_1^o, n_2^o	0.15,0.95				

In Figure 5.12, the stress–strain response and the evolution of the TE tensor

components for an isothermal uniaxial loading–unloading cycle at a temperature at which austenite is stable (above A_f) are shown. Complete forward phase transformation results in fully-oriented martensite and the TE tensor component values at complete transformation are equal to those presented in Figure 5.10(c).

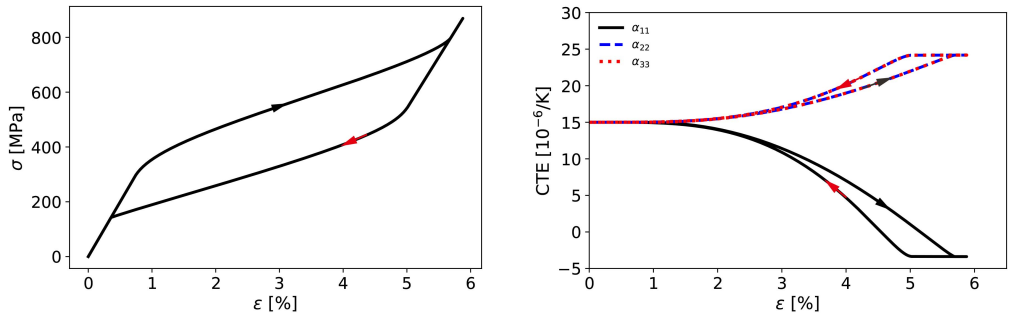

(a) Stress–strain response

(b) TE tensor components vs strain

Figure 5.12: Isothermal uniaxial tensile response at a temperature, $T = 560$K, above the austenite-finish temperature, A_f

In Figure 5.13, the temperature–strain response and TE tensor components evolution are shown for a thermal cycle at different constant bias load levels (isobaric loading) starting from the highest temperature. The range of temperature allows for complete forward and complete reverse phase transformation. For sufficient high bias load levels, forward phase transformation results in fully-oriented martensite and, thus, the TE tensor component values at complete transformation are again equal to those that correspond to complete orientation presented in Figure 5.10(c) and 5.12(b). For lower applied load levels, the TE component values at complete forward phase transformation are dependent on the volume fraction of oriented martensite that can be achieved by the corresponding bias load levels. Note that the dashed lines in Figure 5.13(a) correspond to the temperature–strain responses under the common assumption in literature of an isotropic constant TE martensite tensor, with a coefficient of TE equal to that of self-accommodated

martensite.

The numerical results in Figure 5.15 correspond to the control strain path shown in Figure 5.14 applied to a thin-walled tube, *i.e.*, to a box test spanning all four axial/shear strain quadrants, which results in non-proportional loading and reorientation [35]. Following the notation introduced in [35], $\varepsilon = \varepsilon_{zz}$ stands for the axial strain and $\gamma' = 2\varepsilon_{z\theta}/\sqrt{3}$, where $\varepsilon_{z\theta}$ is the torsional shear strain, on a cylindrical coordinate system. Arrows indicate the loading direction, thus, the box test starts in simple tension, runs in the counterclockwise direction and ends back at its origin. The numbers characterize points in time (or points in the loading path); respective numbers in the subsequent plots characterize the exact same points. The resulting stress–stress curve is depicted in Figure 5.15(a), in which $\sigma = \sigma_{zz}$ is the axial stress and $\tau' = \sqrt{3}\sigma_{z\theta}$, where $\sigma_{z\theta}$ is the torsional shear stress. In Figure 5.15b, the TE tensor components evolutions with respect to time is shown, and in Figure 5.15(c), 5.15(d), and 5.15(e) with respect to the martensite volume fraction, ξ. Note (i) the reorientation induced changes in the TE tensor components' values, *i.e.*, changes induced from the orientation unitary tensor $\mathbf{N}$, which are evident by the changes in those values occurring at constant values of martensite volume fraction, ξ, for example near point 7 in Figure 5.15(c) and 5.15(d), and (ii) the non-zero values of the non-diagonal component $\alpha_{z\theta}$.

5.4 3D Analysis of SMA Devices

In this section, complex 3D simulations of SMAs devices, *i.e.*, of a self-expanding stent, buckling tube and helical spring actuator, are undertaken.

5.4.1 Biomedical SMA self-expanding stent

The good material behavior of SMAs, like psuedoelasticity and shape memory effect, along with its biocompatibility and fatigue properties have made the

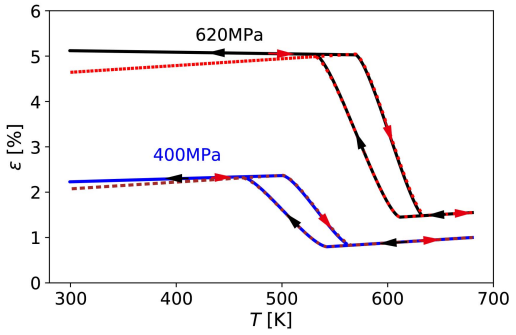

(a) Stress–strain responses. The solid lines correspond to the anisotropic evolving TE martensite tensor proposed in the present model and the dashed lines to the common assumption in literature of an isotropic constant TE martensite tensor with a coefficient of TE equal to that of self-accommodated martensite

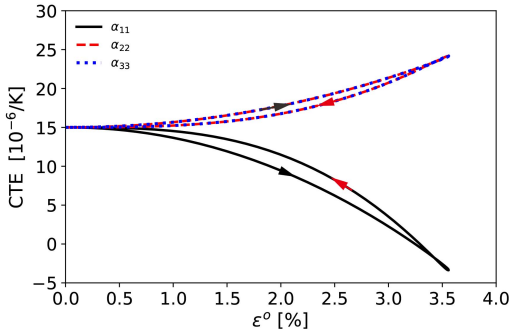

(b) TE tensor components vs strain for tensile bias load resulting in $\sigma = 620$ MPa

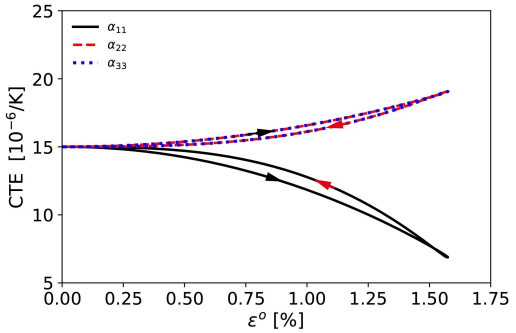

(c) TE tensor components vs strain for tensile bias load resulting in $\sigma = 400$ MPa

Figure 5.13: Isobaric responses under tensile bias load resulting in $\sigma = 400$ MPa and 620 MPa for thermal cycles that ensure complete forward and reverse phase transformation

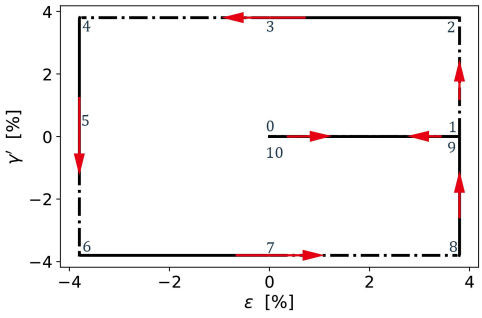

Figure 5.14: Control strain path

material attractive for medical applications. Self-expanding SMAs stent, which is used to treat narrowed arteries in the body, is one of representative application in biomedical (Figure 5.16). Taking advantage of the psuedoelastic property of SMAs, these stents are crimped into a smaller diameter outside the body and inserted into the diseased artery. After being delivered into the desired position, releasing the constraints of the SMAs stent and it will self-expand to its original diameter. Self-expanding stents have proven to reduce the extent of arterial recoil and restenosis as compared to balloon angioplasty procedures and provide a less invasive alternative in the treatment of endovascular disease.

The manufacturing process of SMAs stents starts from a thin tube in which a pattern is micro-machined. The finite element model is built from this machined tube. At first, the stent is expanded to its nominal dimensions, typically at a diameter much larger than the original tube diameter. The stent is then annealed to provide its new unloaded configuration. It is then crimped from the outside and inserted into the delivery system (catheter tube). Once inside the blood vessel, the stent will self-expand when releasing the catheter tube.

The structure used in the simulations is 61.5 mm long, 25.4 mm in outer diameter and 0.5 mm thick in radial direction. The expanded and crimped shape of

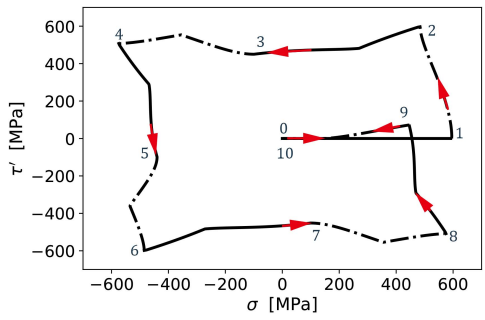

(a) Stress–stress curve

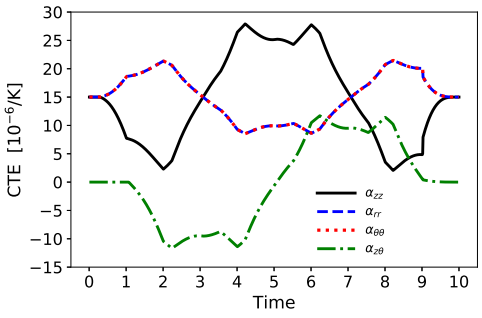

(b) TE tensor evolution

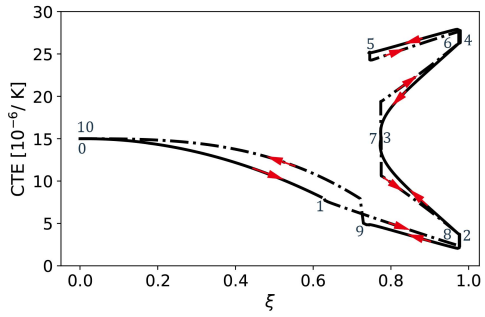

(c) α_{zz} vs ξ

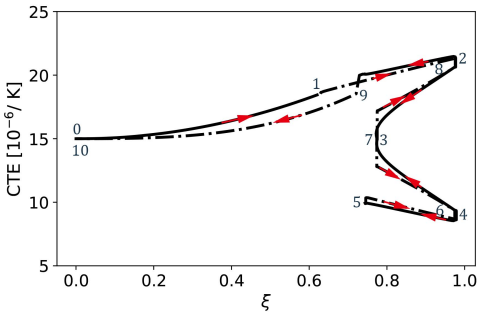

(d) $\alpha_{\theta\theta} = \alpha_{rr}$ vs ξ

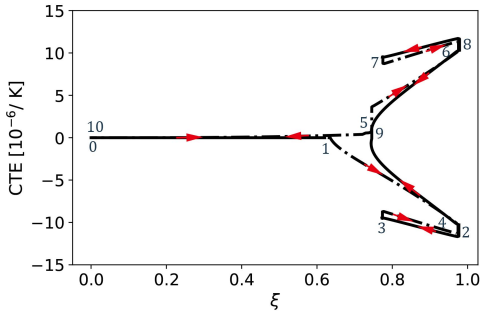

(e) $\alpha_{z\theta}$ vs ξ

Figure 5.15: Simulated response for the control strain path shown in Figure 5.14

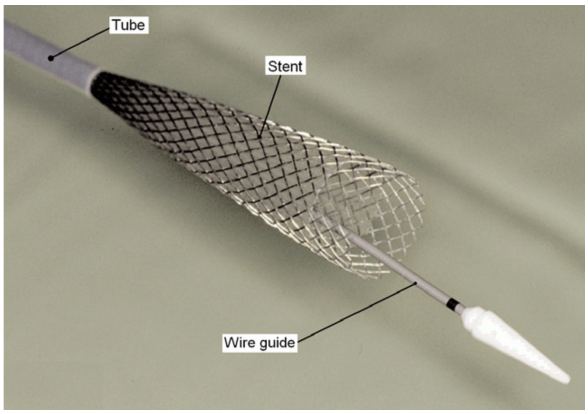

Figure 5.16: Self-expanding NiTi stent

the stent and a unit-cell of the structures are given in Figure 5.17.

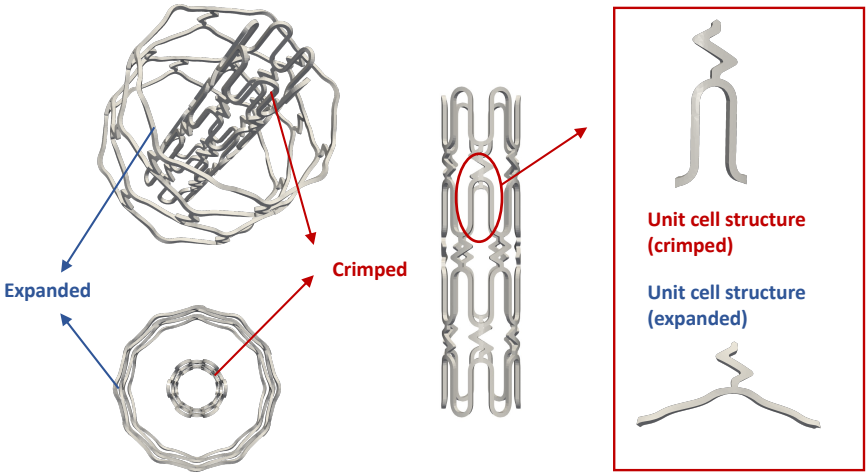

Figure 5.17: Self-expanding NiTi stent geometry and unit-cell model

The material properties of the stent are calibrated in two temperature level, as shown in Figure5.18(a), 293 K as room temperature (crimped stent outside the body) and 310 K as body temperature (self-expanded stent in the body) [8], and the material parameters used in the simulation are listed in Table 11.

Table 11: Parameter values used for the numerical results presented in Section 5.4.1. The calibration of the material parameters included the uniaxial experiments performed by [8]

Thermoelastic		Phase Transformation	
parameter	value	parameter	value
E^A [MPa]	37700	H^{max}[%]	3.5
E^M [MPa]	28500	M_f [K]	175
$\nu^A = \nu^M$	0.33	M_s [K]	190
ρ [g mm^{-3}]	...	A_s [K]	264
$c^A = c^M$ [J g^{-1} K^{-1}]	...	A_f [K]	288
k^A [W mm^{-1} K^{-1}]	...	C_A,C_M [MPa K^{-1}]	11.5,12
k^M [W mm^{-1} K^{-1}]	...	n_1, n_2 ,n_3, n_4	0.6,0.2,0.2,0.3

(Re)orientation		T/C Asymmetry		Thermal Expansion	
value	parameter	value	parameter	value	parameter
$c^o = c^r$ [MPa K^{-1}]	...	γ, n	0,1.0	α^A [10^{-6}·K^{-1}]	...
$Y^o = Y^r$ [MPa]	20			α_0^M [10^{-6}·K^{-1}]	...
a^o [MPa]	120			α^M [10^{-6}·K^{-1}]	...
n_1^o, n_2^o	...				

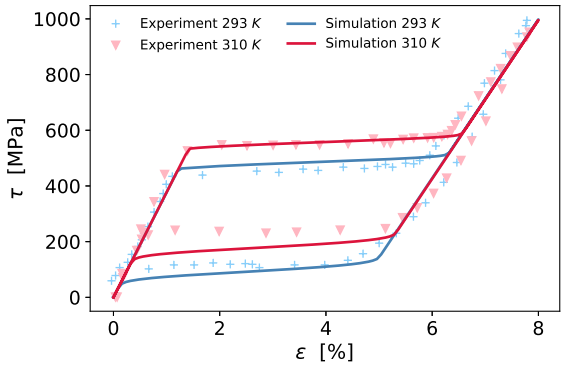

(a) Calibration and experimental validation of the proposed constitutive NiTi model [8], and the calibrated parameters are shown in Table 11

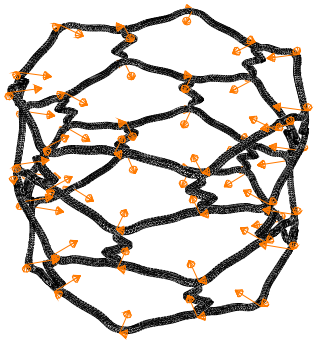

(b) Boundary condition of crimping

Figure 5.18: Material calibration and simulation boundary condition of the SMAs self-expanding stent

Figure 5.18(b) gives the boundary condition for the simulation of the stent

crimping and self-expanding. The loading path adopted by the full-scale 3D SMA stent simulation consists of three steps:

(i) the stent is crimped outside the body at temperature 293 K by applying a uniform cylindrical displacement as shown in Figure 5.18 and attached to a constraint container device called catheter tube;

(ii) the stent is inserted into the body and, thus, the ambient temperature increases from room temperature 293 K to body temperature 310 K;

(iii) the constraint is removed and the stent is allowed to self-expand to its original shape.

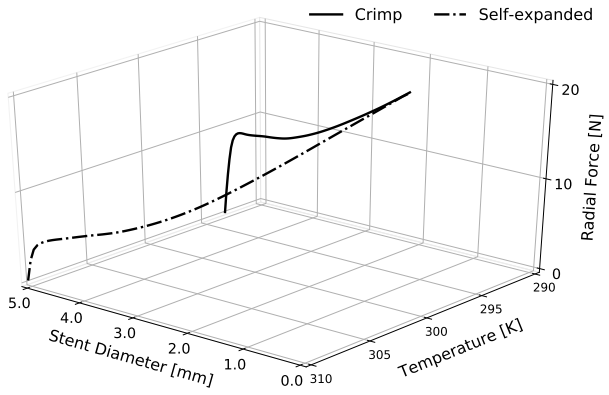

Figure 5.19: Force-diameter-temperature response of SMA stent during crimping and self-expanding

Figure. 5.19 is the total reaction radial force response with respect to the stent diameters and ambient temperatures. The psuedoelasticity properties can be clearly observed when projecting the curve to the force-diameter plane (Figure 5.20 (left)). Since the stent sustains large deformation from crimped configuration to expanded one, finite strain theory plays an important role there. To show how the finite strain theory affects the results, two simulations are performed and compared. One is the proposed finite strain constitutive model based on logarithmic rate and another is based on the infinitesimal strain theory. The radial force response is compared in Figure 5.20, and it is obvious that the finite strain theory

provide more accurate prediction [8].

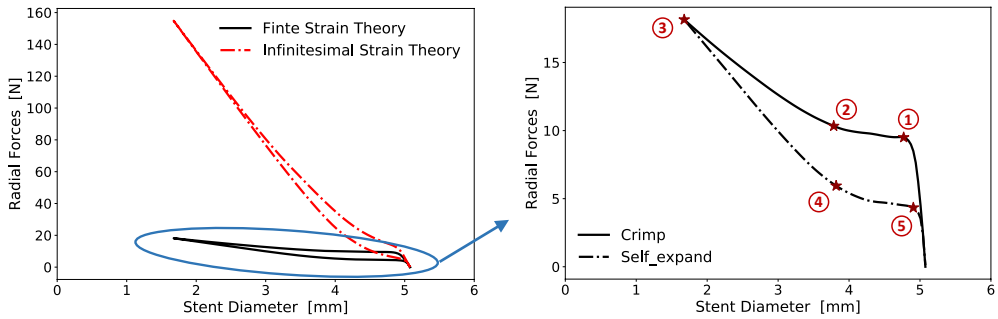

Figure 5.20: Finite strain theory and infinitesimal strain theory are compared on the left figure. The respective points are selected in force-diameter response curve on the right figure and the related evolution of deformed configuration is shown in Figure 5.21

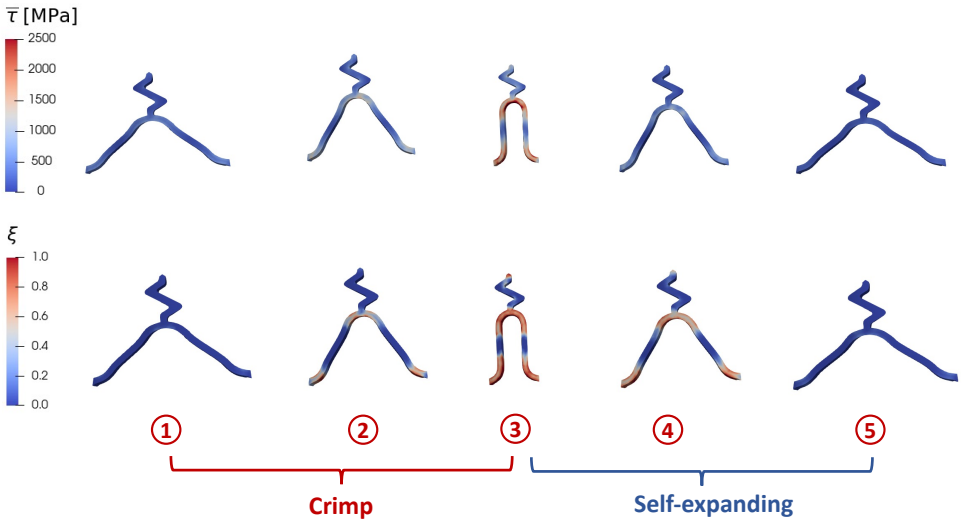

Figure 5.21: Von Mises of Kirchhoff Stress, $\bar{\tau}$, and martensite volume fraction, ξ, distributions in a unit cell at various instances during the simulation. The numerical points are marked in Figure 5.20

We select several representative points (in Figure 5.20(right)) to exhibit the von mises of Kirchhoff stress and martensite volume fraction distribution evolution in a unit cell, and it is shown in Figure 5.21. Stress concentrations evolve at the hinge location, which is subjected to bending, during the crimping process; the initially austenitic material transforms to martensite in the strut curve parts while

the straight strut parts remain in the austenite phase. Once the stent is allowed to self-expand, the martensitic material regions transform back to the austenite phase and the stent assumes its original shape.

5.4.2 SMA tube buckling

The author in [49] recently demonstrated that pseudoelastic NiTi tubes compressed axially buckle and subsequently collapse by progressive development of buckle lobes. On unloading, the material transforms back to austenite, deformation is recovered, and the buckling lobes are erased.

Table 12: Geometry parameters of the SMAs Tube

L (mm)	D (mm)	t (mm)	T (K)
19.62	6.32	0.268	293

The finite element model of the tube is compressed between two rigid plates, and the geometry parameters of the thin-wall tube, the length (L), outer diameter (D), and wall thickness (t), are given in the Table 12. The tube is assigned with initial geometry imperfections and the adopted imperfection mode is given in Figure 5.22(b)(c). The material parameters are calibrated under uniaxial compression as Figure 5.22 (a) at room temperature 293 K. The dotted line is the experimental results and the solid line is the simulation results based on calibrated material parameters given in Table 13.

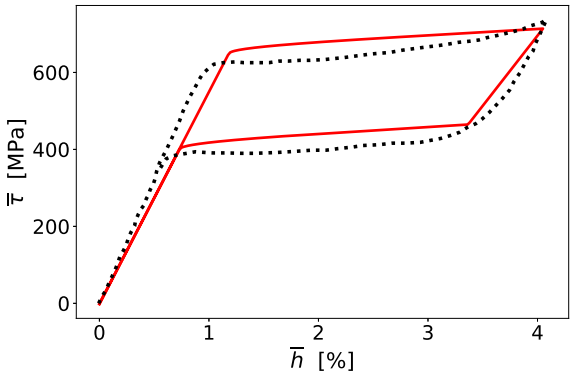

(a) Tube calibration under uniaxial compression at room temperature 293 K [49], and the calibrated material parameters are shown in Table 13

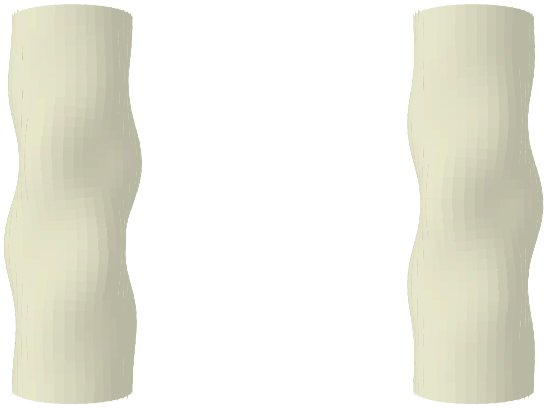

(b) (c)

Figure 5.22: Material calibration and initial geometry imperfection of the tube (amplitudes exaggerated)

Table 13: Parameter values used for the numerical results presented in Section 5.4.2. The calibration of the material parameters under the uniaxial compression at room temperature 293 K [50], as shown in Figure 5.22(a)

Thermoelastic		Phase Transformation	
parameter	value	parameter	value
E^A [MPa]	37500	H^{max}[%]	3.5
E^M [MPa]	32500	M_f [K]	178
$\nu^A = \nu^M$	0.33	M_s [K]	198
ρ [g mm^{-3}]	...	A_s [K]	204
$c^A = c^M$ [J g^{-1} K^{-1}]	...	A_f [K]	228
k^A [W mm^{-1} K^{-1}]	...	C_A,C_M [MPa K^{-1}]	4.2,4.2
k^M [W mm^{-1} K^{-1}]	...	n_1, n_2 ,n_3, n_4	0.12, 0.8 ,0.6, 0.12

(Re)orientation		T/C Asymmetry		Thermal Expansion	
value	parameter	value	parameter	value	parameter
$c^o = c^r$ [MPa K^{-1}]	...	γ, n	0,1.0	α^A [10^{-6}·K^{-1}]	...
$Y^o = Y^r$ [MPa]	20			α_0^M [10^{-6}·K^{-1}]	...
a^o [MPa]	120			α^M [10^{-6}·K^{-1}]	...
n_1^o, n_2^o	...				

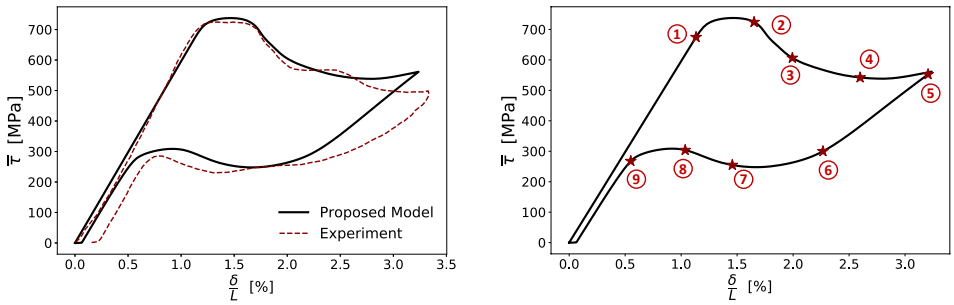

(a) Compressive axial stress-shortening response of SMAs tube buckling.The simulation results are compared with the experimental response

(b) Selected representative points in stress-shortening response, and the related deformed configuration and the distribution of martensite valume fracture ξ are shown in Figure 5.24

Figure 5.23: Stress-shortening response of tube buckling

The loading path of this simulation is relatively simple,

(i) compressing the tube by the two rigid plates to 0.667mm (3.40% shortening),

(ii) releasing the external force, and the tube will recover to its original shape

itself.

The stress-shortening response is demonstrated in Figure 5.23. The simulation results is compared with the experimental one in Figure 5.23(a), and some representative points are selected and numbered in 5.23(b). The corresponding deformed configurations and martensite volume fraction distribution evolution are given in Figure 5.24.

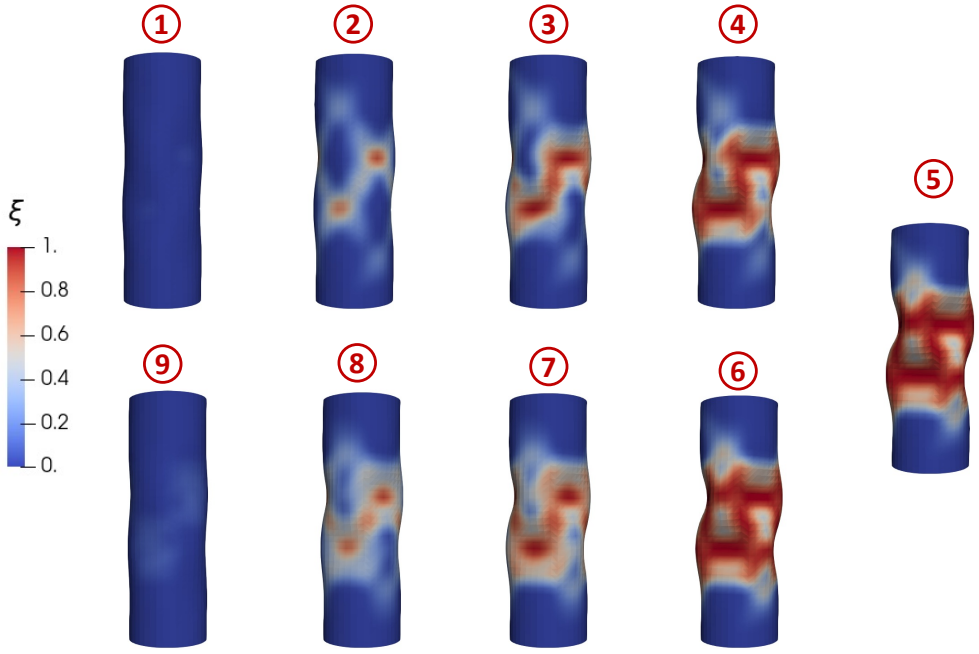

Figure 5.24: Deformed configuration and distributions of martensite volume fraction ξ of the tube buckling and recovering. The images correspond to the numbered bullets on the responses in Figure 5.23 (b)

Attributed to the initial geometry imperfection, the load distribution during buckling is non-proportional and reorientation actives simultaneously with phase transformation. The importance of reorientation is indicated in Figure 5.25.

5.4.3 SMA helical spring actuator

Finally, an SMA helical spring actuator is considered. The response of single free coil with diameter 12.7 mm, wire diameter 0.5 mm, and a pitch size 2.8 mm is

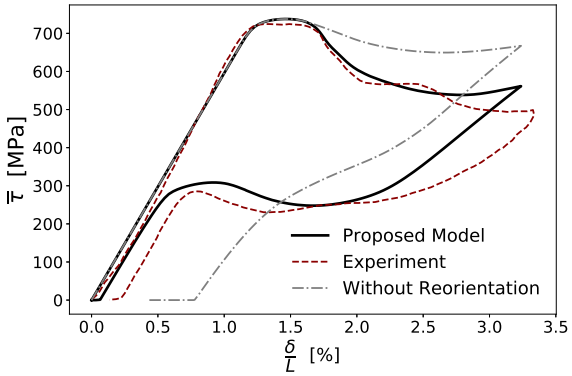

Figure 5.25: Comparison of stress-shortening response with proper martensite variants reorientation and without reorientation

(a) Initial geometry of a coil of the SMA helical spring

(b) Mesh on the end surfaces

Figure 5.26: Coil geometry and mesh

Table 14: Parameter values used for the numerical results presented in [37]

Thermoelastic		Phase Transformation	
parameter	value	parameter	value
E^A [MPa]	90000	H^{max}[%]	1.5
E^M [MPa]	63000	M_f [K]	242
$\nu^A = \nu^M$	0.33	M_s [K]	308
ρ [g mm^{-3}]	...	A_s [K]	288
$c^A = c^M$ [J g^{-1} K^{-1}]	...	A_f [K]	342
k^A [W mm^{-1} K^{-1}]	...	C_A,C_M [MPa K^{-1}]	16,10
k^M [W mm^{-1} K^{-1}]	...	n_1, n_2 ,n_3, n_4	0.2, 0.26 ,0.38, 0.21

(Re)orientation		T/C Asymmetry		Thermal Expansion	
value	parameter	value	parameter	value	parameter
$c^o = c^r$ [MPa K^{-1}]	...	γ, n	0,1.0	α^A [10^{-6}·K^{-1}]	...
$Y^o = Y^r$ [MPa]	10			α_0^M [10^{-6}·K^{-1}]	...
a^o [MPa]	390			α^M [10^{-6}·K^{-1}]	...
n_1^o, n_2^o	0.98,0.32				

simulated (Figure 5.26(a)). The mesh, shown on a spring section in Figure 5.26(b), consists of eight-node brick elements with an aspect ratio equal to 8. The material parameters for the spring are given in Table 14. The following loading path is considered:

(i) a bias load $F = 1.5$ N is applied at the coil ends at $T = 310$ K, and

(ii) the coil is heated to $T = 420$ K maintaining the bias load.

The bias load is applied to reference points of rigid surfaces by imposing tie constraints between the nodes of each of the coil end surfaces and an associated adjacent rigid surface. An additional kinematic constraint is applied to prevent unbounded rotation about coil's axis.

As can be seen in Figure 5.27(a), the application of the load results in a substantial coil elongation, *i.e.*, increase in the axial distance between the two end surfaces, of ~ 35 mm. Note that the results of the finite strain analysis are very different from those of the infinitesimal strain one due to geometric effects captured by the

former analysis, which result in a progressive stiffening of the structure. The local von Mises stress and martensite volume fraction distribution evolutions in the midsection of the coil are presented in Figure 5.27(b). The von Mises stress level and in turn the martensite volume fraction are higher on the surface than the wire center due to local bending.

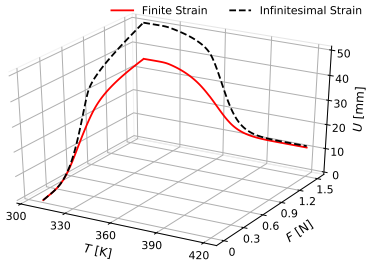

(a) Temperature, T, vs force, F, vs elongation, U

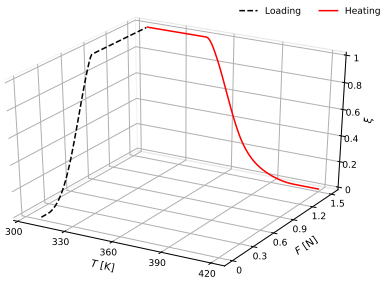

(b) Temperature, T, vs force, F, vs ξ

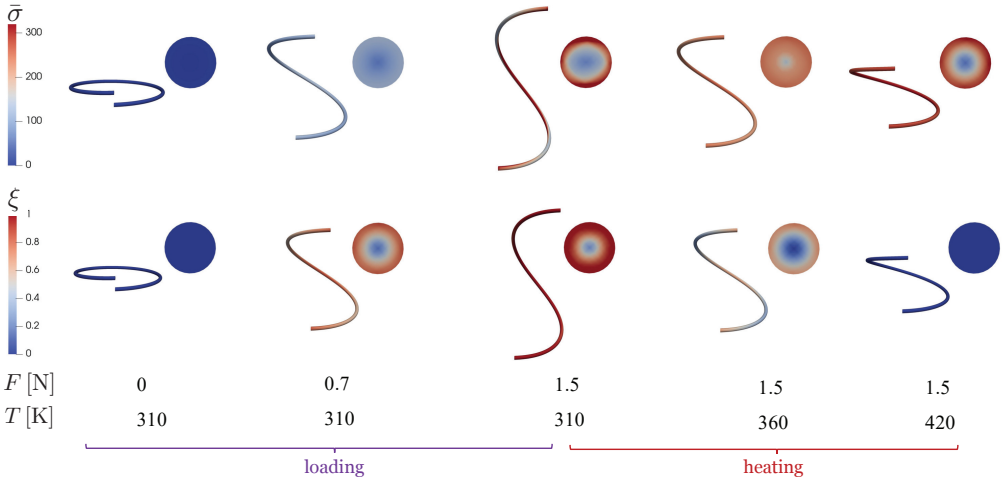

(c) von Mises stress, $\bar{\sigma}$, and martensite volume fraction, ξ, distributions at various instances during the simulation

Figure 5.27: Global and local response of a coil in an SMA helical spring actuator subjected first to mechanical loading that induces phase transformation and then heating while maintaining the load constant. The material parameter values adopted in the simulations are those reported in Table 14

5.5 Summaries of Model Capabilities and Corresponding Validation

A summary of the theoretical contributions, their corresponding model capabilities, and validation efforts are list in Table 15.

Table 15: Summary of the theoretical contributions, model capabilities, and validation efforts

Theoretical Contributions	Model Capabilities	Numerical Validation
Finite Strain Theory		
Eulerian logarithmic strain and the corotational logarithmic objective rate (Section **??**)	•large deformation and rotation response	Section 5.4.1 (Figure 5.20(a)); Section 5.4.3 (Figure 5.27(a))
Framework (Table 1)		
Framework of irreversible thermodynamics	•shape memory effect and pseudoelasticity	Section 5.1.1 (Figure 5.2)
Relying on a set of three independent internal state variables $\{\xi, H, \lambda^r\}$	•co-existence of several phases under multiaxial, non-proportional loading	Section 5.2 (Figure 5.7)
	•temperature and load dependence of the hysteresis width	Section 5.1.1 (Figure 5.1)
	•temperature dependence of the critical force required for (re)orientation	
Yield Surface		
Classical J_2 yield surface with the following modifications:		
Clapeyron slope (Section 3.4.7)	•asymmetry between forward and reverse phase transformation	Section 5.1.1 (Figure 5.2(b))
Minor Loops captured by two major-loop based scalar-values (Section 3.4.6)	•minor loop	Section 5.1.1 (Figure 5.3); Section 5.2 (Figure 5.8(a))
Tension-compression asymmetry based on Lode invariant (Section A.1)	•tension-compression asymmetry	Section 5.1.1 (Figure 5.2(a)); Section 5.2 (Figure 5.8(b))
Thermomechanical Coupling		
Latent heat (Section 3.5)	•rate effects due to latent heat	Section 5.1.1 (Figure 5.3)
Anisotropic TE (Section 3.2)		
Within the aforementioned framework	•TE evolution response under uniaxial loading	Section 5.3 (Figure 5.13, Figure 5.10)
CTE evolution dependenting on matensite variants	•CTE evolution during non-proportional deformation response	Section 5.3.3 (Figure 5.15)
Numerical Implementation		
Closet point projection return mapping algorithm (Table 3)	•a good convergence rate allowing the simulations of complex 3D structures	Section 5.4.1 (Figure 5.21); Section 5.4.2 (Figure 5.23); Section 5.4.3 (Figure 5.27)

6 CONCLUSIONS

A constitutive model for the thermomechanical deformation response of shape memory alloys (SMAs) is proposed, which can efficiently describe the material response under non-proportional thermomechanical loading and tailoring the evolution of thermal expansion (TE) tensor during deformation.

The model accounts for pseudoelasticity, shape memory effect, reorientation of martensite variants, minor loops, tension–compression asymmetry, and latent-heat-induced rate effects in a finite strain description. Although most of the aforementioned aspects of martensitic transformation can be adequately described by different models in literature, each of which accounts for a number of those, the strength of the proposed model lies in its ability to account for all in a fairly simple manner by introducing a set of three independent internal state variables. These internal variables, the martensite volume fraction, the magnitude and the direction of the inelastic strain, allow for an implicit definition of the volume fraction of oriented vs self-accommodated martensite. The model further accounts for temperature and load dependence of the hysteresis width, asymmetry between forward and reverse phase transformation, smooth thermomechanical response, and can address the deformation response in the concurrent presence of several phases, *i.e.*, when austenite, self-accommodated and oriented martensite co-exist in the microstructure. Moreover, the model accounts for temperature dependence of the critical force required for (re)orientation, which is largely neglected in the models proposed in the literature. The model's ability to reproduce all the above characteristics of martensitic transformation and the efficiency of the numerical scheme employed for the model integration has been demonstrated by comparison of simulations with available experimental data. The model is able to capture

in good accord the deformation response of SMAs observed in complex experiments, such as tension/compression/torsion experiments. The proposed model is also validated against recent experiments on tailoring TE through martensite orientation in a NiTiPd high temperature SMA. In those experiments, the TE tensor component in the loading direction of NiTiPd in the martensite state was shown to decrease with increasing inelastic strain induced by uniaxial tensile loading. According to the model, the TE tensor components in the transverse to the loading directions decrease with increasing tensile inelastic strain. The TE tensor components' dependence on inelastic strain is predicted to be reversed for compressive uniaxial loading. In the absence of related experimental observations, the model does not account for possible tension–compression asymmetry in the TE response for simplicity. The efficiency of the numerical implementation is verified with simulations of SMA devices, such as a biomedical stent and a spring actuator, as well as buckling of an SMA tube.

References

[1] Ahadi, A., Matsushita, Y., Sawaguchi, T., Sun, Q., and Tsuchiya, K. Origin of zero and negative thermal expansion in severely-deformed superelastic niti alloy. *Acta Materialia 124* (2017), 79 – 92.

[2] Arghavani, J., Auricchio, F., and Naghdabadi, R. A finite strain kinematic hardening constitutive model based on hencky strain: general framework, solution algorithm and application to shape memory alloys. *International Journal of Plasticity 27*, 6 (2011), 940–961.

[3] Arghavani, J., Auricchio, F., Naghdabadi, R., Reali, A., and Sohrabpour, S. A 3-D phenomenological constitutive model for shape memory alloys under multiaxial loadings. *International Journal of Plasticity 26*, 7 (2010), 976–991.

[4] Auricchio, F., Bonetti, E., Scalet, G., and Ubertini, F. Theoretical and numerical modeling of shape memory alloys accounting for multiple phase transformations and martensite reorientation. *International Journal of Plasticity 59* (2014), 30–54.

[5] Auricchio, F., Bonetti, E., Scalet, G., and Ubertini, F. Theoretical and numerical modeling of shape memory alloys accounting for multiple phase transformations and martensite reorientation. *International Journal of Plasticity 59* (2014), 30–54.

[6] Auricchio, F., and Petrini, L. A three-dimensional model describing stress-temperature induced solid phase transformations: solution algorithm and boundary value problems. *International Journal for Numerical Methods in Engineering 61*, 6 (2004), 807–836.

[7] Auricchio, F., and Sacco, E. Thermo-mechanical modelling of a superelastic shape-memory wire under cyclic stretching–bending loadings. *International Journal of Solids and Structures 38*, 34-35 (2001), 6123–6145.

[8] Azaouzi, M., Makradi, A., and Belouettar, S. Deployment of a self-expanding stent inside an artery: a finite element analysis. *Materials & Design 41* (2012), 410–420.

[9] Bo, Z., and , D. C. Thermomechanical modeling of polycrystalline SMAs under cyclic loading, Part IV: Modeling of minor hysteresis loops. *International Journal of Engineering Science 37*, 9 (1999), 1205–1249.

[10] Bruhns, O., Xiao, H., and Meyers, A. Self-consistent eulerian rate type elasto-plasticity models based upon the logarithmic stress rate. *International Journal of Plasticity 15*, 5 (1999), 479–520.

[11] Bruhns, O., Xiao, H., and Meyers, A. Large simple shear and torsion problems in kinematic hardening elasto-plasticity with logarithmic rate. *International journal of solids and structures 38*, 48-49 (2001), 8701–8722.

[12] Bruhns, O., Xiao, H., and Meyers, A. A self-consistent eulerian rate type

model for finite deformation elastoplasticity with isotropic damage. *International Journal of Solids and Structures 38*, 4 (2001), 657–683.

[13] Bunget, G., and Seelecke, S. Actuator placement for a bio-inspired bone-joint system based on sma. In *Active and Passive Smart Structures and Integrated Systems 2009* (2009), vol. 7288, International Society for Optics and Photonics, p. 72880L.

[14] Calhoun, C., Wheeler, R., Baxevanis, T., and , D. Actuation fatigue life prediction of shape memory alloys under the constant-stress loading condition. *Scripta Materialia 95* (2015), 58–61.

[15] Chatziathanasiou, D., Chemisky, Y., Chatzigeorgiou, G., and Meraghni, F. Modeling of coupled phase transformation and reorientation in shape memory alloys under non-proportional thermomechanical loading. *International Journal of Plasticity 82* (2016), 192–224.

[16] Chemisky, Y., Duval, A., Patoor, E., and Zineb, T. B. Constitutive model for shape memory alloys including phase transformation, martensitic reorientation and twins accommodation. *Mechanics of Materials 43*, 7 (2011), 361–376.

[17] Chowdhury, P., Patriarca, L., Ren, G., and Sehitoglu, H. Molecular dynamics modeling of NiTi superelasticity in presence of nanoprecipitates. *International Journal of Plasticity 81* (2016), 152–167.

[18] Chowdhury, P., Ren, G., and Sehitoglu, H. Niti superelasticity via atomistic simulations. *Philosophical Magazine Letters 95*, 12 (2015), 574–586.

[19] Christ, D., and Reese, S. A finite element model for shape memory alloys considering thermomechanical couplings at large strains. *International Journal of Solids and Structures 46*, 20 (2009), 3694–3709.

[20] Chrysochoos, A., Lobel, M., and Maisonneuve, O. Thermomechanical coupling of pseudoelastic behavior of cuznal and niti alloys. *Comptes Rendus De L Academie des sciences serie II 320*, 5 (1995), 217–223.

[21] Chumljakov, J., and Starenchenko, S. Stress induced martensitic transformation in aged Titanium Nickel single crystals. *Journal de Physique IV 5*, C8 (1995), C8–803.

[22] Cisse, C., Zaki, W., and Zineb, T. B. A review of modeling techniques for advanced effects in shape memory alloy behavior. *Smart Materials and Structures 25*, 10 (2016), 103001.

[23] Colorado, J., Barrientos, A., Rossi, C., and Breuer, K. S. Biomechanics of smart wings in a bat robot: morphing wings using sma actuators. *Bioinspiration & biomimetics 7*, 3 (2012), 036006.

[24] Darijani, H., and Naghdabadi, R. Hyperelastic materials behavior modeling using consistent strain energy density functions. *Acta Mechanica 213*, 3-4 (2010), 235–254.

[25] Dhala, S., Mishra, S., Tewari, A., and Alankar, A. Modeling of finite deformation of pseudoelastic NiTi shape memory alloy considering various inelasticity mechanisms. *International Journal of Plasticity 115* (2019), 216–237.

[26] Dutta, S. M., and Ghorbel, F. H. Differential hysteresis modeling of a shape memory alloy wire actuator. *IEEE/ASME Transactions on Mechatronics 10*, 2 (2005), 189–197.

[27] Evangelista, V., Marfia, S., and Sacco, E. Phenomenological 3D and 1D consistent models for shape-memory alloy materials. *Computational Mechanics 44*, 3 (2009), 405.

[28] Eyres, D., and Bruce, G. 23 - liquefied gas carriers. In *Ship Construction (Seventh Edition)*, D. Eyres and G. Bruce, Eds., seventh edition ed. Butterworth-Heinemann, Oxford, 2012, pp. 279 –289.

[29] Feng, Y., Rabbath, C. A., and Su, C.-Y. Inverse Duhem model based robust adaptive control for flap positioning system with SMA actuators. *IFAC Proceedings Volumes 44*, 1 (2011), 8126–8131.

[30] Furst, S. J., Bunget, G., and Seelecke, S. Design and fabrication of a bat-inspired flapping-flight platform using shape memory alloy muscles and joints. *Smart Materials and Structures 22*, 1 (2012), 014011.

[31] Gall, K., Juntunen, K., Maier, H., Sehitoglu, H., and Chumlyakov, Y. I. Instrumented micro-indentation of niti shape-memory alloys. *Acta Materialia 49*, 16 (2001), 3205–3217.

[32] Gall, K., Sehitoglu, H., Chumlyakov, Y. I., and Kireeva, I. Tension–compression asymmetry of the stress–strain response in aged single crystal and polycrystalline niti. *Acta Materialia 47*, 4 (1999), 1203–1217.

[33] Gall, K., and Shehitoglu, H. The role of texture in tension-compression asymmetry in polycrstyalline NiTi. *International Journal of Plasticity 15* (1999), 69–92.

[34] Gehring, D., Monroe, J. A., and Karaman, I. Effects of composition on the mechanical properties and negative thermal expansion in martensitic tinb alloys. *Scripta Materialia 178* (2020), 351–355.

[35] Grabe, C., and Bruhns, O. Path dependence and multiaxial behavior of a polycrystalline NiTi alloy within the pseudoelastic and pseudoplastic temperature regimes. *International Journal of Plasticity 25*, 3 (2009), 513–545.

[36] Gurtin, M. E., Fried, E., and Anand, L. *The mechanics and thermodynamics of continua*. Cambridge University Press, 2010.

[37] Hartl, D., Mooney, J., Lagoudas, D., Calkins, F., and Mabe, J. Use of a Ni60Ti shape memory alloy for active jet engine chevron application: II. experimentally validated numerical analysis. *Smart Materials and Structures 19*, 1 (2009), 015021.

[38] He, Y., and Sun, Q. Rate-dependent domain spacing in a stretched NiTi strip. *International Journal of Solids and Structures 47*, 20 (2010), 2775–2783.

[39] He, Y., and Sun, Q. On non-monotonic rate dependence of stress hysteresis of superelastic shape memory alloy bars. *International Journal of Solids and Structures 48*, 11–12 (2011), 1688–1695.

[40] He, Y., Yin, H., Zhou, R., and Sun, Q. Ambient effect on damping peak of NiTi shape memory alloy. *Materials Letters 64*, 13 (2010), 1483–1486.

[41] Helm, D., and Haupt, P. Thermomechanical behavior of shape memory alloys. In *Smart Structures and Materials 2001: Active Materials: Behavior and Mechanics* (2001), vol. 4333, International Society for Optics and Photonics, pp. 302–313.

[42] Helm, D., and Haupt, P. Shape memory behaviour: modelling within continuum thermomechanics. *International Journal of Solids and Structures 40*, 4 (2003), 827–849.

[43] Hill, R. Aspects of invariance in solid mechanics. In *Advances in applied mechanics*, vol. 18. Elsevier, 1979, pp. 1–75.

[44] Hossain, M., and Baxevanis, T. A finite strain thermomechanically-coupled constitutive model for phase transformation and (transformation-induced) plastic deformation in NiTi single crystals. *International Journal of Plasticity 139* (2021), 102957.

[45] Jacobus, K., Sehitoglu, H., and Balzer, M. Effect of stress state on the stress-induced martensitic transformation in polycrystalline Ni-Ti alloy. *Metallurgical and Materials Transactions A 27*, 10 (1996), 3066–3073.

[46] Jacquot, P. M., Lehmann, M., and de Lega, X. C. Deformation analysis of a communication telescope structure under nonuniform heating using holographic interferometry. In *Practical Holography XII* (1998), S. A. Benton, Ed., vol. 3293, International Society for Optics and Photonics, SPIE, pp. 102 – 113.

[47] Jani, J. M., Leary, M., Subic, A., and Gibson, M. A. A review of shape memory alloy research, applications and opportunities. *Materials & Design (1980-2015) 56* (2014), 1078–1113.

[48] Jiang, D., Kyriakides, S., Bechle, N. J., and Landis, C. M. Bending of pseudoelastic NiTi tubes. *International Journal of Solids and Structures 124* (2017), 192–214.

[49] Jiang, D., and Landis, C. M. A constitutive model for isothermal pseudoelasticity coupled with plasticity. *Shape Memory and Superelasticity 2*, 4 (2016), 360–370.

[50] Jiang, D., Landis, C. M., and Kyriakides, S. Effects of tension/compression asymmetry on the buckling and recovery of niti tubes under axial compression. *International Journal of Solids and Structures 100* (2016), 41–53.

[51] Junker, P., Jaeger, S., Kastner, O., Eggeler, G., and Hackl, K. Variational prediction of the mechanical behavior of shape memory alloys based on thermal experiments. *Journal of the Mechanics and Physics of Solids 80* (2015), 86–102.

[52] Karakalas, A., Machairas, T., Solomou, A., and Saravanos, D. A. Modeling of partial transformation cycles of SMAs with a modified hardening function. *Smart Materials and Structures* (2019).

[53] Karakalas, A. A., Machairas, T. T., and Saravanos, D. A. Effect of shape memory alloys partial transformation on the response of morphing structures encompassing shape memory alloy wire actuators. *Journal of Intelligent Material Systems and Structures 30*, 11 (2019), 1682–1698.

[54] Kinsey, J. C., and Whitcomb, L. L. Adaptive identification on the group of rigid body rotations. In *Proceedings of the 2005 IEEE international conference on robotics and automation* (2005), IEEE, pp. 3256–3261.

[55] Lagoudas, D., Ed. *Shape Memory Alloys: Modelling and Enginnering Applications*. Springer, New-York, 2008.

[56] Lagoudas, D., and Bo, Z. Thermomechanical modeling of polycrystalline SMAs under cyclic loading, Part II: Material characterization and experimental results for a stable transformation cycle. *International Journal of Engineering Science 37*, 9 (1999), 1141–1173.

[57] Lagoudas, D., Entchev, P., Popov, P., Patoor, E., Brinson, L., and Gao, X. Shape memory alloys. Part II: Modeling of polycrystals. *Mechanics of Materials 38* (2006), 430–462.

[58] Lagoudas, D., Hartl, D., Chemisky, Y., Machado, L., and Popov, P. Constitutive model for the numerical analysis of phase transformation in polycrystalline shape memory alloys. *International Journal of Plasticity 32* (2012), 155–183.

[59] Lagoudas, D. C., Entchev, P. B., Popov, P., Patoor, E., Brinson, L. C., and Gao, X. Shape memory alloys, part ii: Modeling of polycrystals. *Mechanics of Materials 38*, 5-6 (2006), 430–462.

[60] Levitas, V., and Preston, D. Three-dimensional Landau theory for multivariant stress-induced martensitic phase transformations. II. Multivariant phase transformations and stress space analysis. *Physical review B 66* (2002), 134207.

[61] Lim, J. T., and McDowell, D. L. Mechanical behavior of a Ni-Ti shape memory alloy under axial-torsional proportional and nonproportional loading. *Journal of Engineering Materials and Technology 121* (1999), 9–18.

[62] Lim, T., and McDowell, D. Cyclic thermomechanical behavior of a polycrystalline pseudoelastic shape memory alloy. *Journal of the Mechanics and Physics of Solids 50*, 3 (2002), 651–676.

[63] Lim, T. J., and McDowell, D. L. Mechanical behavior of an ni-ti shape memory alloy under axial-torsional proportional and nonproportional loading.

[64] Lloyd, L. T., and Barrett, C. Thermal expansion of alpha uranium. *Journal of Nuclear Materials 18*, 1 (1966), 55 – 59.

[65] Lobo, P. S., Almeida, J., and Guerreiro, L. Recentring and control of peak displacements of a RC frame using damping devices. *Soil Dynamics and Earthquake Engineering 94* (2017), 66–74.

[66] Loh, C. S., Yokoi, H., and Arai, T. New shape memory alloy actuator: design and application in the prosthetic hand. In *2005 IEEE Engineering in Medicine and Biology 27th Annual Conference* (2006), IEEE, pp. 6900–6903.

[67] Machairas, T., Solomou, A., and Saravanos, D. A morphing chevron actuated by shape memory alloy wires for noise reduction. In *las actas, proceedings, de 3AF/CEAS Conference Greener Aviation: Clean Sky Breakthroughs and Worldwide Status* (2014).

[68] Matsuzaki, Y., Funami, K., and Naito, H. Inner loops of pseudoelastic hysteresis of shape memory alloys: Preisach approach. In *Smart Structures and Materials 2002: Active Materials: Behavior and Mechanics* (2002), vol. 4699, International Society for Optics and Photonics, pp. 355–364.

[69] Mayergoyz, I. D. *Mathematical models of hysteresis*. Springer Science & Business Media, 2012.

[70] Meyers, A., Xiao, H., and Bruhns, O. Elastic stress ratchetting and corotational stress rates. *Technische Mechanik-European Journal of Engineering Mechanics 23*, 2-4 (2003), 92–102.

[71] Meyers, A., Xiao, H., and Bruhns, O. Choice of objective rate in single parameter hypoelastic deformation cycles. *Computers & structures 84*, 17-18 (2006), 1134–1140.

[72] Moler, C., and Van Loan, C. Nineteen dubious ways to compute the exponential of a matrix, twenty-five years later. *SIAM review 45*, 1 (2003), 3–49.

[73] Monroe, J., Gehring, D., Karaman, I., Arroyave, R., Brown, D., and Clausen, B. Tailored thermal expansion alloys. *Acta Materialia 102* (2016), 333 – 341.

[74] Morin, C., Moumni, Z., and Zaki, W. A constitutive model for shape memory alloys accounting for thermomechanical coupling. *International Journal of Plasticity 27*, 5 (2011), 748–767.

[75] Morin, C., Moumni, Z., and Zaki, W. Thermomechanical coupling in shape memory alloys under cyclic loadings: Experimental analysis and constitutive modeling. *International Journal of Plasticity 27*, 12 (2011), 1959–1980.

[76] Müller, C., and Bruhns, O. A thermodynamic finite-strain model for pseudoelastic shape memory alloys. *International Journal of Plasticity 22*, 9 (2006), 1658–1682.

[77] Müller, I., and Xu, H. On the pseudo-elastic hysteresis. *Acta metallurgica et materialia 39*, 3 (1991), 263–271.

[78] Nakshatrala, K. B. Notes on the exponential of a matrix.

[79] Oehler, S., Hartl, D., Lopez, R., Malak, R., and , D. Design optimization and uncertainty analysis of sma morphing structures. *Smart Materials and Structures 21*, 9 (2012), 094016.

[80] Ogden, R. W. *Non-linear elastic deformations*. Courier Corporation, 1997.

[81] Paranjape, H. M., Manchiraju, S., and Anderson, P. M. A phase field–Finite element approach to model the interaction between phase transformations and plasticity in shape memory alloys. *International Journal of Plasticity 80* (2016), 1–18.

[82] Patoor, E., El Amrani, M., Eberhardt, A., and Berveiller, M. Determination of the origin for the dissymmetry observed between tensile and compression tests on shape memory alloys. *Le Journal de Physique IV 5*, C2 (1995), C2–495.

[83] Patoor, E., Lagoudas, D. C., Entchev, P. B., Brinson, L. C., and Gao, X. Shape memory alloys, Part I: General properties and modeling of single crystals. *Mechanics of Materials 38*, 5–6 (2006), 391–429.

[84] Popov, P., and Lagoudas, D. C. A 3-D constitutive model for shape memory alloys incorporating pseudoelasticity and detwinning of self-accommodated martensite. *International Journal of Plasticity 23*, 10 – 11 (2007), 1679 – 1720.

[85] Prahlad, H., and Chopra, I. Development of a strain-rate dependent model for uniaxial loading of SMA wires. *Journal of Intelligent Material Systems and Structures 14*, 14 (2003), 429–442.

[86] Rajagopal, K., and Srinivasa, A. Mechanics of the inelastic behavior of materials—part 1, theoretical underpinnings. *International Journal of Plasticity 14*, 10-11 (1998), 945–967.

[87] Raniecki, B., and Mróz, Z. Yield or martensitic phase transformation conditions and dissipation functions for isotropic, pressure-insensitive alloys exhibiting SD effect. *Acta Mechanica 195*, 1–4 (2008), 81–102.

[88] Rao, A., Ruimi, A., and Srinivasa, A. R. Internal loops in superelastic shape memory alloy wires under torsion–experiments and simulations/predictions. *International Journal of Solids and Structures 51*, 25-26 (2014), 4554–4571.

[89] Reinhardt, W., and Dubey, R. Eulerian strain-rate as a rate of logarithmic strain. *Mechanics Research Communications 22*, 2 (1995), 165–170.

[90] Savi, M., and Paiva, A. Describing internal subloops due to incomplete phase transformations in shape memory alloys. *Archive of Applied Mechanics 74*, 9 (2005), 637–647.

[91] Scalet, G., Karakalas, A., Xu, L., and , D. Finite strain constitutive modelling of shape memory alloys considering partial phase transformation with transformation-induced plasticity. *Shape Memory and Superelasticity* (2021), 1–16.

[92] Sedlak, P., Frost, M., Benešová, B., Zineb, T. B., and Šittner, P. Thermomechanical model for niti-based shape memory alloys including r-phase

and material anisotropy under multi-axial loadings. *International Journal of Plasticity 39* (2012), 132–151.

[93] Shaw, J., and Kyriakides, S. Thermomechanical aspects of NiTi. *Journal of the Mechanics and Physics of Solids 43*, 8 (1995), 1243–1281.

[94] Shaw, J. A., and Kyriakides, S. Thermomechanical aspects of niti. *Journal of the Mechanics and Physics of Solids 43*, 8 (1995), 1243–1281.

[95] Stebner, A., and Brinson, L. Explicit finite element implementation of an improved three dimensional constitutive model for shape memory alloys. *Computer Methods in Applied Mechanics and Engineering 257* (2013), 17–35.

[96] Stebner, A., Vogel, S., Noebe, R., Sisneros, T., Clausen, B., Brown, D., Garg, A., and Brinson, L. Micromechanical quantification of elastic, twinning, and slip strain partitioning exhibited by polycrystalline, monoclinic nickel–titanium during large uniaxial deformations measured via in-situ neutron diffraction. *Journal of the Mechanics and Physics of Solids 61*, 11 (2013), 2302–2330.

[97] Sun, L., Huang, W., and Cheah, J. The temperature memory effect and the influence of thermo-mechanical cycling in shape memory alloys. *Smart Materials and Structures 19*, 5 (2010), 055005.

[98] Tadmor, E. B., Miller, R. E., and Elliott, R. S. *Continuum mechanics and thermodynamics: from fundamental concepts to governing equations*. Cambridge University Press, 2012.

[99] Takenaka, K. Negative thermal expansion materials: technological key for control of thermal expansion. *Science and Technology of Advanced Materials 13*, 1 (2012), 11.

[100] Takenaka, K. Progress of research in negative thermal expansion materials: Paradigm shift in the control of thermal expansion. *Frontiers in Chemistry 6* (2018), 267.

[101] Thamburaja, P. A finite-deformation-based phenomenological theory for shape-memory alloys. *International Journal of Plasticity 26*, 8 (2010), 1195–1219.

[102] Šittner, P., Takakura, M., and Tokuda, M. The stabilization of transformation pathway in stress induced martensite. *Scripta Mettallurgica et Materilia 32* (1995), 2073–2079.

[103] Waitz, T., Antretter, T., Fischer, F. D., and Karnthaler, H.-P. Size effects on martensitic phase transformations in nanocrystalline niti shape memory alloys. *Materials Science and Technology 24*, 8 (2008), 934–940.

[104] Wang, B., Kang, G., Wu, W., Zhou, K., Kan, Q., and Yu, C. Molecular dynamics simulations on nanocrystalline super-elastic NiTi shape memory alloy by addressing transformation ratchetting and its atomic mechanism. *International Journal of Plasticity 125* (2020), 374–394.

[105] Wang, J., Moumni, Z., and Zhang, W. A thermomechanically coupled finite-strain constitutive model for cyclic pseudoelasticity of polycrystalline

shape memory alloys. *International Journal of Plasticity 97* (2017), 194–221.

[106] Wang, J., Moumni, Z., Zhang, W., and Zaki, W. A thermomechanically coupled finite deformation constitutive model for shape memory alloys based on hencky strain. *International Journal of Engineering Science 117* (2017), 51–77.

[107] Wang, L., Feng, P., Wu, Y., and Liu, Z. A tensile–compressive asymmetry model for shape memory alloys with a redefined martensite internal variable. *Smart Materials and Structures 28*, 10 (2019), 105050.

[108] Wang, L., Feng, P., Xing, X., Wu, Y., and Liu, Z. A one-dimensional constitutive model for NiTi shape memory alloys considering inelastic strains caused by the R-phase transformation. *Journal of Alloys and Compounds 868* (2021), 159192.

[109] Wasilewski, R. The effects of applied stress on the martensitic transformation in tini. *Metallurgical and Materials Transactions B 2*, 11 (1971), 2973–2981.

[110] Whittaker, E. T. *A treatise on the analytical dynamics of particles and rigid bodies*. CUP Archive, 1937.

[111] Xiao, H., Bruhns, O., and Meyers, A. Hypo-elasticity model based upon the logarithmic stress rate. *Journal of Elasticity 47*, 1 (1997), 51–68.

[112] Xiao, H., Bruhns, O., and Meyers, A. Logarithmic strain, logarithmic spin and logarithmic rate. *Acta Mechanica 124*, 1-4 (1997), 89–105.

[113] Xiao, H., Bruhns, O., and Meyers, A. Explicit dual stress-strain and strain-stress relations of incompressible isotropic hyperelastic solids via deviatoric hencky strain and cauchy stress. *Acta Mechanica 168*, 1-2 (2004), 21–33.

[114] Xiao, H., Bruhns, O., and Meyers, A. Elastoplasticity beyond small deformations. *Acta mechanica 182*, 1 (2006), 31–111.

[115] Xiao, H., Bruhns, O. T., and Meyers, A. Logarithmic strain, logarithmic spin and logarithmic rate. *Acta Mechanica 124* (1996), 89–105.

[116] Xiao, Y., Zeng, P., and Lei, L. Micromechanical modeling on thermomechanical coupling of cyclically deformed superelastic NiTi shape memory alloy. *International Journal of Plasticity 107* (2018), 164–188.

[117] Xu, C., Mudunuru, M. K., and Nakshatrala, K. Material degradation due to moisture and temperature. part 1: Mathematical model, analysis, and analytical solutions. *Continuum Mechanics and Thermodynamics 28*, 6 (2016), 1847–1885.

[118] Xu, L., Baxevanis, T., and Lagoudas, D. A three-dimensional constitutive model for polycrystalline shape memory alloys under large strains combined with large rotations. In *ASME 2018 Conference on Smart Materials, Adaptive Structures and Intelligent Systems* (2018), American Society of Mechanical Engineers Digital Collection.

[119] Xu, L., Baxevanis, T., and Lagoudas, D. C. A three-dimensional constitutive model for the martensitic transformation in polycrystalline shape memory alloys under large deformation. *Smart Materials and Structures 28*, 7 (2019), 074004.

[120] Yan, Y., Yin, H., Sun, Q., and Huo, Y. Rate dependence of temperature fields and energy dissipations in non-static pseudoelasticity. *Continuum Mechanics and Thermodynamics 24*, 4–6 (2012), 675–695.

[121] Yin, H., He, Y., and Sun, Q. Effect of deformation frequency on temperature and stress oscillations in cyclic phase transition of NiTi shape memory alloy. *Journal of the Mechanics and Physics of Solids 67* (2014), 100–128.

[122] Yin, H., Yan, Y., Huo, Y., and Sun, Q. Rate dependent damping of single crystal CuAlNi shape memory alloy. *Materials Letters 109* (2013), 287–290.

[123] Yu, C., Kang, G., and Kan, Q. A micromechanical constitutive model for grain size dependent thermo-mechanically coupled inelastic deformation of super-elastic NiTi shape memory alloy. *International Journal of Plasticity 105* (2018), 99–127.

[124] Yu, C., Kang, G., Kan, Q., and Zhu, Y. Rate-dependent cyclic deformation of super-elastic NiTi shape memory alloy: thermo-mechanical coupled and physical mechanism-based constitutive model. *International Journal of Plasticity 72* (2015), 60–90.

[125] Yu, C., Kang, G., Song, D., and Kan, Q. Effect of martensite reorientation and reorientation-induced plasticity on multiaxial transformation ratchetting of super-elastic NiTi shape memory alloy: New consideration in constitutive model. *International Journal of Plasticity 67* (2015), 69–101.

[126] Yu, C., Kang, G., Sun, Q., and Fang, D. Modeling the martensite reorientation and resulting zero/negative thermal expansion of shape memory alloys. *Journal of the Mechanics and Physics of Solids 127* (2019), 295–331.

[127] Zaki, W. An efficient implementation for a model of martensite reorientation in martensitic shape memory alloys under multiaxial nonproportional loading. *International Journal of Plasticity 37* (2012), 72–94.

[128] Zaki, W., and Moumni, Z. A three-dimensional model of the thermomechanical behavior of shape memory alloys. *Journal of the Mechanics and Physics of Solids 55*, 11 (2007), 2455–2490.

[129] Zaki, W., Moumni, Z., and Morin, C. Modeling tensile-compressive asymmetry for superelastic shape memory alloys. *Mechanics of Advanced Materials and Structures 18*, 7 (2011), 559–564.

[130] Zhang, Y., Jiang, S., and Wang, M. Atomistic investigation on superelasticity of niti shape memory alloy with complex microstructures based on molecular dynamics simulation. *International Journal of Plasticity 125* (2020), 27–51.

[131] Zhu, S., and Zhang, Y. A thermomechanical constitutive model for superelastic sma wire with strain-rate dependence. *Smart Materials and Structures 16*, 5 (2007), 1696.

[132] Zhu, X., Chu, L., and Dui, G. Constitutive Modeling of Porous Shape Memory Alloys Using Gurson–Tvergaard–Needleman Model Under Isothermal Conditions. *International Journal of Applied Mechanics 12*, 04 (2020), 2050038.

A APPENDIX

A.1 Tension-Compression Asymmetry–Convexity of the Associated Yield Surface

NiTi SMAs have been reported to exhibit asymmetric behavior under tension and compression during phase transformation, which is discussed in Section 1.4.1. The intensity of the asymmetry depends on the heat treatment and, consequently, the size of the formed precipitates [32]. The material usually shows higher transformation stress, smaller recoverable strain and steeper transformation strain-stress slope when it is subjected to compressive load. Conversely, lower critical stress, and larger recoverable strain are observed when subjected to tension. The present work in this section is devoted to the analysis of yield conditions and dissipation potentials of tension-compression asymmetry of SMAs. To capture the tension-compression, a class of yield conditions based on the second and third deviatoric stress invariants is expressed by [87]. The Lode invariants r and y are induced to present the asymmetry,

$$\begin{aligned} \tilde{J}_2 &= \frac{1}{2}\mathrm{Tr}(\boldsymbol{\tau}'^2), & \tilde{J}_3 &= \mathrm{Det}(\boldsymbol{\tau}'), \\ r(\boldsymbol{\tau}') &= \sqrt{2\tilde{J}_2}, & y(\boldsymbol{\tau}') &= \frac{3\sqrt{3}\tilde{J}_3}{2(\tilde{J}_2)^{\frac{3}{2}}}, \end{aligned} \tag{A.1}$$

where $\boldsymbol{\tau}'$ is denoted to the deviatoric part of Kirchhoff stress $\boldsymbol{\tau}$.[12] The Lode invariant $r(\boldsymbol{\tau}')$ represents the stress radius, and $y(\boldsymbol{\tau}')$ is the homogeneous function of degree zero of the stress deviator, which is bounded by $[-1, 1]$. That means the value of $y(\boldsymbol{\tau}')$ can indicates the stress state of material. If $y(\boldsymbol{\tau}')$ takes value $y(\boldsymbol{\tau}') = 0$, the material is at simple shear. The material is under tension if

[12] We use $\boldsymbol{\pi}$, the thermodynamic force conjugated to $\boldsymbol{h}^{in}$ (see Eqn. (3.27)) to define the yield surfaces in previous chapters.

$y(\boldsymbol{\tau}') = 1$ and compression if $y(\boldsymbol{\tau}') = -1$. The asymmetric yield surface can be specified by a two-parameter power shape function as,

$$R(y) = (1 + b\, y(\boldsymbol{\tau}'))^{\frac{1}{n}} = \left(1 + \gamma \frac{\mathrm{Det}(\boldsymbol{\tau}')}{\overline{\tau}^{\frac{3}{2}}}\right)^{\frac{1}{n}}, \;\; R(0) = 1, \;\; \gamma = \frac{27}{2} b \tag{A.2}$$

According previous work [87], the convexity condition of the shape function is defined as Eqn. (A.3),

$$(1 - y^2) R^{''}(y) - y R^{''}(y) + \frac{R(y)}{9} \geqslant 0 \tag{A.3}$$

Consequently, we are able to find the convexity condition for the two asymmetric parameters γ and $\dfrac{1}{n}$ as Eqn. (A.4):

$$\begin{cases} \frac{1}{n} \leq 0 \\ \gamma \leq \frac{27}{2} \frac{n}{n-9} \end{cases}, \text{ or } \begin{cases} 0 \leq \frac{1}{n} \leq \frac{11}{3} \\ \gamma \leq \frac{27}{2} \sqrt{\frac{12n^3 - 39n^2}{12(n-1)(n^2-9)}} \end{cases}, \text{ or } \begin{cases} \frac{1}{n} \geq \frac{11}{3} \\ \gamma \leq \frac{27}{2} \frac{n}{9-n} \end{cases}. \tag{A.4}$$

The theoretical convexity region is shown in Figure A.1.

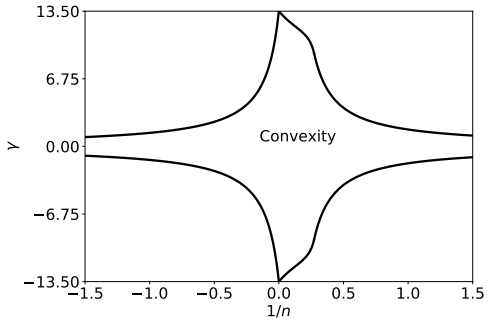

Figure A.1: Convex region of asymmetric yield surface [87]

Then a $J_2 - J_3$ yield surface contributing to tension-compression asymmetry

can be defined as Eqn. (A.5),

$$\Phi(\boldsymbol{\tau}) = R(\boldsymbol{\tau}')\overline{\tau} = \left(1 + \gamma \frac{\mathrm{Det}(\boldsymbol{\tau}')}{\overline{\tau}^{\frac{3}{2}}}\right)^{\frac{1}{n}} \overline{\tau}. \tag{A.5}$$

To visualize how the asymmetry shape function contributing to the yield surface, a theoretical limit transformation curve in plane stress in displayed in Figure A.2, where τ_c is the critical stress. In Figure A.2(a), the dotted line shows the yield surface based on classical J_2 theory, and the solid line is the yield condition considering tension-compression asymmetry. Figure A.2(b) shows the yield surface if the asymmetric parameters fail to satisfy the convexity condition.

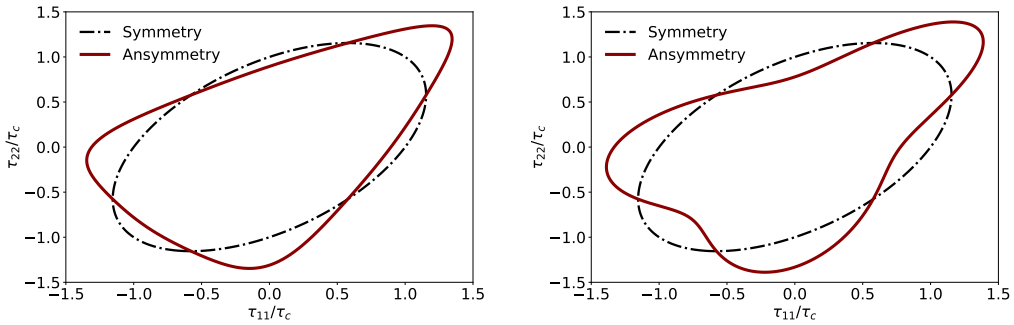

(a) In convexity region (b) Out of convexity region

Figure A.2: Theoretical limit transformation curve in plane stress state for SMA

A.2 TE Tensors of the Austenite and Martensite Lattices

As reported by [73], the austenite phase in NiTiPd is a cubic B2 structure with a lattice length of $a_0 = 0.3091$nm and the martensite phase is an orthorhombic B19 structure and its lattice constants are $a = 0.2784$nm, $b = 0.4450$nm and $c = 0.4697$nm. The TE tensor of the austenite lattice is isotropic

$$\boldsymbol{\kappa}^A = \kappa_{ij}^A \mathbf{e}_i^A \otimes \mathbf{e}_i^A, \tag{A.6}$$

where $\boldsymbol{e}_1^A := [100]_A$, $\boldsymbol{e}_2^A := [010]_A$, and $\boldsymbol{e}_3^A := [001]_A$ are the orthonormal basis vectors of the local coordinate system of austenite (Figure A.3a) and

$$\left[\kappa_{ij}^A\right] = \begin{bmatrix} 14.4 & 0 & 0 \\ 0 & 14.4 & 0 \\ 0 & 0 & 14.4 \end{bmatrix} \text{ ppm K}^{-1}. \tag{A.7}$$

The TE tensor of the martensite lattice is anisotropic,

$$\boldsymbol{\kappa}^M = \kappa_{ij}^M \mathbf{e}_i^M \otimes \mathbf{e}_i^M, \tag{A.8}$$

where $\mathbf{e}_1^M := [100]_M$, $\mathbf{e}_2^M := [010]_M$, and $\mathbf{e}_3^M := [001]_M$ are the orthonormal basis vectors of the local coordinate system of martensite residing on the *a*, *b*, and *c*-axis, respectively (Figure A.3(b)), and

$$\left[\kappa_{ij}^M\right] = \begin{bmatrix} 51.33 & 0 & 0 \\ 0 & -3.17 & 0 \\ 0 & 0 & -34.51 \end{bmatrix} \text{ ppm K}^{-1}. \tag{A.9}$$

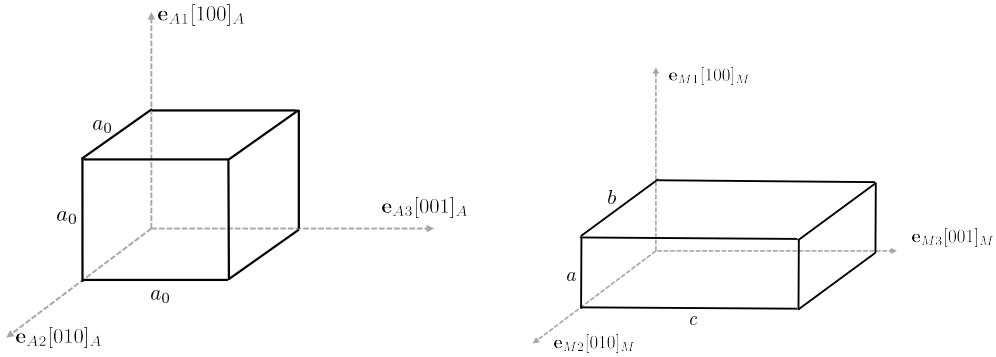

(a) Austenite (b) Martensite

Figure A.3: Austenite and martensite unit cells in their respective local coordinate systems